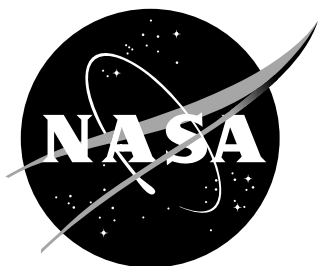NASA/TM–2012–217761

Investigation of "6X" Scramjet Inlet Configurations

Stephen J. Alter
Langley Research Center, Hampton, Virginia

September 2012

NASA STI Program . . . in Profile

Since its founding, NASA has been dedicated to the advancement of aeronautics and space science. The NASA scientific and technical information (STI) program plays a key part in helping NASA maintain this important role.

The NASA STI program operates under the auspices of the Agency Chief Information Officer. It collects, organizes, provides for archiving, and disseminates NASA's STI. The NASA STI program provides access to the NASA Aeronautics and Space Database and its public interface, the NASA Technical Report Server, thus providing one of the largest collections of aeronautical and space science STI in the world. Results are published in both non-NASA channels and by NASA in the NASA STI Report Series, which includes the following report types:

- TECHNICAL PUBLICATION. Reports of completed research or a major significant phase of research that present the results of NASA Programs and include extensive data or theoretical analysis. Includes compilations of significant scientific and technical data and information deemed to be of continuing reference value. NASA counterpart of peer-reviewed formal professional papers, but having less stringent limitations on manuscript length and extent of graphic presentations.

- TECHNICAL MEMORANDUM. Scientific and technical findings that are preliminary or of specialized interest, e.g., quick release reports, working papers, and bibliographies that contain minimal annotation. Does not contain extensive analysis.

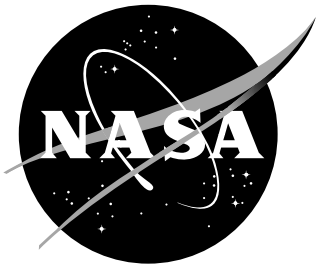- CONTRACTOR REPORT. Scientific and technical findings by NASA-sponsored contractors and grantees.

- CONFERENCE PUBLICATION. Collected papers from scientific and technical conferences, symposia, seminars, or other meetings sponsored or co-sponsored by NASA.

- SPECIAL PUBLICATION. Scientific, technical, or historical information from NASA programs, projects, and missions, often concerned with subjects having substantial public interest.

- TECHNICAL TRANSLATION. English-language translations of foreign scientific and technical material pertinent to NASA's mission.

Specialized services also include organizing and publishing research results, distributing specialized research announcements and feeds, providing information desk and personal search support, and enabling data exchange services.

For more information about the NASA STI program, see the following:

- Access the NASA STI program home page at *http://www.sti.nasa.gov*

- E-mail your question to help@sti.nasa.gov

- Fax your question to the NASA STI Information Desk at 443-757-5803

- Phone the NASA STI Information Desk at 443-757-5802

- Write to:
  STI Information Desk
  NASA Center for AeroSpace Information
  7115 Standard Drive
  Hanover, MD 21076-1320

Investigation of "6X" Scramjet Inlet Configurations

Stephen J. Alter
Langley Research Center, Hampton, Virginia

September 2012

Acknowledgments

Available from:

NASA Center for AeroSpace Information
7115 Standard Drive
Hanover, MD 21076-1320
443-757-5802

Abstract

This work presents a performance analysis of scramjet inlets that are scaled to six times the capture area of the X-43 HyperX vehicle. These inlets are the largest size that could be tested in the 8-ft high temperature tunnel (8-ft HTT) at NASA Langley Research Center, and were analyzed to determine what was possible to test within the facility for the next generation of hypersonic flight vehicles. The inlets could be used as the flight scale geometry of a viable candidate for both military and civilian applications. To determine performance characteristics, existing 8-ft. HTT nozzle exit conditions were a basis for the hypersonic inlets designed to operate at nominal Mach 4 and Mach 5 conditions. A total of 16 detailed flow field solutions were computed for alternate scramjet inlet designs at Mach 4 and 5, and off-design conditions at Mach 3.The total pressure recovery for viable inlets was about 70 percent, while maintaining self-start characteristics and providing operable inflow to scramjet combustors. Based on this study, the strength of a vortex created along the cowl edge causing adverse boundary layer growth in the inlet, was highlighted as an issue for further investigation.

Contents

List of Figures

4

List of Tables

1 Introduction

To date, hypersonic flight has been limited to rocket propelled vehicles [1] and small subscale hypersonic air-breathing engine test vehicles [2]. In order to enable the use of air-breathing engines for hypersonic flight, previous test vehicles, such as the X-43 and X-52, need to be scaled from ten to as much as one hundred times their current size. Such scaling of these vehicles is necessary to enable the inclusion of usable types of payloads for both military and access to space missions [3].

Previous flight programs that tested vehicle models in wind-tunnels at less than full-scale Reynolds number and engine components at less than full scale at actual flight conditions, have experienced issues because of scaling [4–6]. According to the references considered, some of the scaling issues occurred because of an inability to accurately model flight conditions or chemically reacting gas effects.

NASA Langley's Hypersonic Air-breathing Propulsion Branch (HAPB) is developing wind tunnel test capabilities that could explore the effect of scaling up from X-43 size vehicles. Scramjets are comprised of four basic segments; an inlet, an isolator that is used to "isolate" the supersonic inlet flow from the back pressure rise in the combustor, a combustor, and a nozzle aft of the combustor. HAPB sought to explore the design space limit of hypersonic inlets that could be tested in the 8-Foot High Temperature Tunnel (8-ft HTT), by investigating which geometric constraints [7, 8] could produce a viable entrance flow into the scramjet combustor. The purpose of this study is to develop the "6X" scramjet inlet designs that could be tested in the 8-ft HTT. In this case "6X" refers to the capture area that is six times the X-43. Some of the geometric constraints considered for this study include capture area, capture shape, aspect ratio of the capture shape, compression ratio, throat cross-section, contraction ratio, total pressure recovery, shock impingement location on the cowl, length, width, and transition shape from inlet entrance to isolator exit.

There are a variety of techniques for designing and analyzing inlets for scramjets [9–11]. A recently developed tool, the Three-Dimensional Hypersonic Inlet System (3DHItS) was used for this study. The 3DHItS designs rectangular to elliptic shaped transition [12,13] (REST) geometries for an inlet. The parameters used to design these inlets included free stream Mach number, aspect ratio, inlet flow angle, throat diameter, throat to isolator angle, cowl lip radius, leading edge radius, as well as height, width, and length of the two dimensional projection of the front of the inlet, as shown in figure 1.

For this study, the circular throat of the scramjet inlet was held fixed at 9 in. diameter and the geometry of the inlet entrance was a square cross-section. In order for a 6X inlet to fit in the 8-ft HTT, the length of the inlets had to be constrained. The inlets were designed for a specific free stream Mach number, sized for a mass flow rate ($\dot{m}$) consistent with either high or low dynamic pressure tunnel conditions and then computed at on and off-design Mach numbers for determining performance characteristics. Mach 4 and Mach 5 hypersonic inlets were designed and analyzed in detail for both on and off design conditions, using four different contraction ratios, resulting in 16 flow field computations. GridPro was used to generate the volume grids, which were post processed with GridGen prior to using the VULCAN [14,15] flow solver for fluid dynamic simulations. Within the VULCAN software, two solver methods were used; the direct approximate factorization (DAF) and the incomplete lower-upper (ILU) solvers. The ILU provided solutions at a more converged state characterized by a typical order of magnitude lower in in the residuals of the Navier-Stokes equations over the DAF converged solutions. Extensive discussion of typical trends in the data were noted in the results section of the report. For example, directly proportional relationships between contraction ratio and shock strength, shock strength and surface pressure were observed
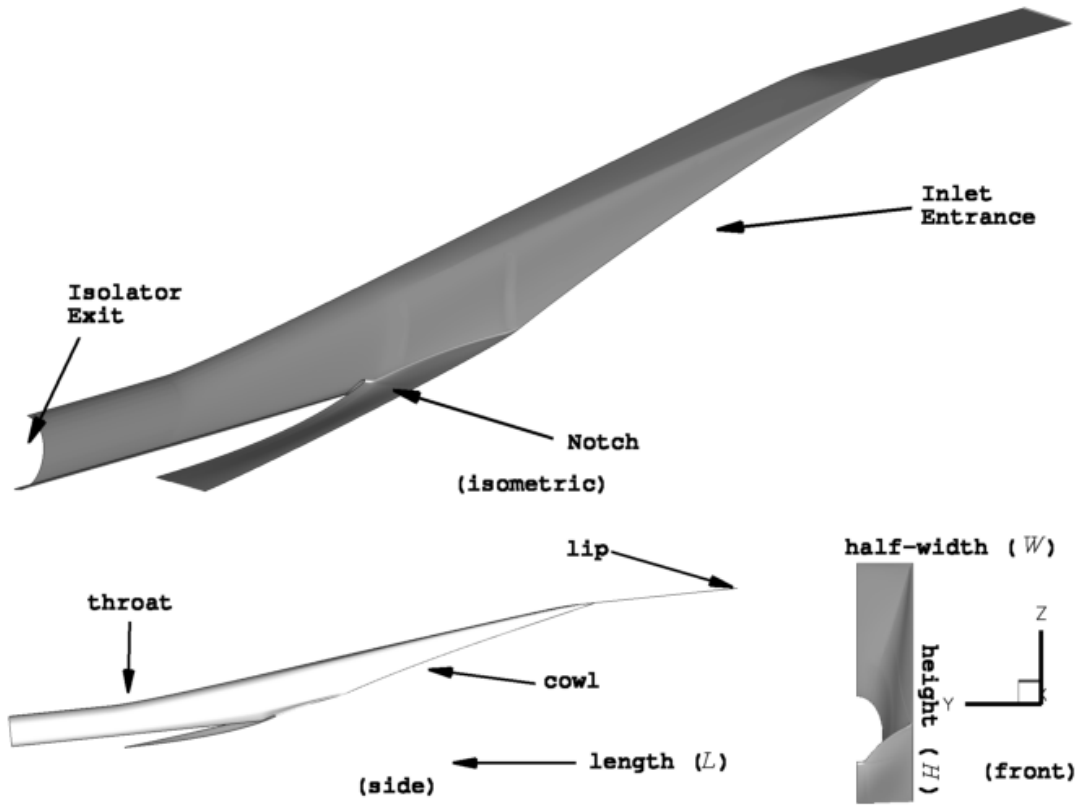
Figure 1. Side, front, and isometric view of a typical REST inlet with the design parameters noted.

as well as an inverse relationship between solution time and shock strength. There are seven more sections to this report detailing the design space and geometry generation, grid generation, flow field solutions, results, inlet performance, geometric enhancements and a summary.

Nomenclature

A	wetted surface area of the inlet, in^2
A_δ/A_c	boundary layer area ratio (proportion of boundary layer area, A_δ, at a given cross-section, A_c)
BL	boundary layer
CR	contraction ratio
H	height of inlet, inches
L	length of side of inlet (2D), inches
M	Mach number
$\dot{m}$	mass flow rate, lbm/s
μ_{edge}	viscosity at boundary layer edge
p	static pressure, psi
Q	heat transfer rate, BTU/ft^2 sec
q	dynamic pressure, psi
Re_θ	Reynolds number based momentum thickness
ρ	density, lbm/in^3
T	static temperature, R
U, u	streamwise velocity, ft/sec
v	spanwise velocity, ft/sec
V_{edge}	Boundary layer edge velocity, ft/sec
W	capture width of inlet, inches
w	pitch plane velocity, ft/sec
x	streamwise coordinate along axis of inlet, inches
y	spanwise coordinate from pitch plane of inlet, inches
y^+	wall distance for law of the wall
z	vertical coordinate from center of inlet axis, upward, inches
α	angle of attack, degrees
δ	boundary layer thickness, inches
δ^*	displacement thickness, inches
η	flow distortion metric
θ	momentum thickness, inches
τ	shear stress, psi
Subscripts	
$0,\infty$	free stream, flight conditions
1	inlet entrance conditions
e	isolator exit location
ref	reference condition

2 Design Space and Geometry Generation

The design procedure for a REST inlet began with the computation of an inviscid axisymmetric compression flow field for an inflow Mach number, free-stream conditions, and a specific contraction ratio. A one-dimensional equivalent pressure recovery is obtained for each specified contraction

ratio. The rate of change of cross-sectional area along the flow path in the compression flow field was controlled in such a way as to make it isentropic, until the flow was turned by the cowl shock at the notch. This had the desirable effect of mitigating pressure losses due to internal shock waves. Then a region inside the compression field was used to draw streamlines both downstream from the entrance and upstream from the exit. This gave two inlets; one with the appropriate capture shape and another with the appropriate throat shape. Inviscid inlets were subsequently lofted and enlarged to account for boundary layer growth because the resulting displacement could have caused further compression. Pressure rise from the compression led to lower Mach numbers near the end of the inlet. It was possible for the Mach number to be too low, resulting in an unstart [16, 17] of the inlet. The two inlets were lofted to generate a discretized cloud of points. Then, best-fit curves were found for key geometric features such as turning angle at the cowl. These curves were used in the construction of continuous computer aided design (CAD) geometry for an inlet using the Adaptive Modeling Language software from Technosoft [18]. Thus, there were both geometric and flow based parameters that could be used to control the construction of the inlet [19, 20].

The initial controlling parameters that were considered included the entrance Mach number, the geometric contraction ratio (the ratio of the projected two-dimensional area of the inlet entrance to the area of the inlet throat), and the aspect ratio of the capture shape (the width divided by the height). Figure 2 shows how the latter two geometric sets of parameters were obtained.
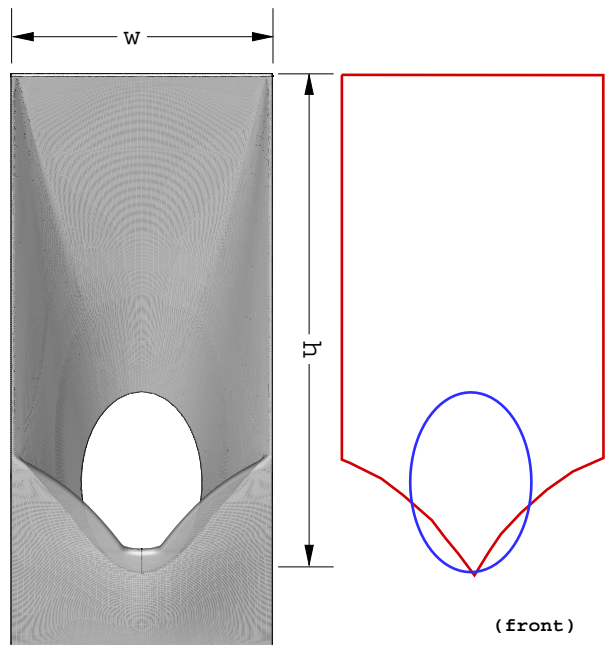
Figure 2. Origination of geometric parameters used to design the REST inlets in this study.

As shown in figure 2, the red and blue outlines represent the two-dimensional projections of the inlet capture area and the throat, respectively. Within the lines that define the capture area of the inlet, the lower curved lines come together at a point, which is not consistent with the actual REST inlet on the left of figure 2. The reason for this difference is that a sharp edge at the inlet notch is not desirable from a mechanical design point of view. To more accurately model the geometry, this sharp section was rounded with a 1.0 inch radius. Also note that the blue line is a super-ellipse.

The throat aspect ratio and super-ellipse power are specified. The cross-sectional area ratio of these two curves was then used to define the contraction ratio, dividing the capture area from the throat area.

After considerable review of the design parameters available for construction of the inlet with the 3DHItS tools, the 3DHItS team modified the parameters used to design the inlets for this study. The inlets being considered for this study were evaluated to determine a single inlet that could be used in the 8-ft HTT. The purpose of this single inlet was to operate over a range of simulated flight Mach numbers. The inlet was also for testing subsequent engines that the USAF contractors had been considering for construction. The engines had a capture area that was six times the typical demonstration size scramjets already proven for flight. The 8-ft HTT facility at the time of this study had what is called a direct-connect fixture that mimics the end of an isolator of an inlet. NASA Langley was attempting to develop an alternative to the direct-connect fixture by designing an inlet that could provide sufficient compression, and isolator entrance conditions suitable for a scramjet engine to operate.

The inlet was designed without viscous corrections. The design procedure used both upstream and downstream streamline tracing from the circular exit of the inlet to a square entrance that is a subset of the REST class of inlets, as shown in figure 3.

(a) Cross-sections.   (b) Initial surface.
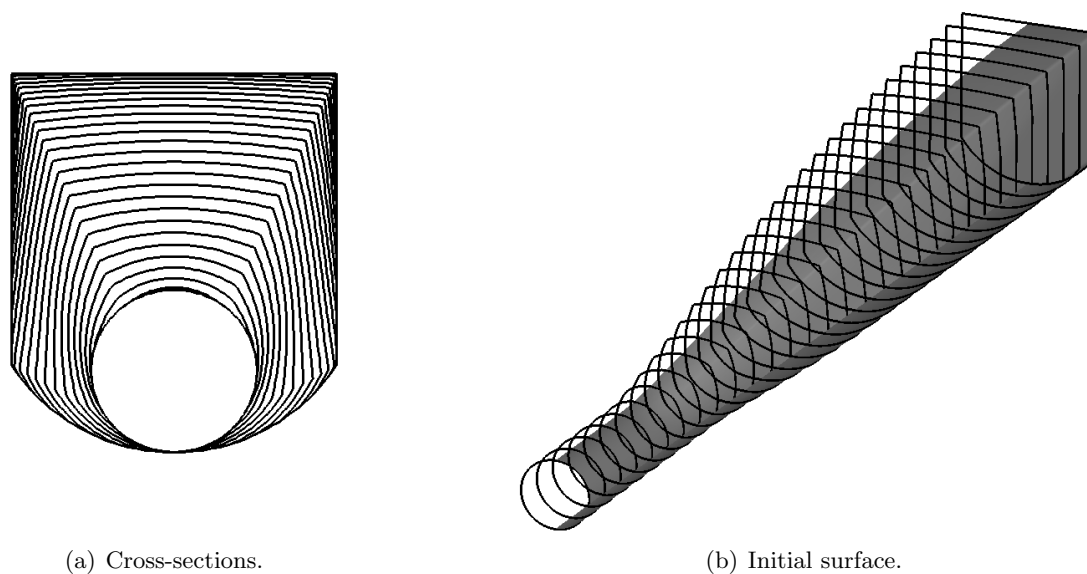
Figure 3. Circular to square shape transition from axisymmetric compression field for inlet design.

To date, only elliptic cross-section throat engines were designed using REST [21]. This study focused on changing the throat cross section to a cylinder because the shape offers a more compact packaging for staging the engines adjacent to one another. Thus, of the variety of parameters to choose for the design of these inlets, the design parameters were reduced down to a 9 inch circular throat with four different contraction ratios at two different on-design Mach numbers that are possible in the 8-ft HTT facility.

The highest Mach number considered was 5, with an upper contraction ratio limit that attempted to produce one atmosphere of pressure at the isolator entrance and with the Kantrowitz self-start limit as the lower contraction ratio limit. In order to determine trends, two additional

Table 1. Design variables and configurations for $M_\infty = 5$.

Configuration Designation	Mach Number	Contraction Ratio	Target Exit Pressure (atm)
5A	5	5.42	1.00
5B	5	4.86	0.75
5C	5	3.80	0.50
5D	5	2.92	Kantrowitz Limit

Table 2. Design variables and configurations for $M_\infty = 4$.

Configuration Designation	Mach Number	Contraction Ratio	Target Exit Pressure (atm)
4A	4	5.42	1.00
4B	4	4.87	0.75
4C	4	3.92	0.50
4D	4	2.99	Kantrowitz Limit

contraction ratios between these limits were chosen. The first was one that had half an atmosphere at the throat, and a second that was between that condition and the highest limit. The second Mach number considered for this study was Mach 4, where instead of designing for specific throat pressures, the target was the same contraction ratios as the Mach 5 design, to provide similar flow conditions to the downstream sections of an engine. In tabulated form, the run matrix of geometric cases is shown in tables 1 and 2.

As the inlets were designed with the Shape Transitioning InLEts (STILE) software, which is a tool in the 3DHItS suite, the contraction ratios were determined implicitly. Because of the parameters chosen, an iterative process is used with the STILE code to find the contraction ratio that provided the matching throat compression ratio for the Mach 5 conditions. The Mach 4 cases were then designed to have comparable contraction ratios to the Mach 5 cases. With these eight designs, an off-design Mach number of 3 was used to test low Mach number operability and flow quality. To identify the cases computed, either a "D" or "OD" is appended to the configuration designation in tables 1 and 2, identifying either a design or off-design case, respectively. Thus, case 5A-OD is the Mach=3 conditions for the Mach=5 design case.

Since the throat is circular, the front of the inlet is being dictated by lofting streamlines from the axisymmetric compression field and developing a rectangular-like capture shape. Since the upstream geometry of this tracing is nearly a circle, the rectangular-line capture shape was a compromise whereby the projected area of the upstream inlet was preserved. A rectangular-like capture shape was sought because it was more easily integrated into a linear array of inlets for the construction of an efficient propulsion system [12,22,23]. Such a shape also offered easy integration onto planar vehicle configurations as shown in figure 4.

Figure 4. Adjacent array packaging of REST inlets on a planar underbody.

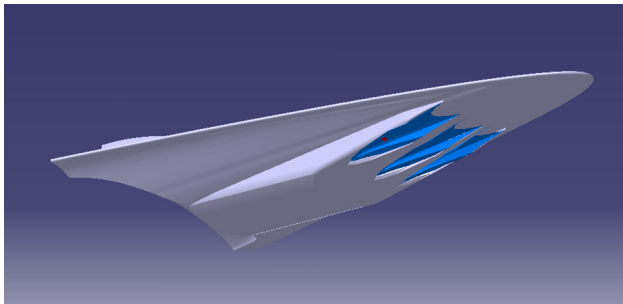# 3   Grid Generation

Within the 3DHItS suite, several software codes were used to construct the initial design, generate geometric surfaces to perform grid generation, and post process the grid to prepare for computational fluid dynamic simulation. The process, shown in figure 5 began by taking the key geometric information from the STILE design software and creating an input file for the Adaptive Modeling Language [18] (AML^{TM}) for constructing and defining curves and surfaces as shown in figure 6.

The AML^{TM} software outputs the generated surface in a stereo-lithography (STL) geometric format, which is simply a set of triangles that approximate the surface to within a prescribed tolerance of angle and curve precision. The STL file was subsequently loaded into the $GridPro^{TM}$ [24] grid generation software with an established topology for the designed class of inlet. While $GridPro^{TM}$ enables the user the ability to generate topology, the strength of this software is the ability to adapt an existing topology to a similar class of geometry, thereby significantly reducing the time required to generate a structured grid. When imported into $GridPro^{TM}$, the topology shown in figure 7 was manipulated so that the corners of the topological constructs were close to, but not necessarily attached to, the defining STL surface of the geometry.

With the topology manipulated, the grid was generated automatically by $GridPro^{TM}$ by projecting the topology to the surface, and smoothing the grid with an elliptic partial differential equation solver. Block boundaries were generated automatically, and a nearly orthogonal grid was produced in every location possible, given the constraints of the STL surface and the provided topology. The result is a grid shown in figure 8.

The initial grid generated for all inlets was sized for calculations using wall functions boundary conditions, and comprised of 216 blocks. Since the topology did not change for any of the inlets, the computational coordinate orientation and grid point count remained constant. Using grid clustering and merging of blocks into "superblocks" with $GridPro^{TM}$ the final grid was 14 blocks dimensioned for viscous flow field computations. This grid was subsequently clustered near the wall of the inlet to target a y+ value of 25 to 100. Large values of y+ were used because they did not exacerbate convergence issues with the flow solver that was used, as will be explained in the following section. Thus, all grids generated used the same process, and produced topologically identical grids and dimensions. This had the desired effect of not requiring input deck regeneration for the flow solver. The final steps in processing the grid were performed with $GridGen^{TM}$, where the grid was reoriented in computational space so that the I-coordinate aligned with the free-stream flow direction and divided into 17 blocks. Each volume grid contained 7,324,672 cells and was decomposed for parallel processing.
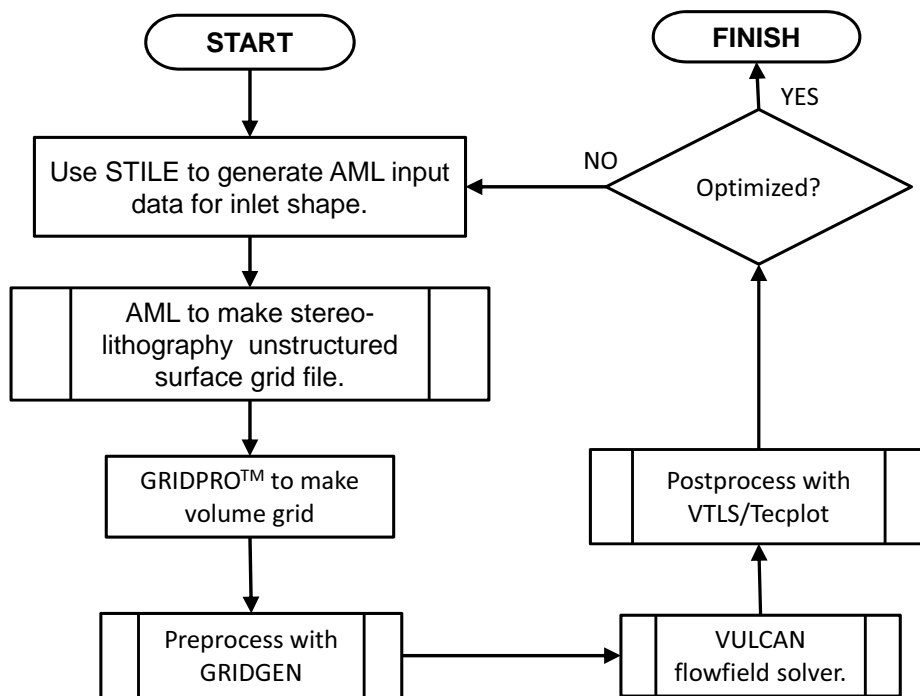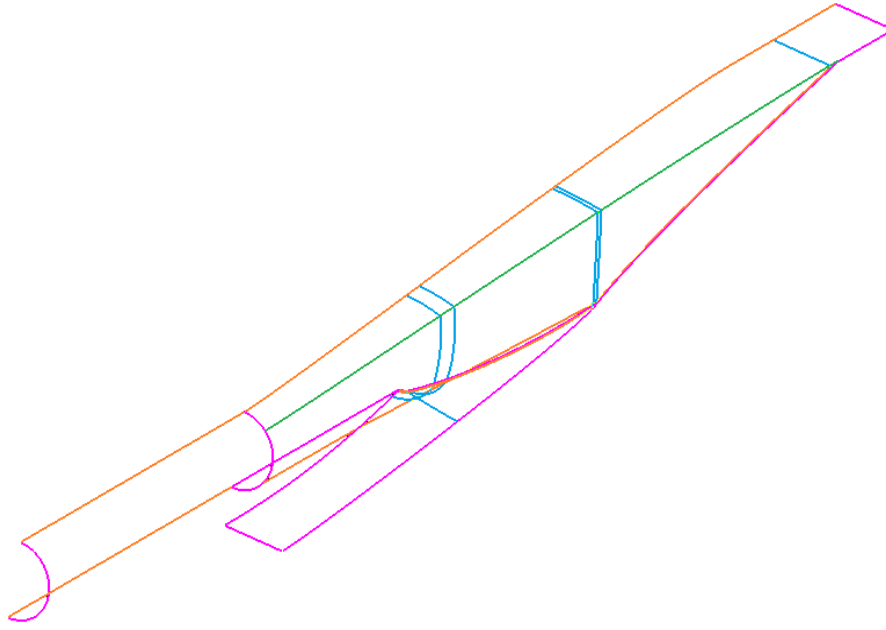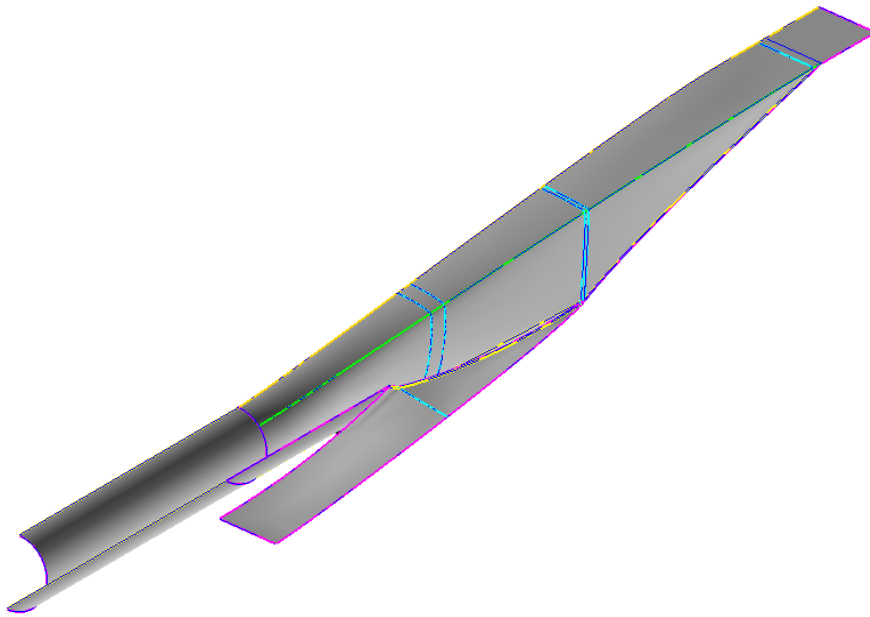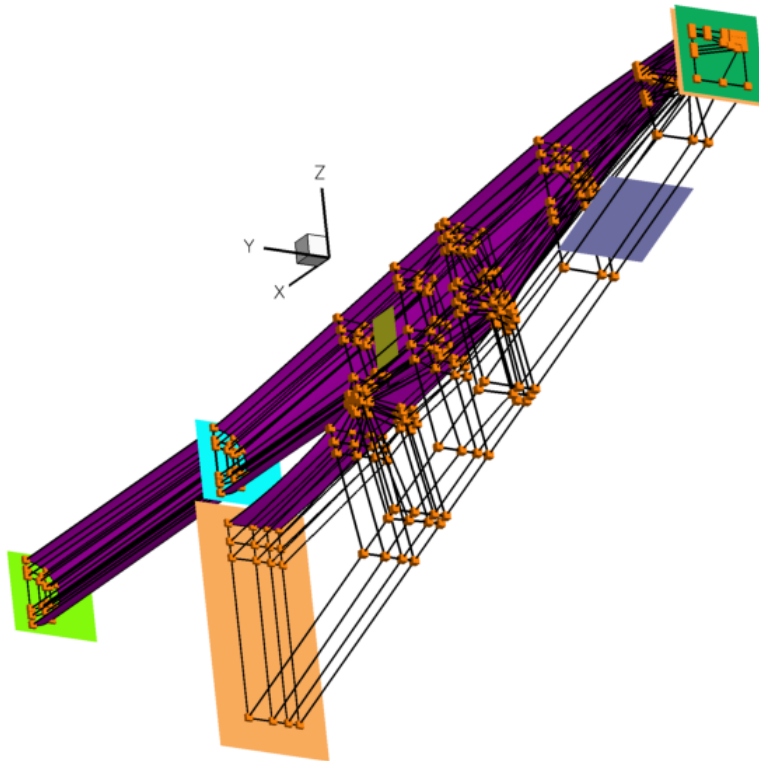
Figure 5. 3DHItS process flow chart.
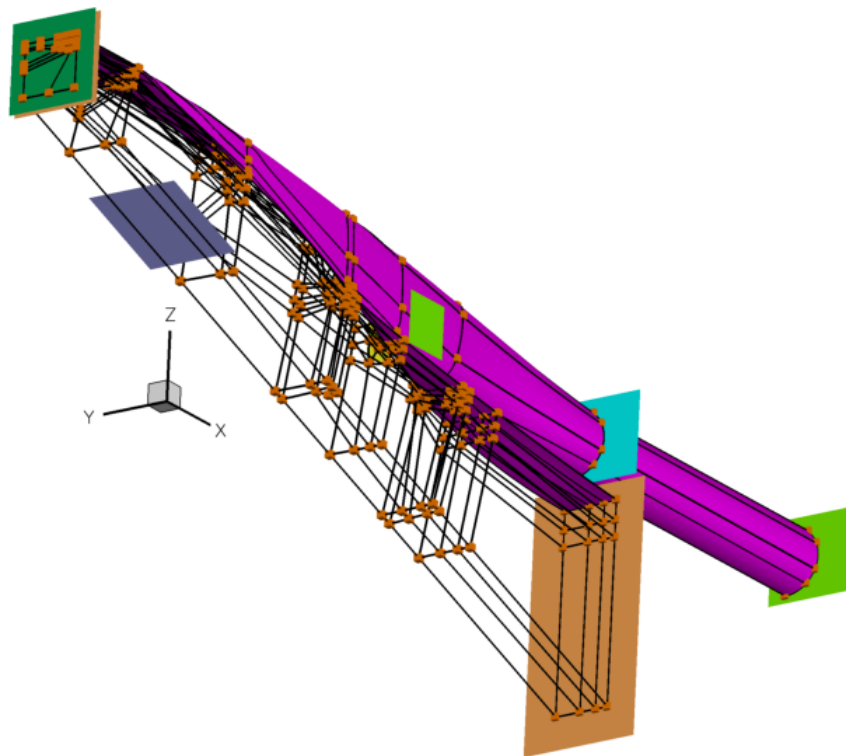
(a) Curve construction.

(b) Surface generation.

Figure 6. Adaptive Modeling Language lofting of curves and surfaces for the REST inlets.
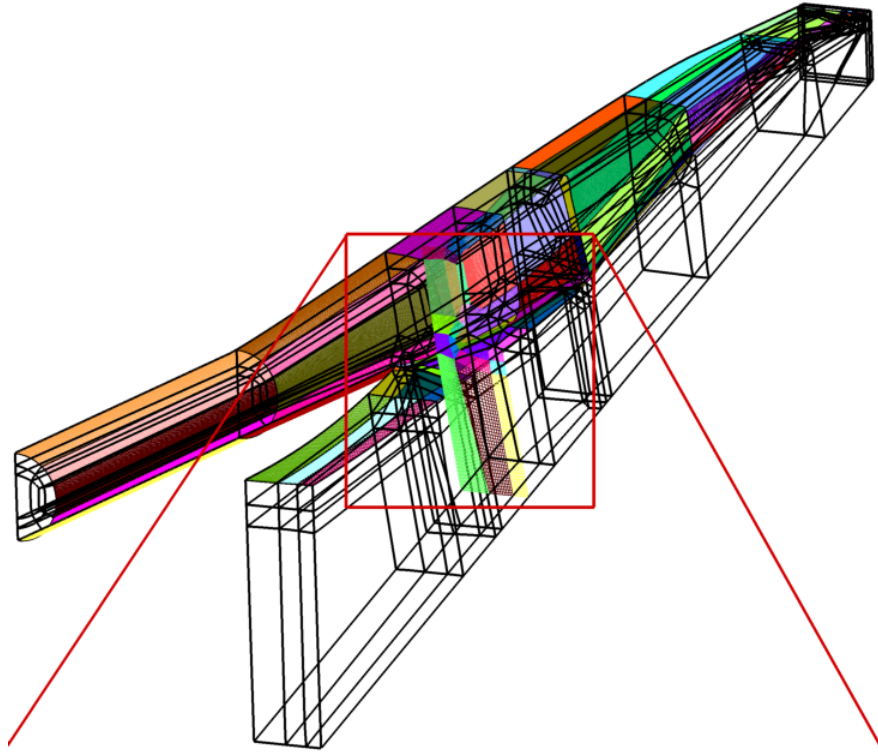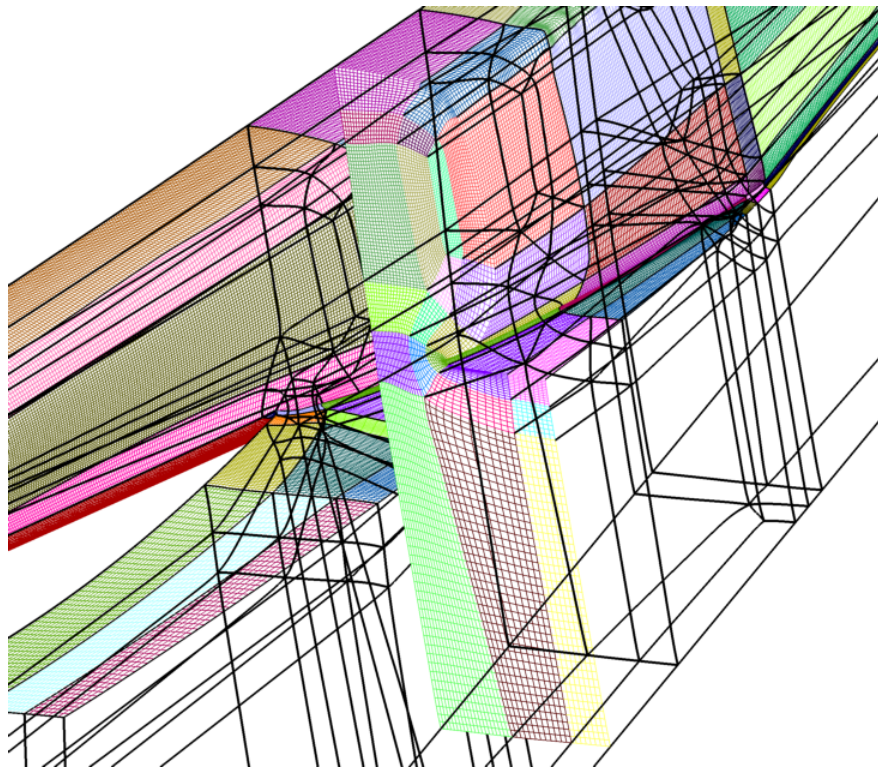
(a) Inside view.

(b) Outside view.

Figure 7. GridPro^{TM} topology views of the inlet grid construction.

(a) Global view.

(b) Focused view.

Figure 8. GridPro^{TM} generated grid for the inlet.

17

4 Flow Field Solutions

With volume grids generated, the VULCAN version 6.1.0 flow solver was the computational fluid dynamics software used for this study. The flow field simulated for each case was modeled with the Navier-Stokes equations, a Wilcox 1998 $k - \omega$ turbulence model, with a thermally perfect species mixture based on the gas model of Gordon and McBride [25]. The species were constructed for the gaseous products of air and methane combustion at equilibrium conditions with oxygen replenishing, an operating gas mixture condition of the 8-ft HTT. For boundary layer modeling, the wall matching boundary functions [26] were used instead of integrating to the wall. This enabled the use of fewer and lower aspect ratio cells than required for integrating to the wall and improves convergence of the flow solver.

The flow conditions provided to the VULCAN flow solver for flow and reference conditions are shown in table 3. The Mach 5 and Mach 3 conditions, indicated by M_1, were for high dynamic pressure (q) while the Mach 4 conditions were for a low dynamic pressure. These conditions were not specific to a flight trajectory. Rather, they were specific to the flow conditions that were possible using available nozzles in the 8-ft HTT facility. Thus, these conditions represent what could be tested should validation data for these inlets become available.

Table 3. Nominal flow field conditions for the REST inlets of this study.

M_∞	M_1	P_1 (psi)	T_1 ^{o}R
4	3	3.66	585.0
5	4	0.49	563.4
6	5	1.01	549.0

Within the VULCAN code, there are a variety of solvers. For this study, the Diagonal Approximate Factorization (DAF) solver was used to start all solutions and was run to convergence. The DAF solver uses hyperbolic partial differential equations in time, which enabled the use of grid sequencing techniques. However, the solver was initialized by starting with a coarsening of the grid by every fourth point in each computational direction until the L2 norm of residuals dropped four orders of magnitude from the initialized free-stream conditions. Then the grid was doubled to a grid of every other point in each computational direction for the same criteria, and finally the original grid resolution was used to finish the computation to a converged state. The DAF scheme uses limited memory resources and runs quickly on desktop workstations, which is why it is more widely used. To improve convergence, the first 7000 iterations were computed with first order accurate derivatives and second order after that point. As will be explained later, the scheme is not the best at obtaining converged solutions. To ensure that a uniformly converged solution was achieved, a more implicit solver, the incomplete lower-upper (ILU) flow solver was used from a restart condition of the converged DAF. This solver was only operated on the original grid density at Courant-Freidrichs-Lewy (CFL) numbers around 100 until the same convergence criteria, to be detailed below, was obtained.

Convergence was determined by monitoring six different metrics: the log of the L2 norm of residuals, the mass flow rate error, the integrated surface heat transfer, and the integrated pitching moment. Each of these measures was determined to be sensitive to the state of the flow field, as given in a previous similar study [27]. Convergence was considered to exist if the log of the L2 norm residuals had dropped at least four orders of magnitude from their highest value, the mass

flow rate error decreased six orders of magnitude from the beginning of the computation, and both the integrated surface heat transfer and moments were constant values to within 0.1 percent change after 100 iterations.

4.1   Convergence Determination

A detailed analysis of case 5B-D was performed where the DAF and ILU were exercised as in all other solutions. Figure 9 shows the six parameters used to determine convergence of the flow field for case 5B. Clearly from these integrated quantities, the DAF solution would be considered converged. The log of the L2 norm residuals has leveled at more than three orders of magnitude drop from their initial values, the mass flow rate error is close to zero, and the integrated quantities of surface heat transfer and the three moments are constant. Even the ILU solution indicates the same level of convergence.

Figure 10 shows the initial differences between the converged solutions of the DAF and ILU schemes for local parameters of surface heat transfer and y+. Convergence verification was dependent on two boundary layer dependent parameters: the percentage differences between the ILU solutions in surface heat transfer and y+. These are local point parameters, and are not integrated values over the entire surface. Rather, they are localized quantities that could show details of the converged state of the flow field solution, and, in particular, with respect to the boundary layer. In this case, the differences are so significant, it would suggest the DAF scheme was not converged and was typical of many of the computations performed for this study. While some of the differences are outside the inlet, the region aft of the notch along the bottom of the inlet centerline has significant differences in the range of 40 percent in surface heat transfer. Similarly, for y+ the values are significantly different in the post notch region.

Therefore, convergence verification was performed by restarting the converged state of the ILU solution and executed another 1000 iterations, nearly the same number of iterations used to obtain the first ILU solution. Figure 11 shows the same differences for this extended computation, indicating the first ILU converged solution was as converged as necessary for an accurate computation. Accuracy for the ILU as compared to the DAF was based on residuals of the L2 and mass flow rate being smaller than the DAF solution. Thus, the ILU solver was considered to produce the best solution for the computations performed.

A key feature of considering the boundary layer quantities for convergence verification was their local effects that enabled better characterization of the converged state because integrated quantities (fig. 9) did not necessarily reflect the state of convergence for the flow field. The differences between the DAF and the ILU originated from the development of the schemes. The DAF scheme suffers from significant factorization errors and the linearization of the viscous terms are very approximate. Thus, the DAF does not bode well with high aspect ratio cells, a characteristic of viscous flow field grids for capturing boundary layer gradients near a wall. Conversely, the ILU scheme does not suffer as significantly from these errors, can easily handle high aspect ratio cells, and convects flow into these cells much more implicitly, enabling better convergence of the Navier-Stokes equations. For these reasons, the ILU solutions were used for data analysis and extractions for the remainder of this report.
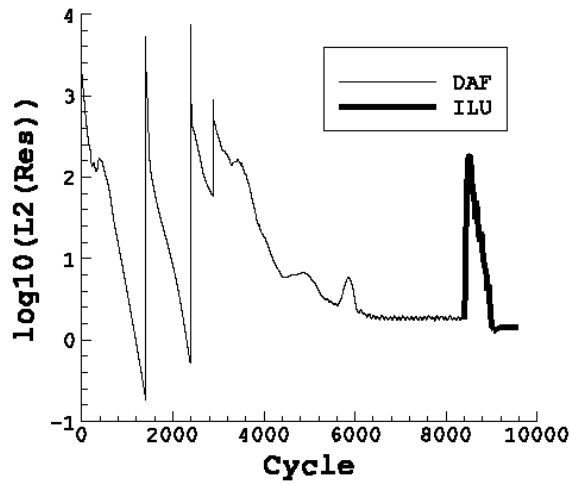
(a) Residuals.
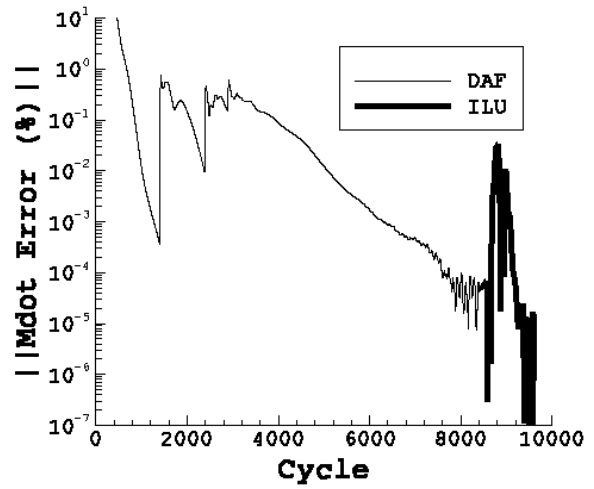
(b) Mass flow rate error.
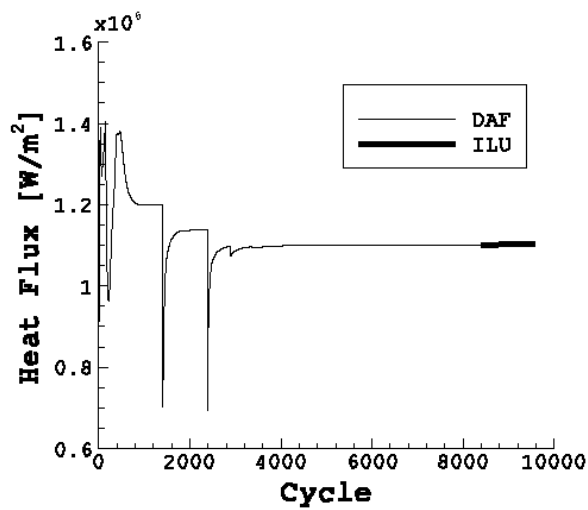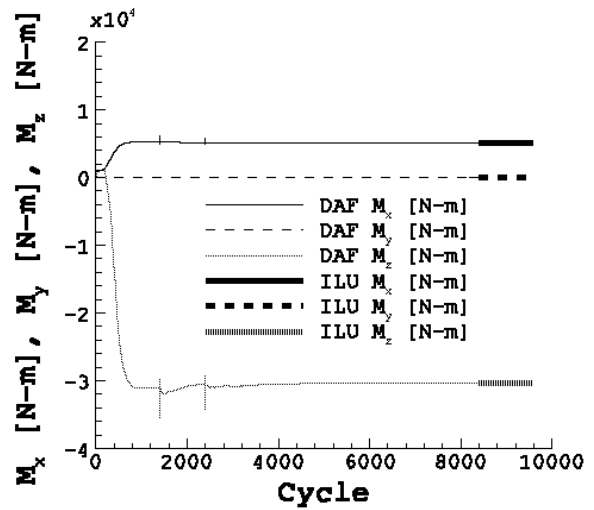
(c) Surface heating.

(d) Moments about CG.

Figure 9. Solution convergence of case 5B-D.
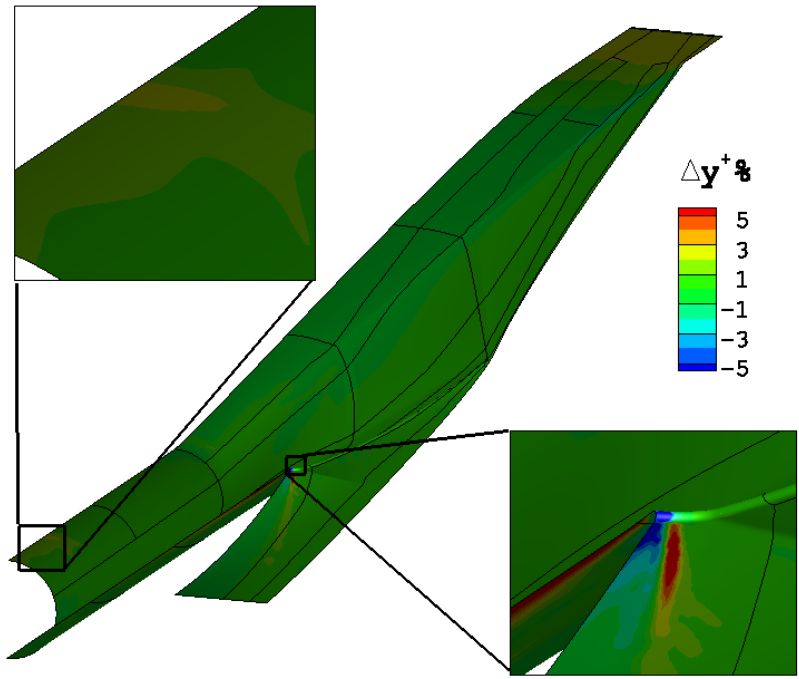
(a) Change in y^+.
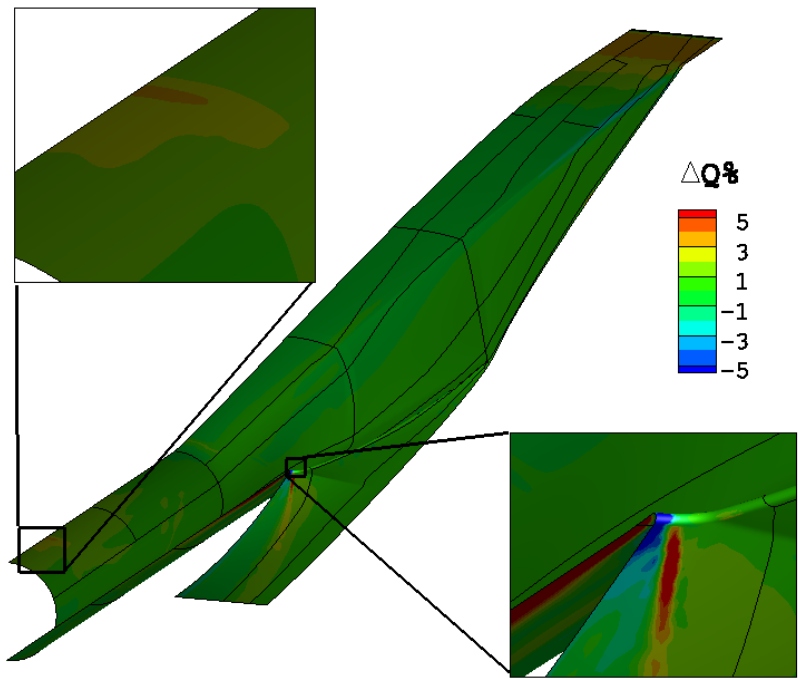
(b) Percentage change in surface heating.

Figure 10. Local boundary layer dominated property convergence of case 5B-D, between DAF and ILU solvers.
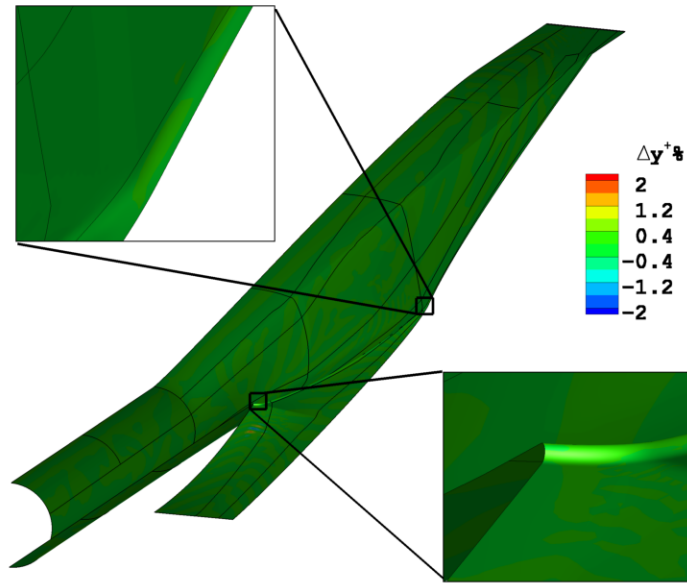
(a) Change in y^+.
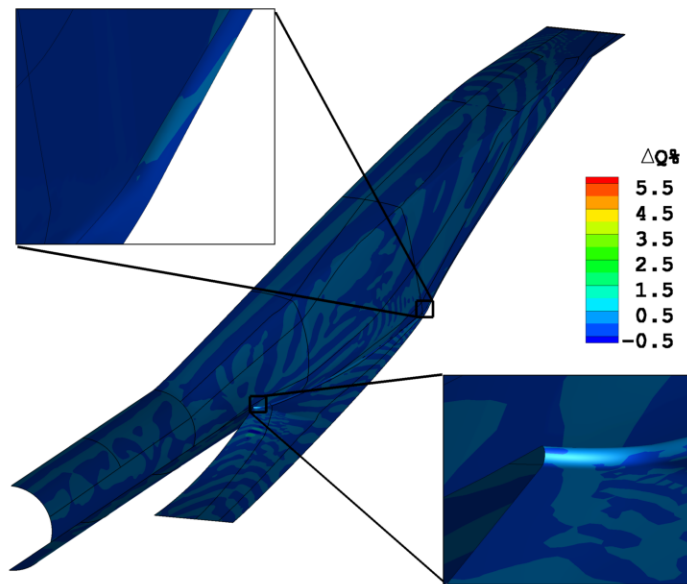
(b) Percentage change in surface heating.

Figure 11. Local boundary layer dominated property convergence of two ILU solutions with 1000 iterations between them.

5 Results

The computations performed for the design space identified in tables 1 and 2 produced a set of well converged simulations and, in some cases, inlet unstart. An unstart condition is where the initial oblique shock significantly passes ahead of the cowl leading edge, thereby lowering the incoming velocity and promoting the formation of a normal shock near the throat of the engine from a choked condition, or worse, in front of the inlet. In the case of choked flow, the shock traverses upstream from the throat preventing proper supersonic flow to the isolator towards the combustor of a scramjet engine. For the cases computed, this occurred when some of the inlets designed for higher Mach numbers were solved with a Mach 3 inflow condition. Thus, cases 5A-OD, 5B-OD, 4A-OD, 4B-OD, and 4C-OD were unable to support supersonic flow through the isolator. The remainder of the cases did have proper flow conditions, and all are explained in detail in the following sections.

Where convergence of a solution was possible, a convergence test criteria was used. The HAPB uses integrated quantities of moments, heat transfer, and others, as well as considering the $L_{2_{norm}}$ residuals. Integrated quantities are not always the best to use because individual sections within the flow domain could experience oscillations that are canceled through such an integration, as was shown in the previous section. Thus, for each case where the flow supported an operating inlet without an unstart condition, plots of the $L_{2_{norm}}$ residual, integrated quantities of the absolute value of the percentage error in mass flow rate, moments, and heat flux are provided to determine the extent of convergence. Additional surface plots are provided as indicators of flow field parameters and the effects they illustrate, such as surface shear, Mach number, y+, and surface pressure. In the case of y+, since wall matching boundary conditions were used to model the boundary layer, the y+ value target should be within 100.

Although most of the data about to be presented may seem repetitive, attention to details in the data was made to understand underlying trends between the design parameters. For this reason, the bulk of the computations are shown as opposed to describing just a few cases because the exploration of the data is not possible without the additional plot information contained within each of the following sections. After the solutions, there is a summary of trends to help explain why the details of each solution are presented.

5.1 Case 5A-D

Case 5A-D was the highest contraction ratio design computed. The design objective for this particular inlet was to serve as the upper contraction limit for the inlets computed, with a desired one atmosphere of pressure at the throat of the inlet. Based on VULCAN results for the on-design Mach number of five, the total pressure recovery for this inlet was 0.6694 with an average static pressure of slightly more than one atmosphere in the throat. The convergence was determined from the plots shown in figure 12.

Based on the global parameters from the VULCAN run, the mass flow rate error shown in figure 12(b) is the most sensitive indicator for convergence. For this reason, the mass flow rate error was used as the primary indicator for convergence of the remaining solution. When this value hovered at a value sufficiently close to zero, the solution was considered converged. Also noteworthy is that the implicit solver does improve the convergence of the solution, as was shown in section 4.1.

Globally, the surface properties are shown in figure 13, some with two views so that both cowl and inlet lip sides of the inlet can be seen, and show a variety of details. First, in the Mach number contours, the flow field had a usable core, which was more significant than that usually
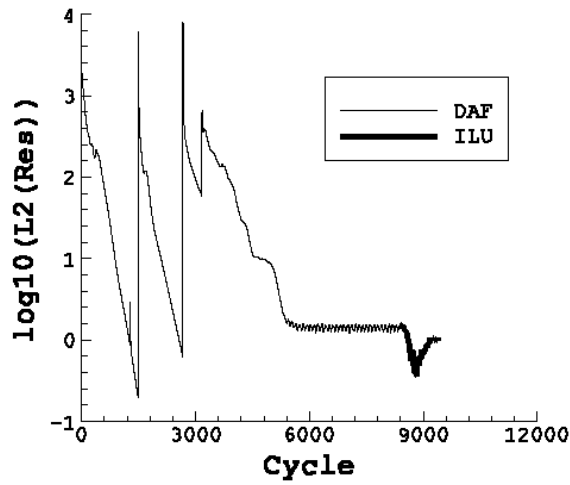
(a) Residuals.
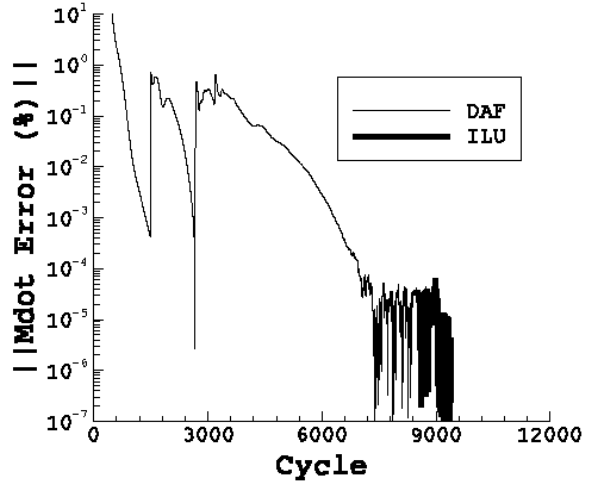
(b) Mass flow rate error.
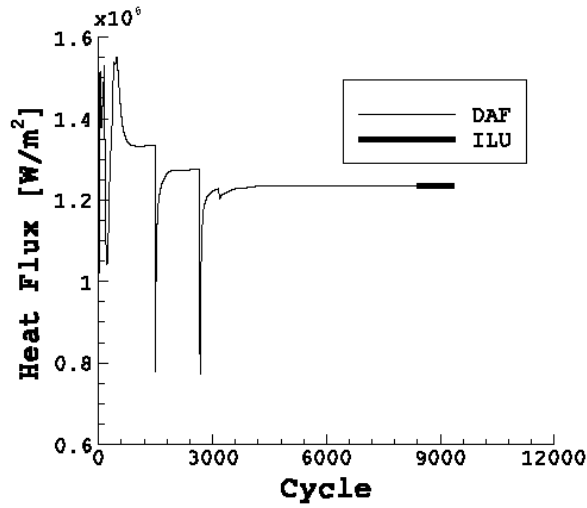
(c) Surface heating.
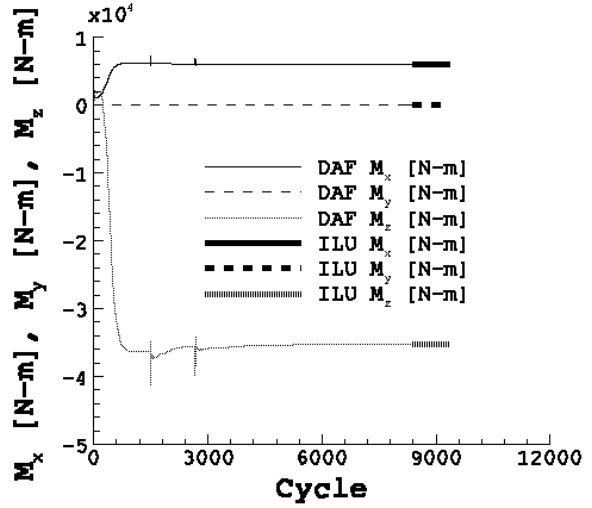
(d) Moments about CG.

Figure 12. Solution convergence of case 5A-D.

found in demonstration flight sized inlets [21]. For this case, the core flow made up more than 25 percent of the cross-sectional area for the larger inlet by comparison to 13 percent in similar flow conditions in the smaller inlet; a doubling of the core unaffected by wall viscous forces. The surface pressure of the inlet surface did not rise significantly until downstream of the closing of the inlet, indicative of the oblique shock raising the pressure in the notch region. Upstream of that region, the surface streamlines also indicated generally slowly compressed flow from the incoming air to the inlet. As internal shocks process the flow, the streamlines began to diverge and coalesce along the sides of the inlet. But as the processed air continued aft beyond the throat, the flow field began to exhibit more uniformity, possibly a desirable feature for fluid entering the combustion region of the engine. The same could be seen in the total surface shear whereas the y^+ data indicated rapid

24

changes in boundary layer properties particularly near the internal shockwaves of the flow domain. Throughout the remainder of this chapter, the total surface shear is the root sum square of the magnitude of the surface shear components multiplied by the sign of the axial shear component so that regions of separation can be detected.
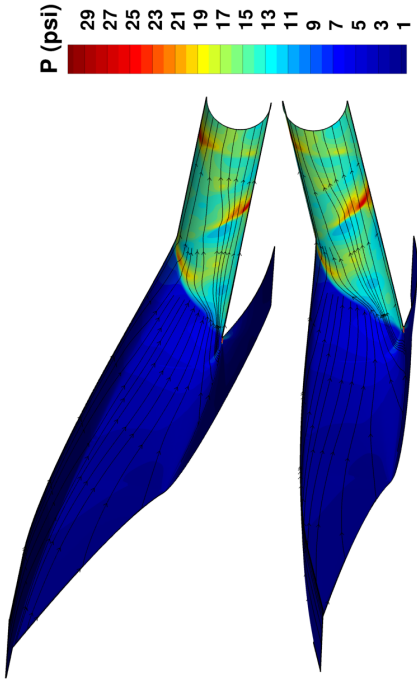
(a) Surface pressure.
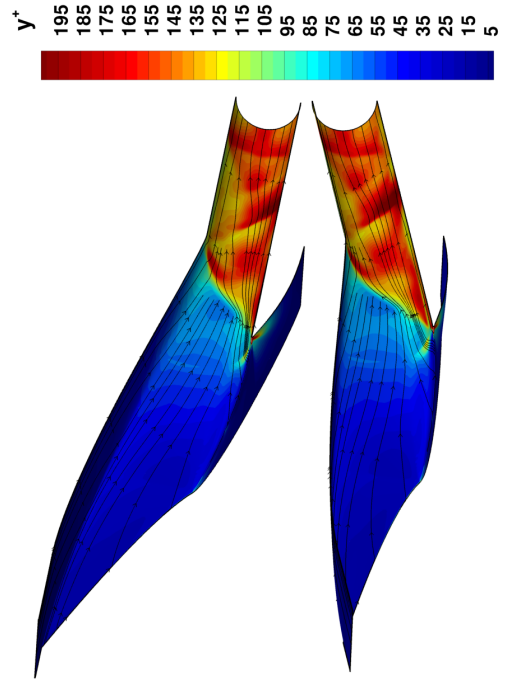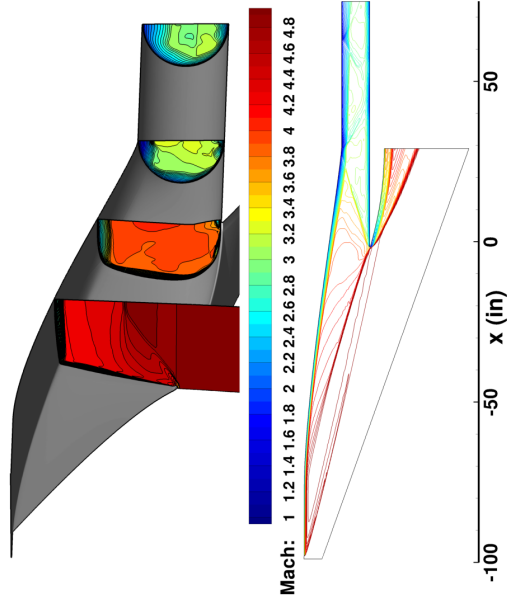
(b) Mach number.
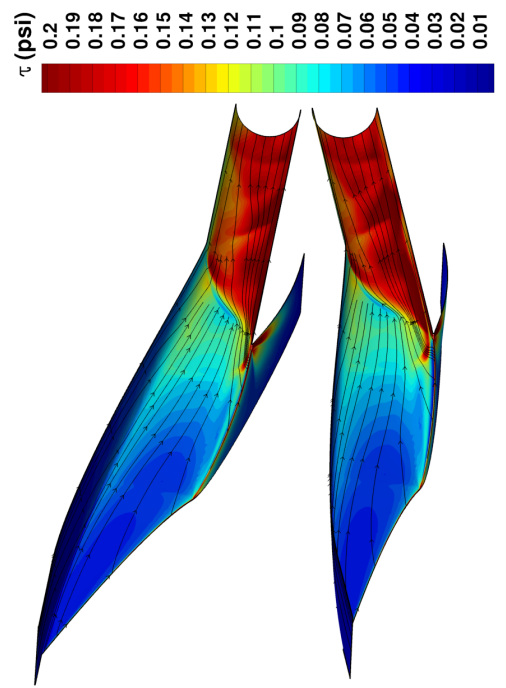
(c) Surface y^+.

(d) Total surface shear.

Figure 13. Surface properties of the flow field of case 5A-D.

The plots shown thus far are predominantly surface data. Enhanced visualization of the three-dimensional flow field structure is accomplished using a numerical Schlieren plot. Figure 14 was developed using an absolute gradient of density contoured with a grayscale to generate the numerical Schlieren plot.
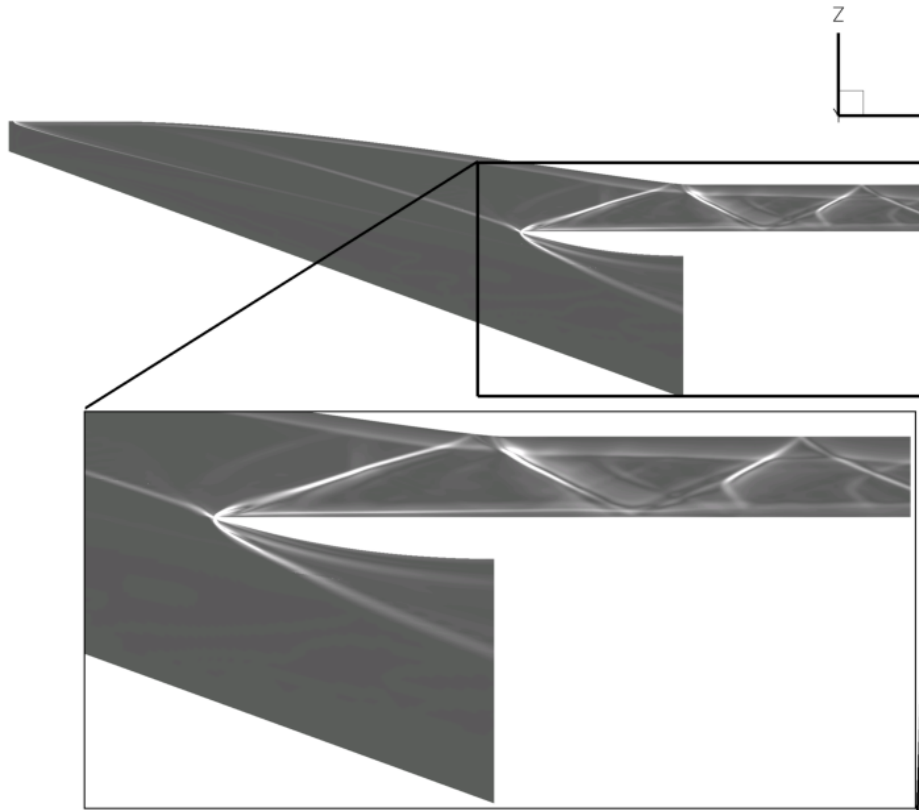
Figure 14. Numerical Schlieren of the symmetry plane of case 5A-D.

The numerical Schlieren image generated for this case shows more information than can be easily determined from the Mach contours of the flow field. In particular, the flow is three-dimensional. The flow structures show a variety of interesting aspects. First, the front lip oblique shock dissipated rapidly, indicating the fluid entering the inlet was more uniform than might have been anticipated. Second, the boundary layer appeared to thicken more rapidly between reflected shocks, not necessarily because of the viscous stresses but quite possibly because of the additional shock structures interacting with the wall bounded boundary layer. The internal shock waves also were not as sharp as might have been seen in two dimensions after the notch region because the three-dimensional shocks were also interacting with the dominant reflected shock waves. Generally, the numerical Schlieren provides more information about why this region of the inlet flow was indeed so complex. During the latter discussion of possible changes to affect the fluid, the numerical Schlieren images will be used more extensively.

5.2 Case 5A-OD

Assessing the inlet at the design Mach number is important to ensure the inlet will operate, as designed, to produce good flow characteristics into the combustor from the isolator section. However, the Mach 3 off-design case is also important so as to understand the possible range of operating flow conditions for this inlet. As such, figure 15 shows the convergence information for this solution.

(a) Residuals.

(b) Mass flow rate error.

(c) Surface heating.

(d) Moments about CG.
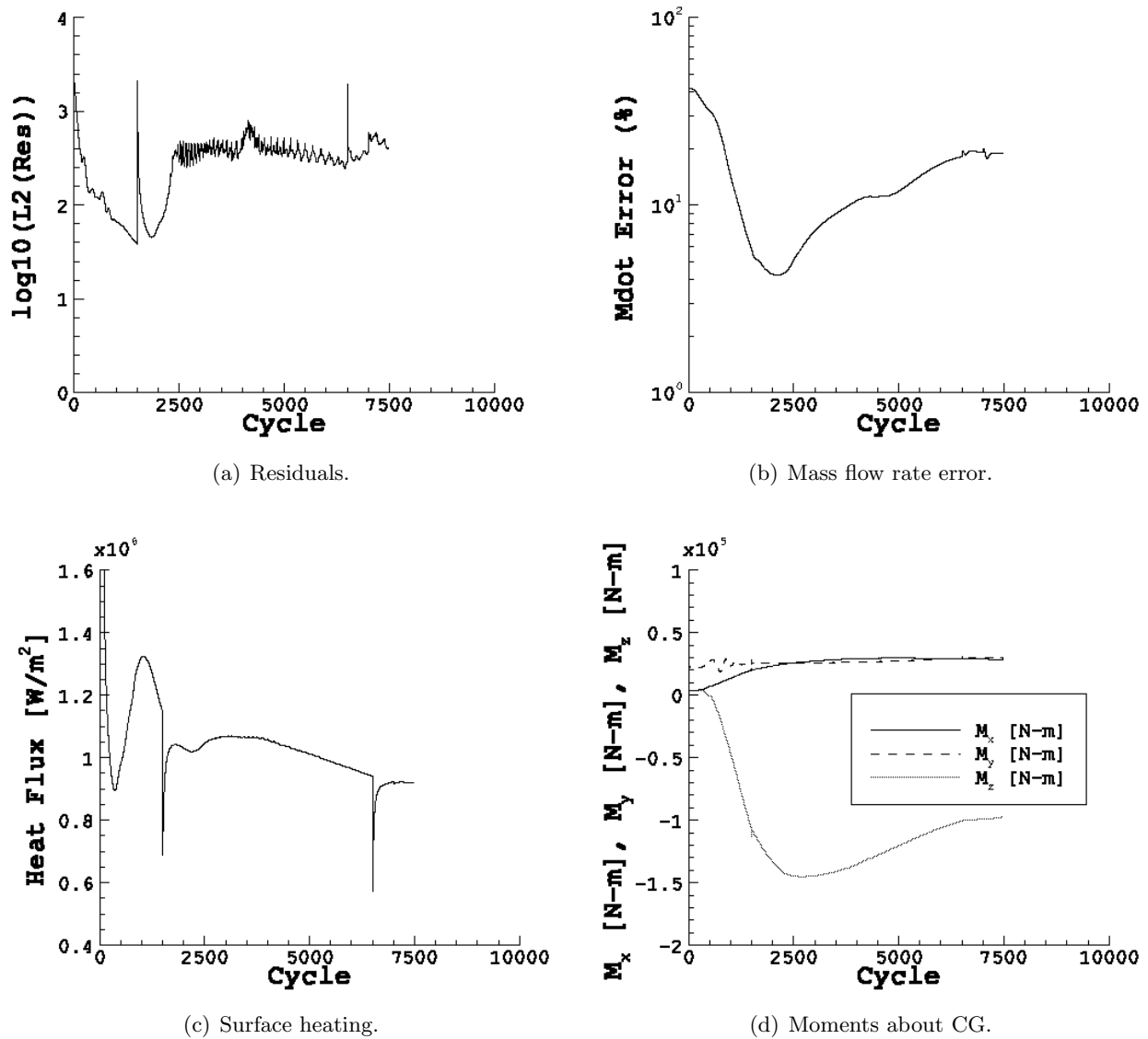
Figure 15. Solution convergence of case 5A-OD.

Based on the convergence information and using the same parameters to control the flow solver, the results would suggest that the solution did not converge well. This is typical of an unstart condition for the inlet solution. In the inlet, an unstart usually occurs because of choked flow at the throat, which causes the formation of a normal shock that begins to travel upstream. As the

normal shock exits the inlet section near the notch, where the inlet is considered to have a closed condition indicated by walls encompassing the flow, the normal shock induces subsonic flow in the interior of the inlet, and the inlet cannot produce the desired supersonic flow needed at the combustor. Although this phenomenon can be seen in the surface properties and Mach contours of the flow field, as illustrated in figure 16, the flow inside the inlet is subsonic. With subsonic flow inside the inlet, the outflow boundary condition is ill posed, and the solution beyond the normal shock is worthless but is shown for the completeness of the cases computed.
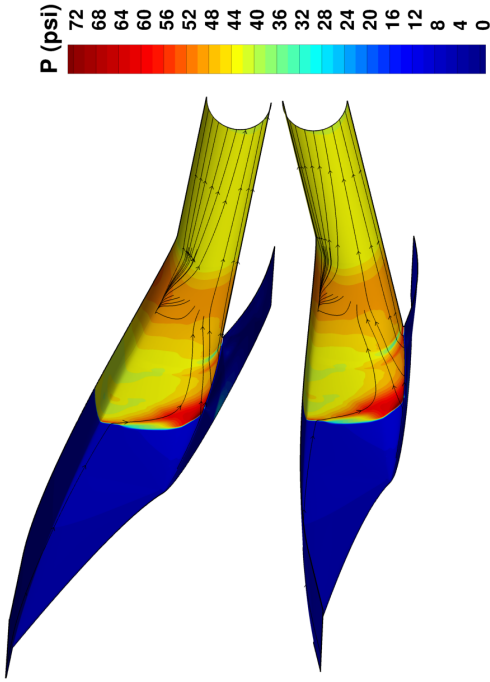
(a) Surface pressure.
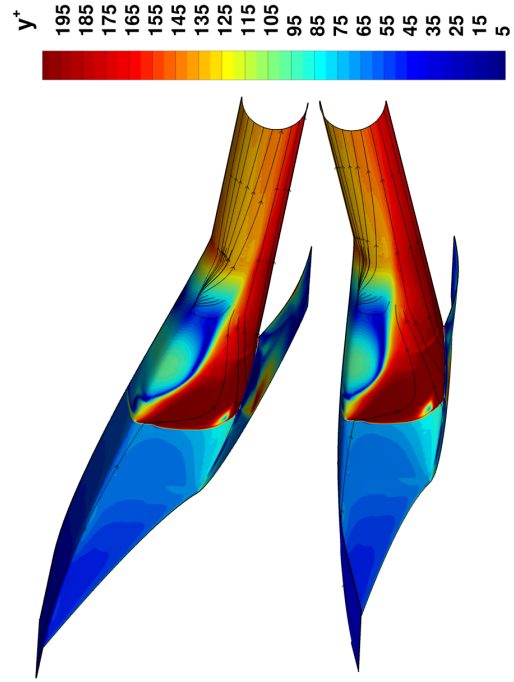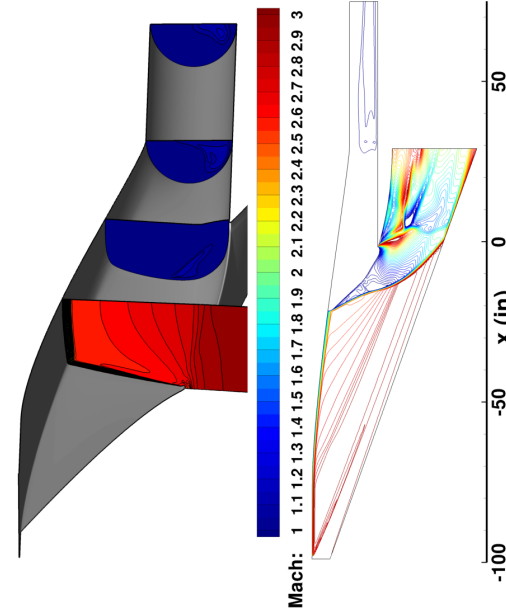
(b) Mach number.
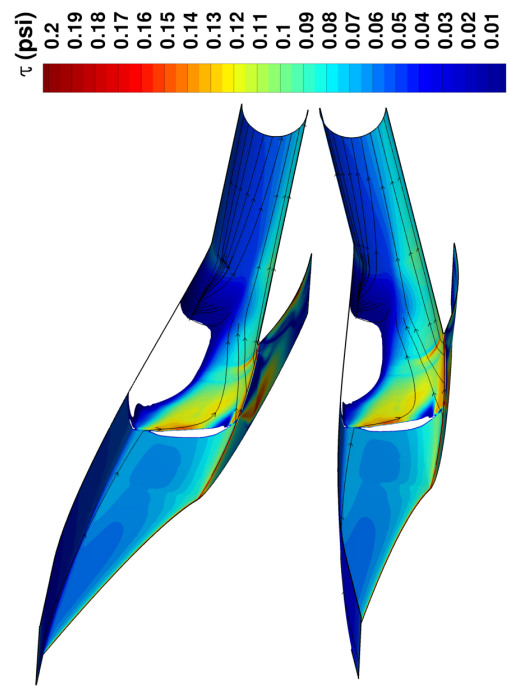
(c) Surface y^+.

(d) Total surface shear.

Figure 16. Surface properties of case 5A-OD.

More telling than these plots is the numerical Schlieren of the symmetry plane shown in figure 17. Clearly the normal shock is located ahead of the notch of the inlet, and the flow field aft of this normal shock splits between the interior of the inlet while some is diverted away from the inlet. This unstart condition was highly unstable, resulting in severe loading and high drag on the inlet. Though this may not be the limit of the operation of the inlet, this information may provide an indicator of how low the inlet can be operated below its on-design Mach number.
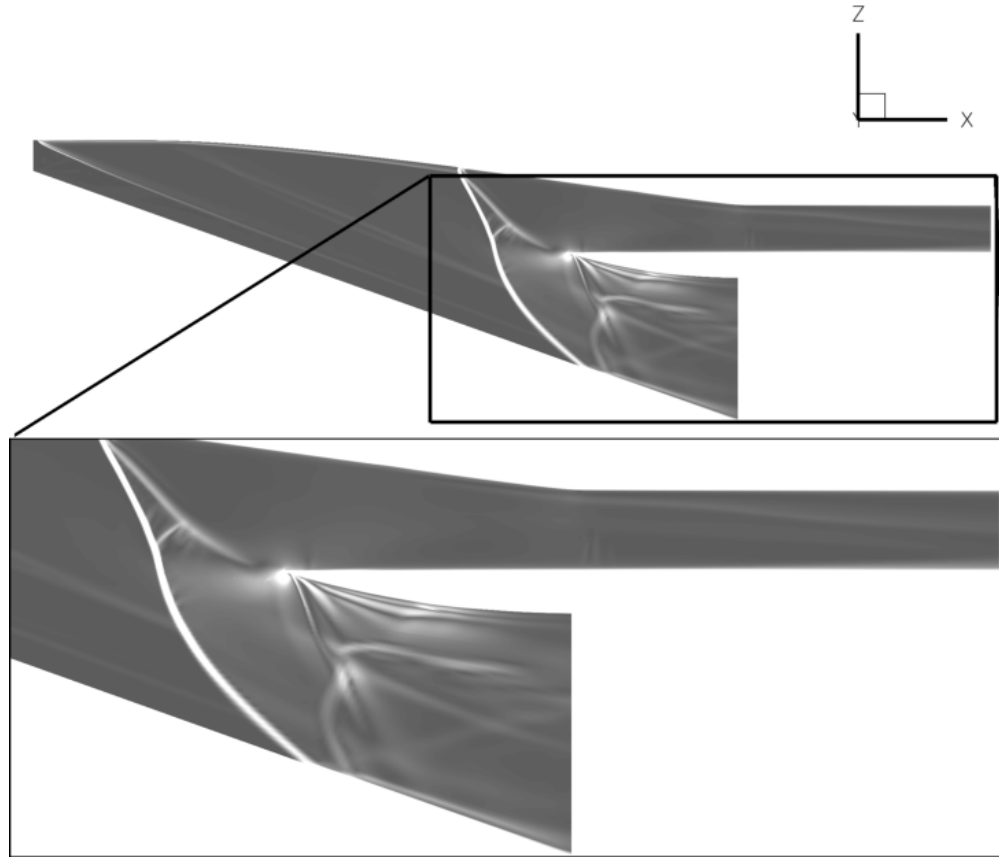
Figure 17. Numerical Schlieren of the symmetry plane of case 5A-OD.

5.3 Case 5B-D

Case 5B-D was designed for a contraction ratio that would produce a pressure that was nearly three quarters of an atmosphere of pressure at the throat of the inlet, or what is typically called the inlet exit. At the throat of the inlet, the average static pressure was approximately 13 psi, or roughly seven-eighths of an atmosphere with a pressure recovery of 0.6789. Figure 9 (section 4.1) shows the convergence results of this solution. Similar to Case 5A-D, the mass flow rate error converged the slowest but was nearly zero, indicating the flow parameter had converged. This case was the one used to determine the overall level of convergence in section 4.1. Globally, the surface properties for surface pressure, Mach number, y+, and surface shear are shown in figure 18.

(a) Surface pressure.

(b) Mach number.

(c) Surface y^+.

(d) Total surface shear.
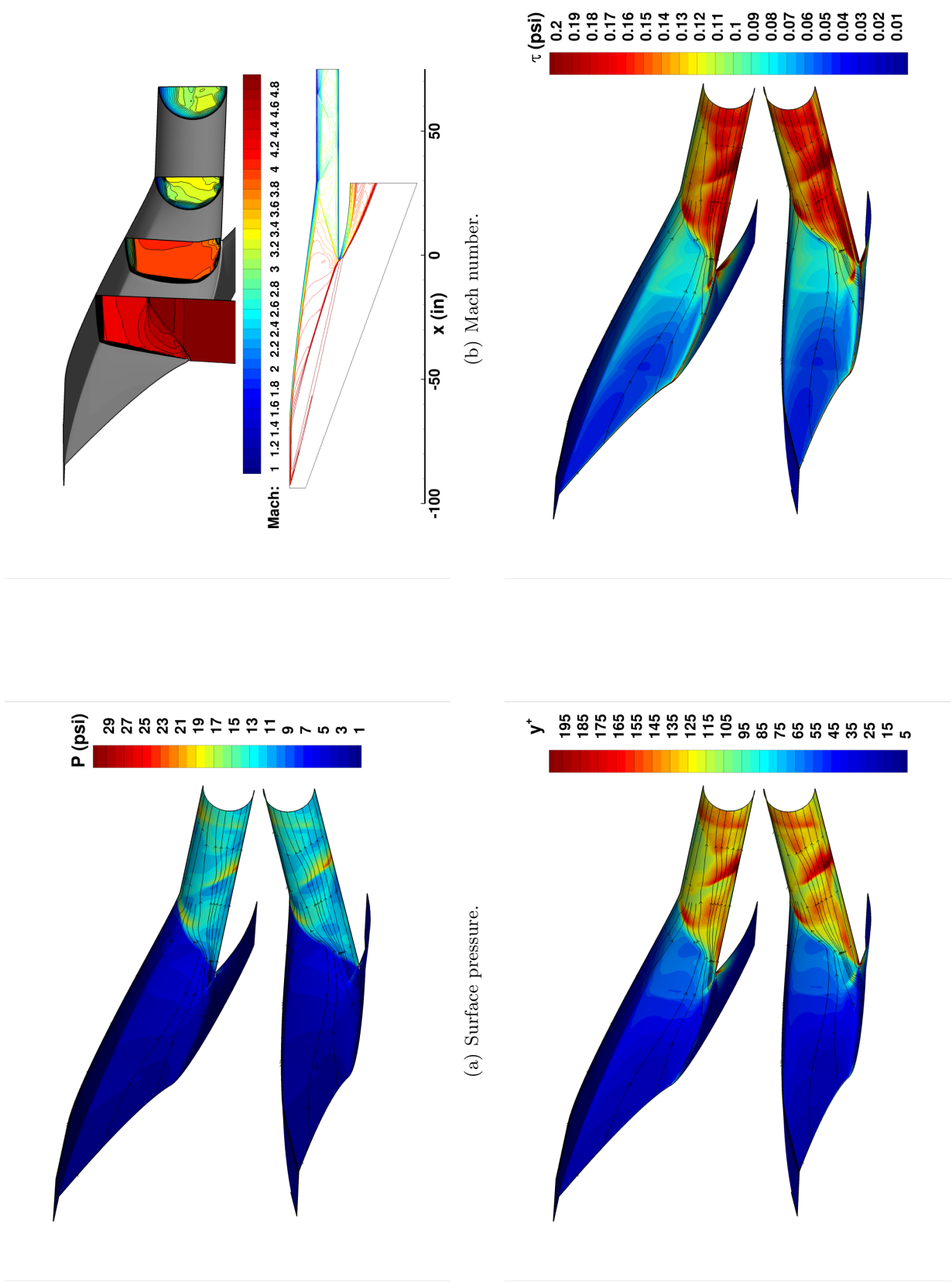
Figure 18. Surface properties of case 5B-D.

Geometrically, the inlet was shorter than the 5A-D, but the flow features were quite similar. The y+ values remained in the range of 100 for the bulk of the computation, but higher values existed near regions of shock impingement on the sides of the inlet. Total surface shear did not indicate separated regions, so the flow processed towards the isolator exit. Considering the numerical Schlieren shown in figure 19, at the isolator exit the primary reflected shock was moving towards the top of the inlet by comparison to figure 14. The shallower shock angles combined with lower contraction due to reduced area from case 5A-D to case 5B-D causes this change in ending shock location.
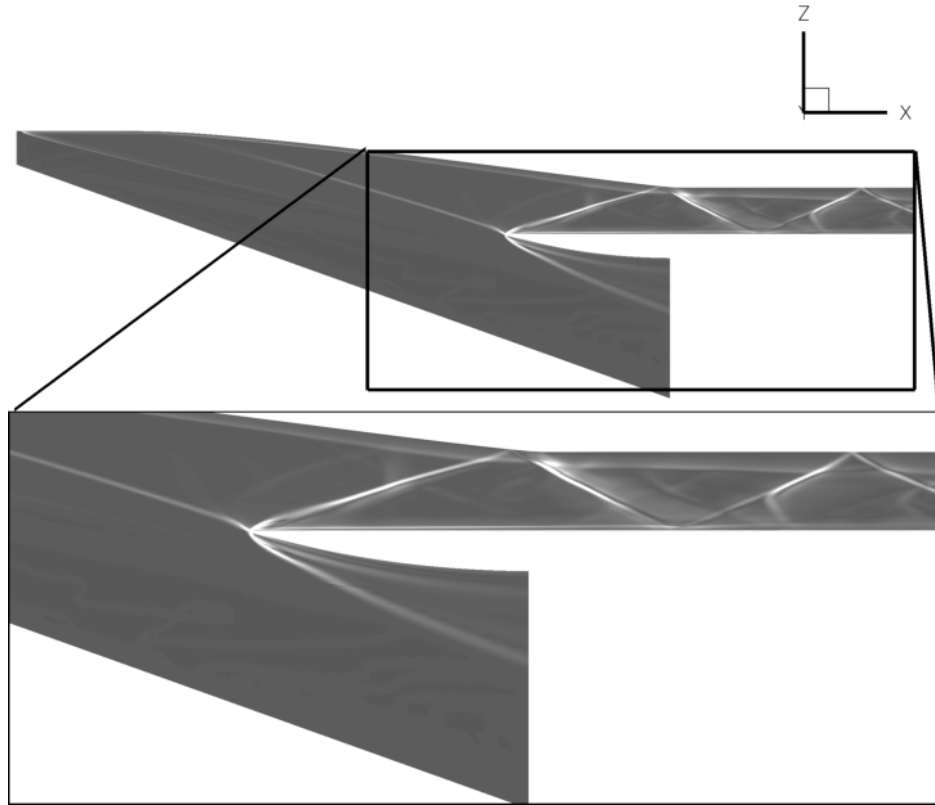
Figure 19. Numerical Schlieren of the symmetry plane of case 5B-D.

5.4 Case 5B-OD

Similar to the 5A-OD case in section 5.2, this case experienced an unstart condition as illustrated by the convergence data shown in figure 20. The flow solver performed similarly to the 5A-OD case. As such, the surface parameters shown in figure 21 show that a normal shock is poised outside the inlet notch, resulting from choked flow at the throat.
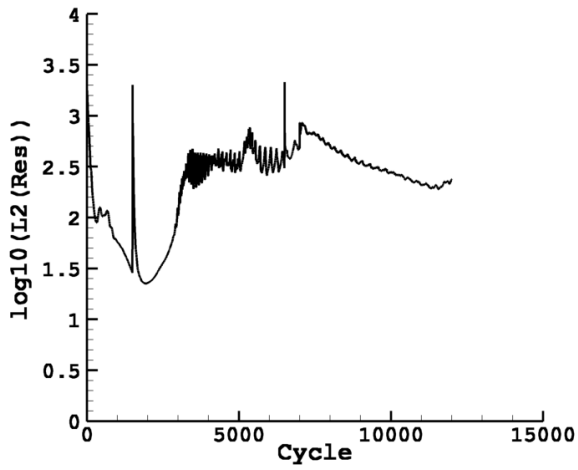
(a) Residuals.
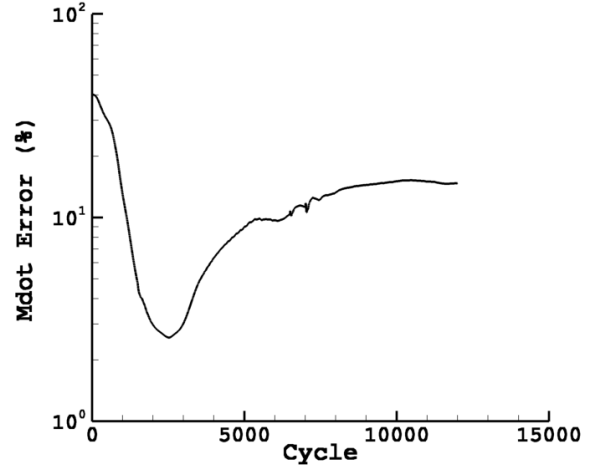
(b) Mass flow rate error.
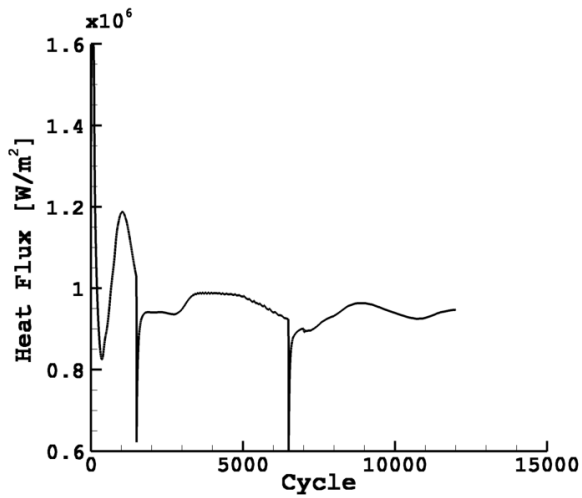
(c) Surface heating.
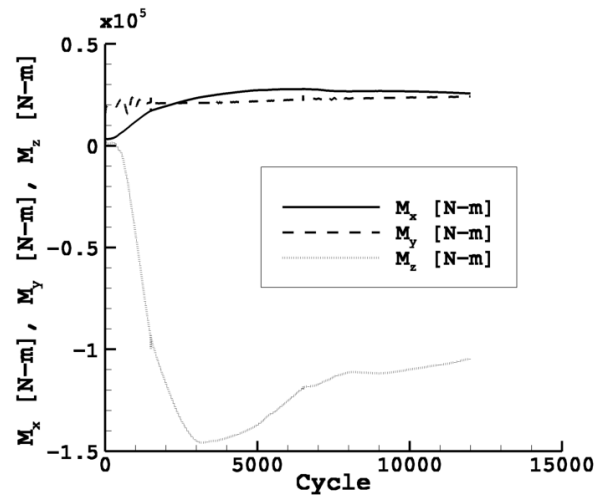
(d) Moments about CG.

Figure 20. Solution convergence of case 5B-OD.

(a) Surface pressure.

(b) Mach number.
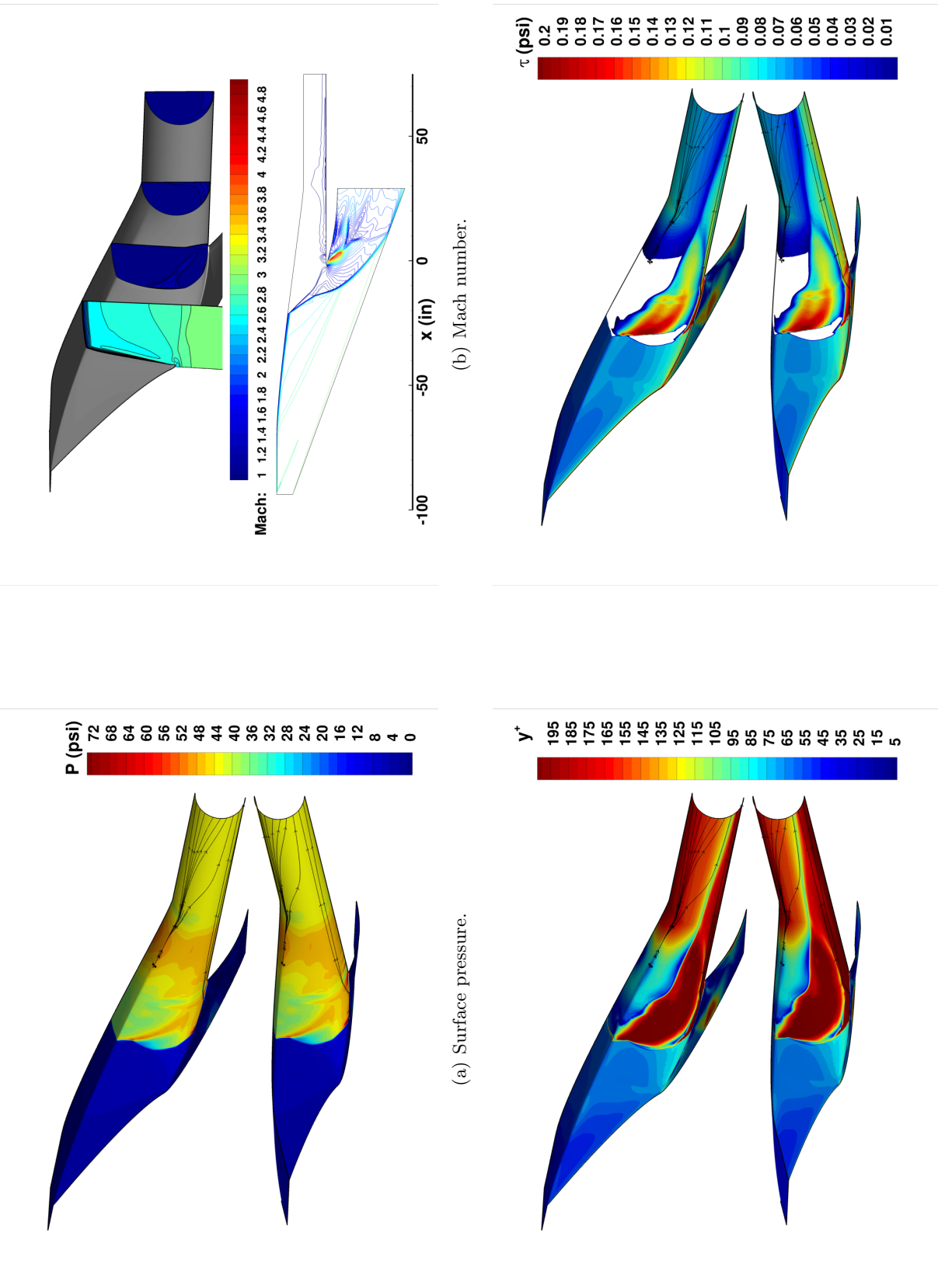
(c) Surface y^+.

(d) Total surface shear.

Figure 21. Surface properties of case 5B-OD.

Interesting to note in these surface properties is that the separation region indicated by negative shear was similar to the longer 5A-D inlet. Similarly, the shock structure shown in figure 22 illustrates the same phenomenon as the 5A off-design. There was a strong normal shock ahead of the inlet close at the notch, most likely produced by a choked flow at the throat.
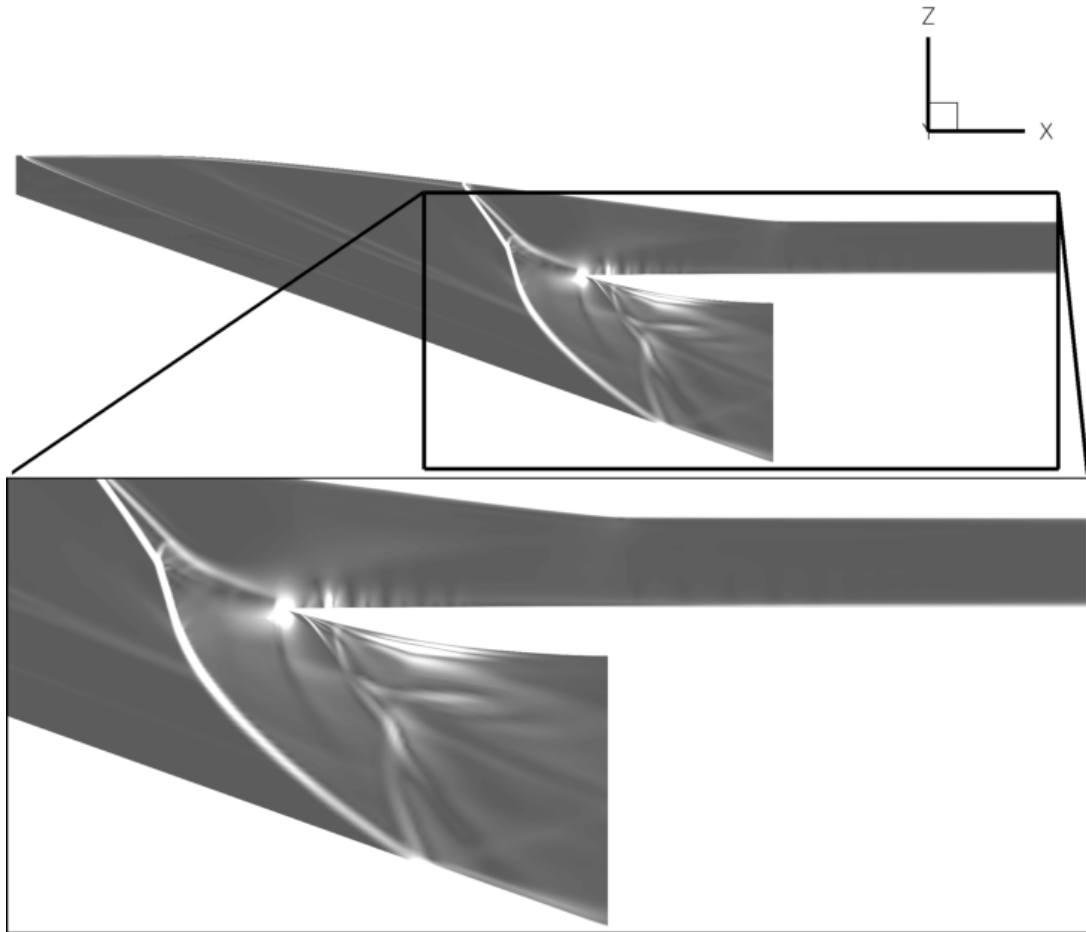
Figure 22. Numerical Schlieren of the symmetry plane of case 5B-OD.

The shock patterns inside the inlet indicated that normal shocks beyond the notch set up as the flow expanded around the notch. Additionally, with the impinging shock at the outer boundary of the flow domain, the mass flow rate into the domain changed because the boundary condition was no longer valid. This was another indication of the flow field state, and pictorially, the unstart condition is conclusive.

5.5   Case 5C-D

Case 5C-D was designed as an intermediate contraction ratio for a throat pressure of half an atmosphere. From the performance data, this inlet had an average static throat pressure of approximately 8 psi with a pressure recovery of 0.6679. Figure 23 shows the convergence of this solution.
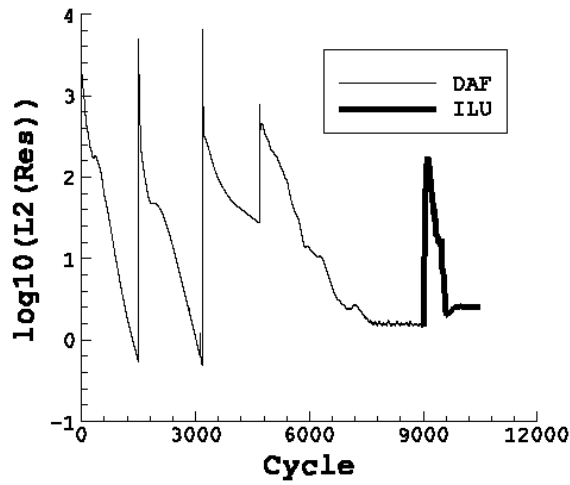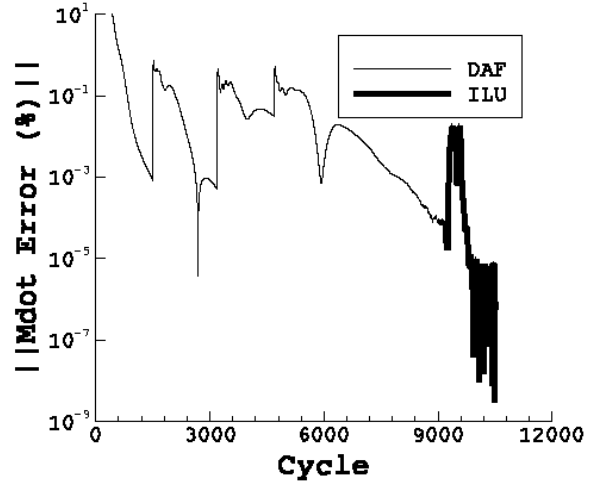
(a) Residuals.

(b) Mass flow rate error.
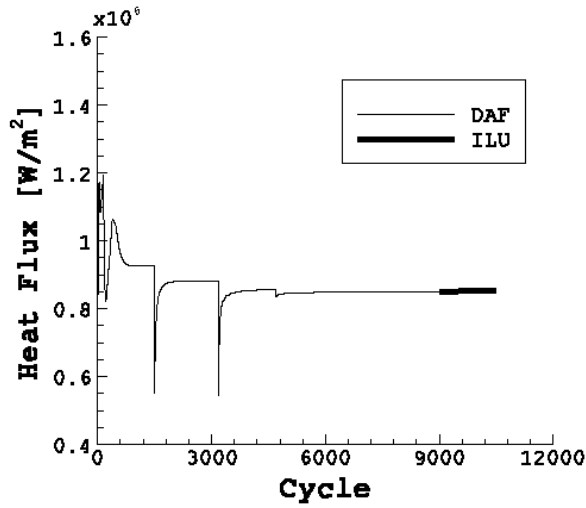
(c) Surface heating.
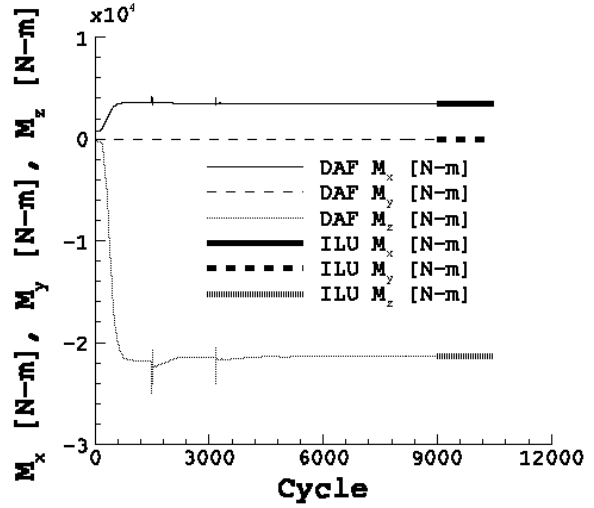
(d) Moments about CG.

Figure 23. Solution convergence of case 5C-D.

In figure 23, the log of the L2 norm residuals dropped by four orders of magnitude, the mass flow rate error was close to zero for both DAF and ILU solvers, and the integrated quantities of surface heat transfer and three moments were constant. In fact, the differences were almost negligible. What is interesting to note though is that convergence was taking several thousand more iterations than case 5A-D. Considering the surface properties shown in figure 24, the y+ values were decreasing in magnitude by comparison to previous cases, as was the surface pressure. Total surface shear indicated a fully attached flow.
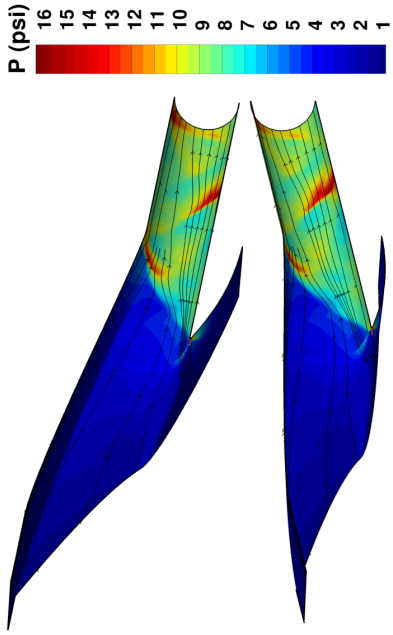
(a) Surface pressure.
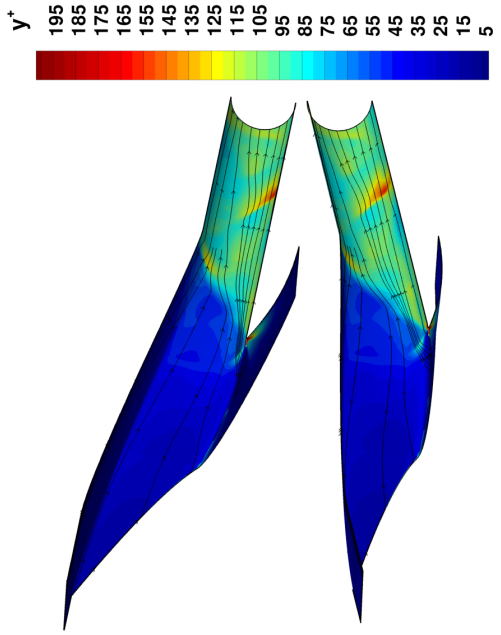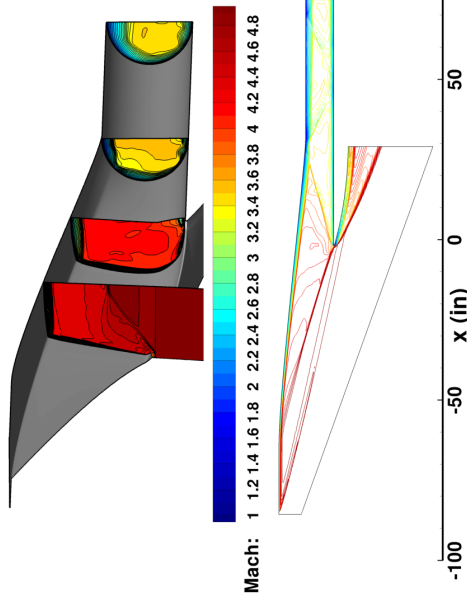
(b) Mach number.
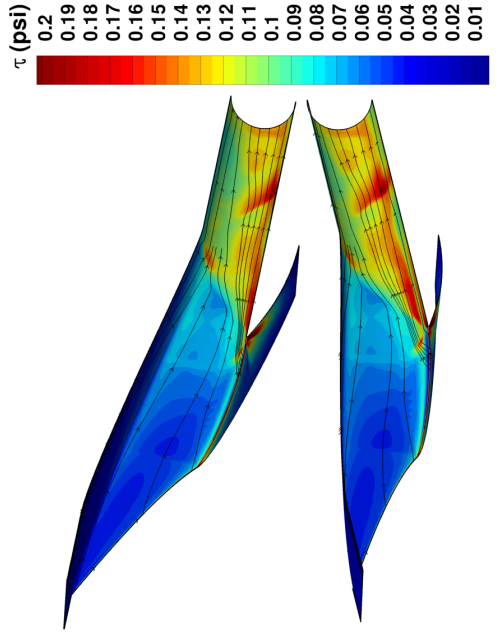
(c) Surface y^+.

(d) Total surface shear.

Figure 24. Surface properties of case 5C-D.

Further investigation of the shock structure shown in figure 25, illustrates that the reflected shock at the exit of the isolator was impinging closer to the top of the inlet, a consistent trend seen from comparing previous cases 5A-D and 5B-D. The lip shock at the beginning of the flow domain also diminished quicker, and the strength of the shock at the notch is not as significant. Overall, as the inlet length shortened and the capture area decreases from a reduced contraction ratio design parameter, the shocks tended to be less intense. This is counter to typical shock relationships when only considering shock angles because the front shock angles from the lip are approaching normal shock features which would produce significantly more compression and more pressure loss. The reduction in area to process the flow counteracts the effects of a less oblique shockwave.
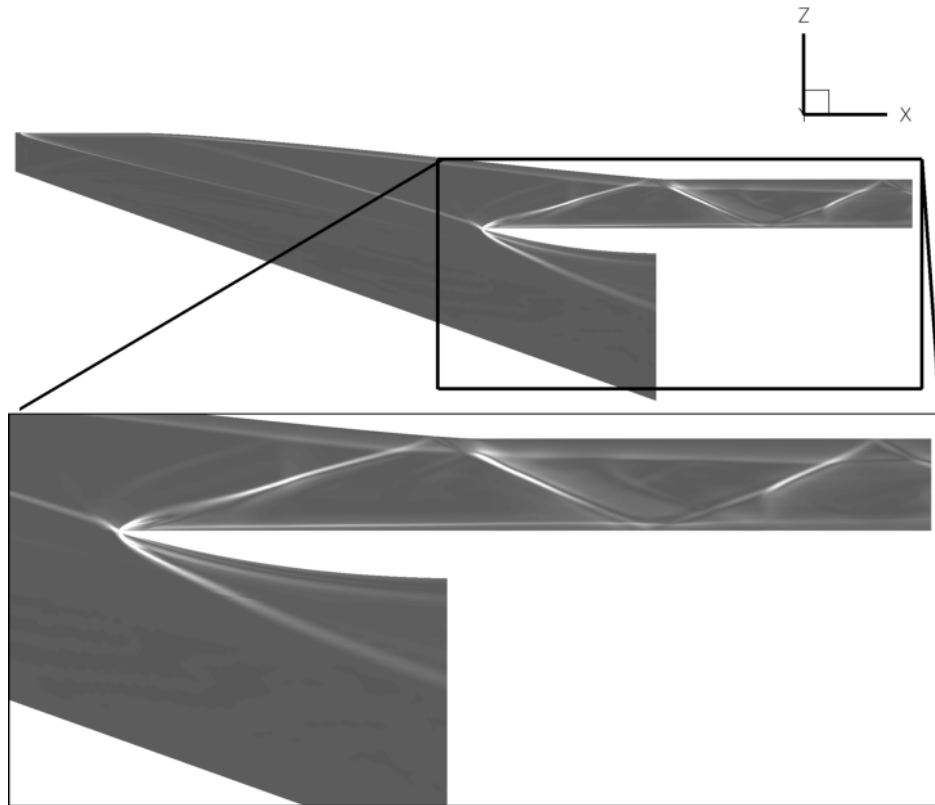
Figure 25. Numerical Schlieren of the symmetry plane of case 5C-D.

5.6   Case 5C-OD

Unlike cases 5A-OD and 5B-OD, the off-design Mach number computation for the 5C-OD case did remain started and had a total pressure recovery of 0.8276. Figure 26 shows convergence of this solution.

Considering the monitored parameters for convergence, the log of the L2 norm of residuals from the DAF scheme appeared to converge four orders of magnitude. The ILU convergence dropped the level of convergence another order of magnitude, but during the use of the ILU, large CFL numbers were not possible without solver divergence. While most of the solutions where the ILU was used had CFL numbers at 100, this particular case would not sustain values larger than 20.
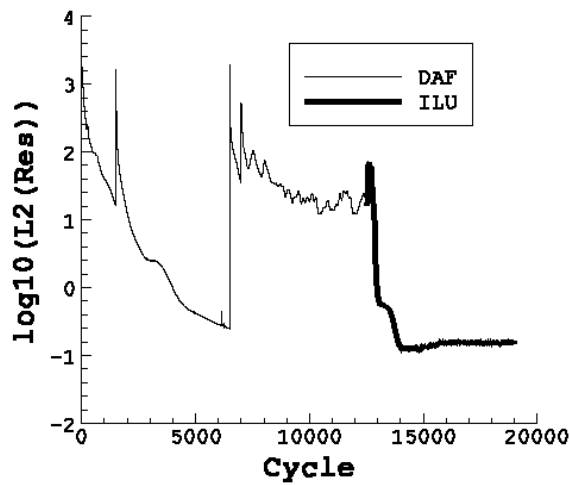
(a) Residuals.
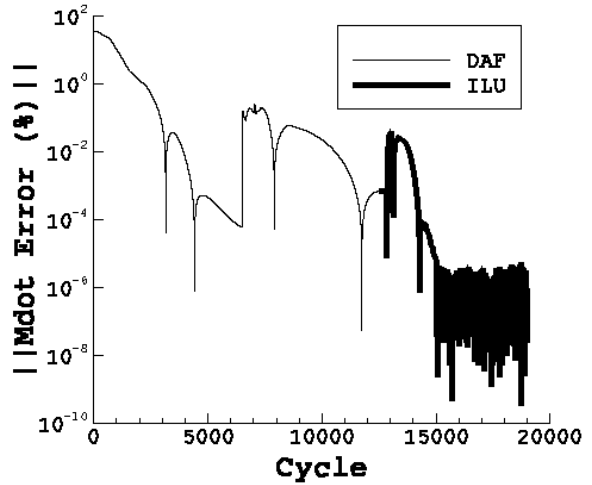
(b) Mass flow rate error.
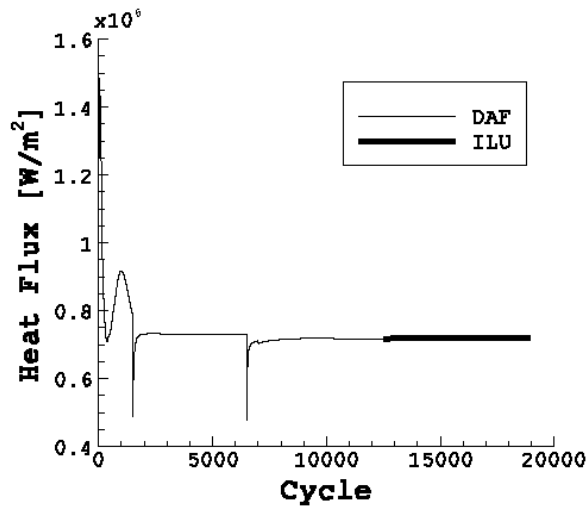
(c) Surface heating.
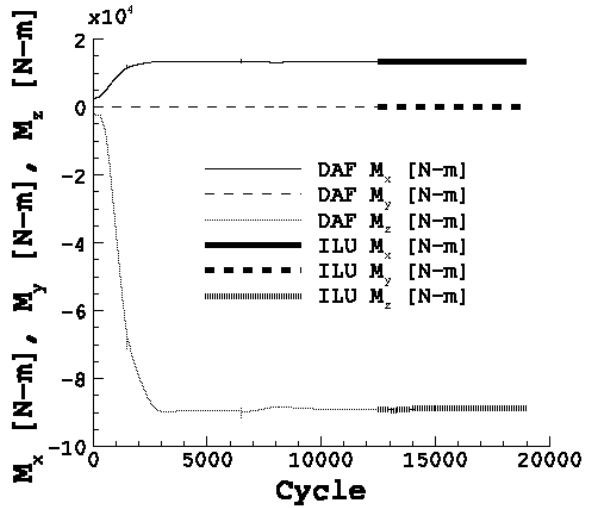
(d) Moments about CG.

Figure 26. Solution convergence of case 5C-OD.

Similarly, the mass flow rate error was low for the DAF convergence, yet the ILU did take the level of convergence significantly lower. Unlike the first two measures, the integrated quantities remained constant for the DAF and ILU solutions, indicating good convergence of the flow field.

The surface properties for pressure, Mach number, shear, and y+ (fig. 27) illustrate that the flow is indeed attached from the surface shear, but internal pressures are much higher and the number of reflected shocks appears to be significant by comparison to the on-design Mach number case. This was to be expected. At on-design conditions, the internal shocks should have been nearly canceled. For the lower Mach number off-design condition, the Mach angles were all steeper, and a completely different shock structure set up inside the inlet.
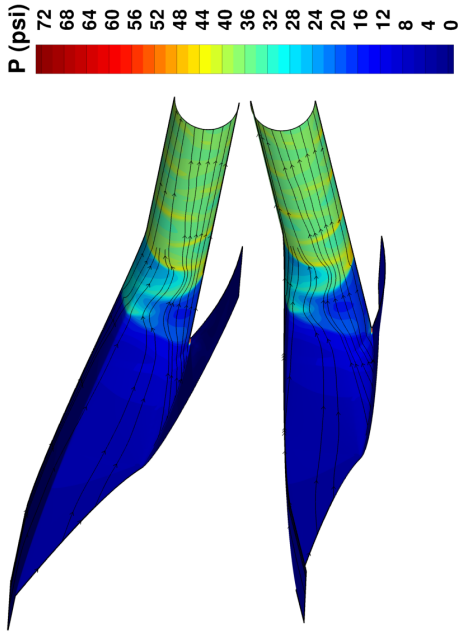
(a) Surface pressure.
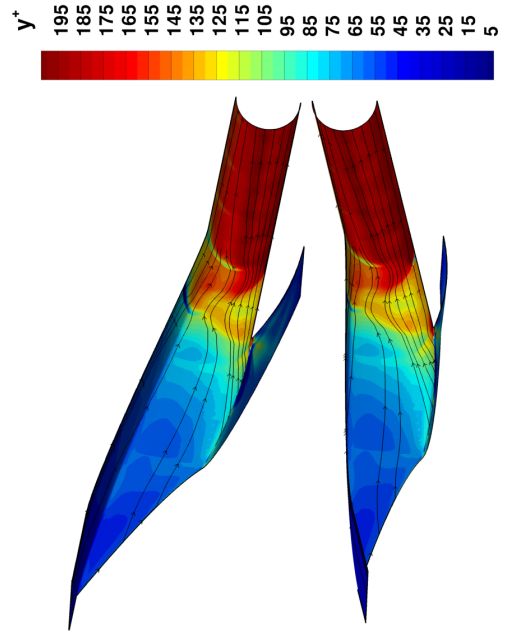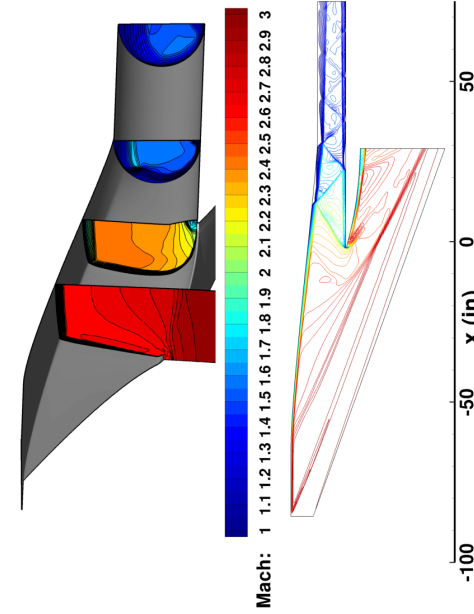
(b) Mach number.
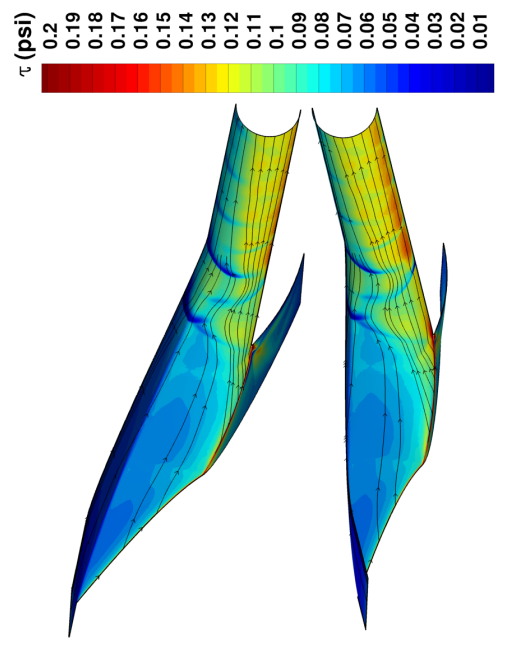
(c) Surface y^+.

(d) Total surface shear.

Figure 27. Surface properties of case 5C-OD.

Within the flow field, the y+ values were then much larger, and the core of the flow was not easily detectable. In the post-processing section of the data, a more detailed evaluation of core flow will be discussed but the flow in this case was not in an unstart condition. Further investigation of the shock structure with the numerical Schlieren shown in figure 28 illustrates the significant shock reflections.
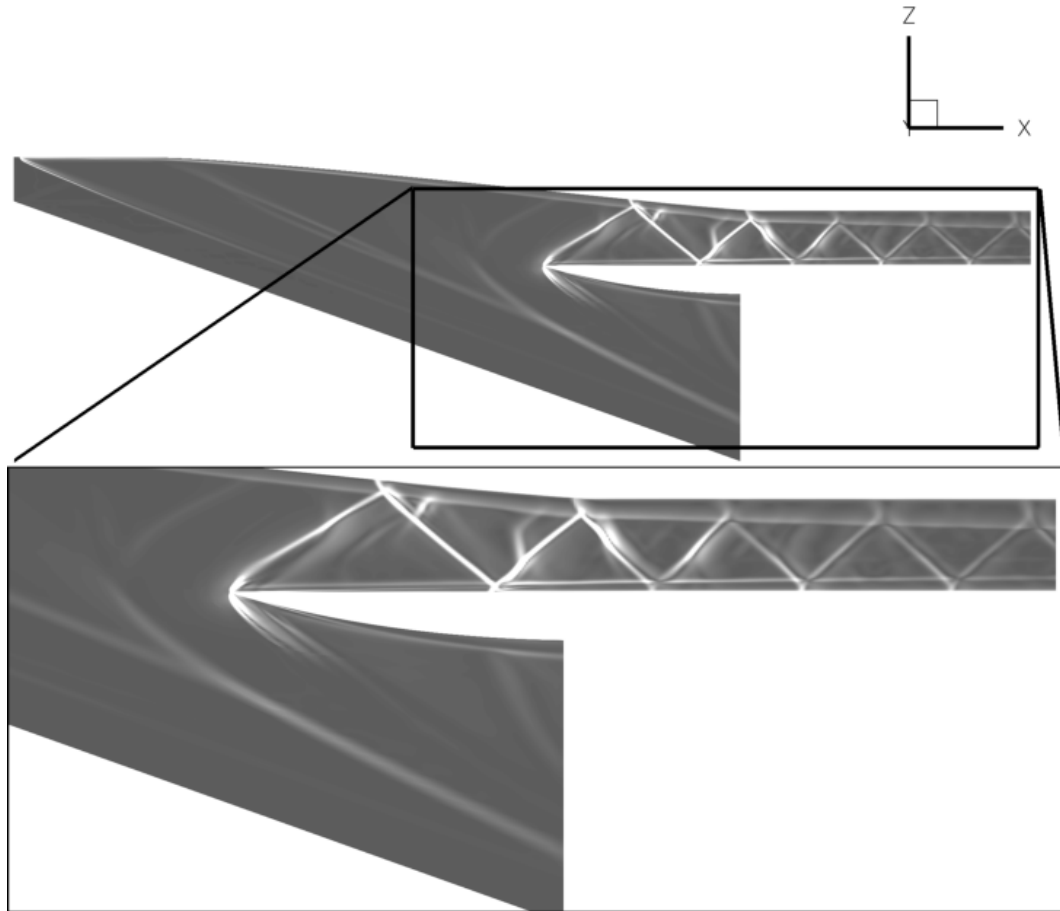
Figure 28. Numerical Schlieren of the symmetry plane of case 5C-OD.

Additionally, the shock structure showed a weak cowl-shock ahead of the inlet notch, though it was not significant enough to cause the inlet to unstart. This was a result of the off-design inflow Mach number. Waves from the three-dimensional compression arrived at the symmetry plane upstream of the notch because of the steeper wave angles. As the contraction ratio dropped, the strength of the shock waves also diminished. With the added shock reflections, the boundary layer thickness was also seen to be increasing by comparison with the Mach 5 condition. While the inlet remained started, and the total pressure recovery was 0.8276, the usefulness of this inlet may be better due to significant flow mixing. Flow in this inlet was heading into the combustor through repeated shock reflections, which could cause pressure losses each time the fluid encountered a shockwave. Even though the total pressure recovery was reasonable, the significant number of shock reflections could benefit the combustion process by improving mixing of the flow constituents.

5.7 Case 5D-D

Case 5D was the lower limit of the inlet contraction ratios, determined from the Kantrowitz self start limit, based on the inviscid average Mach number at the notch. The target contraction ratio for this inlet was 2.92, and it also reflected the shortest inlet of the series of Mach 5 geometries. The total pressure recovery for this inlet was 0.6686 with an average static throat pressure of approximately 6 psi at slightly less than half an atmosphere. Figure 29 shows the convergence of this solution.

(a) Residuals.

(b) Mass flow rate error.

(c) Surface heating.

(d) Moments about CG.
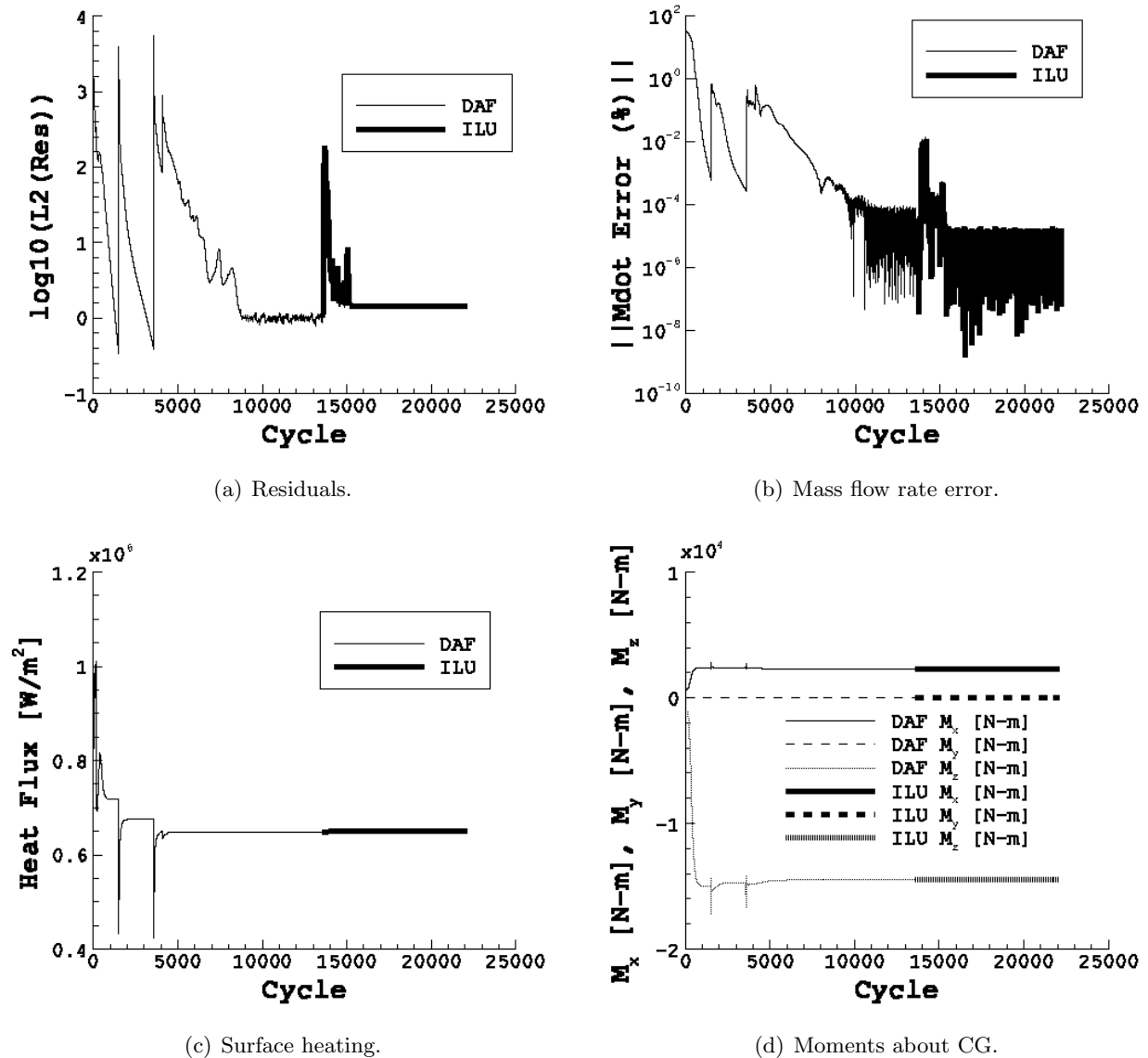
Figure 29. Solution convergence of case 5D-D.

According to the log of the L2 norm residuals, the DAF scheme converged in about 9000 iterations. By comparison to the previous Mach 5 cases, with decreasing length inlets, the time

to convergence had increased steadily. Thus, a trend is that as the contraction ratio decreases for the Mach 5 conditions, the time to convergence increases. The mass flow rate error for the DAF scheme also converged to near zero, though the ILU decreased it by another order of magnitude. Similar to previous computations, the integrated quantities of surface heat transfer and moments remain constant through the converged state of the DAF and ILU schemes. Thus, the solution was considered converged.

The surface properties illustrated in figure 30 show the continuing trend of the weakening shock waves in the inlet from the lower surface pressures, and even smaller y+ values. The smaller y+ values indicate that boundary layer gradients were not as significant. Equally, there was a core from the isolator exit that was not impeded by a flow structure, but the core Mach number was increasing by comparison to previous computations. Another trend is that as the contraction ratio decreases, the internal core Mach number is increasing.
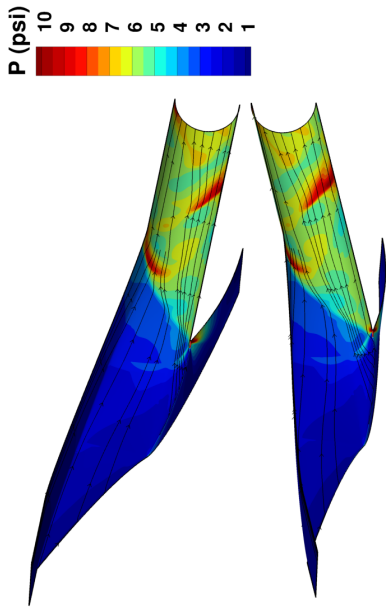
(a) Surface pressure.
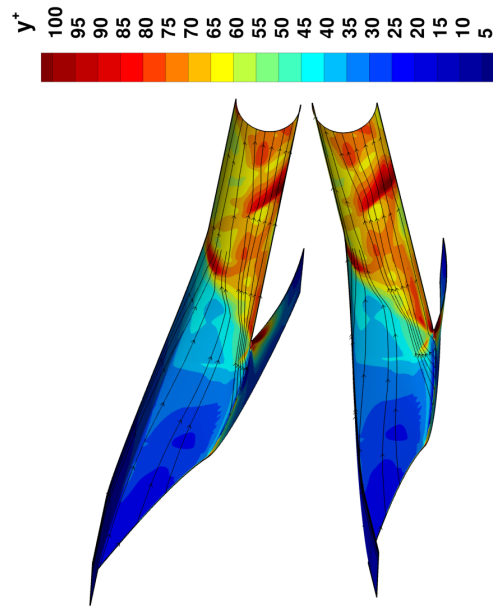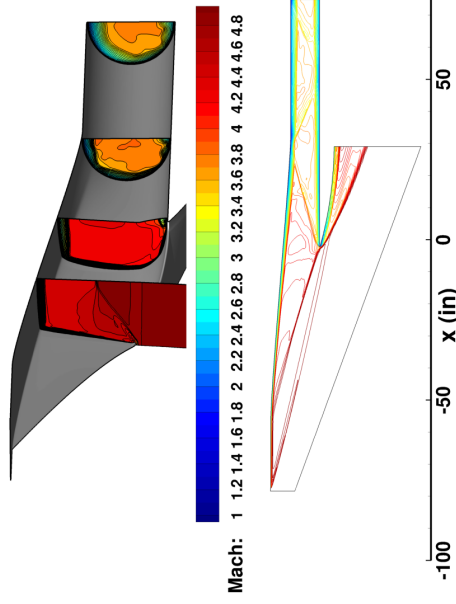
(b) Mach number.
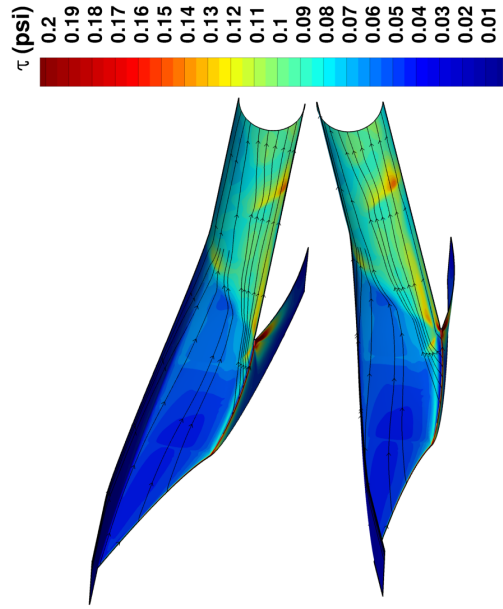
(c) Surface y^+.

(d) Total surface shear.

Figure 30. Surface properties of the case 5D-D.

Investigating deeper into the shock structure of the flow field, shown in figure 31, the shock weakness is illustrated easily by the reflection in the isolator that ends at the top of the inlet. Not only are the reflections now fewer, but the strength of the shock is so diminished it can barely be detected.
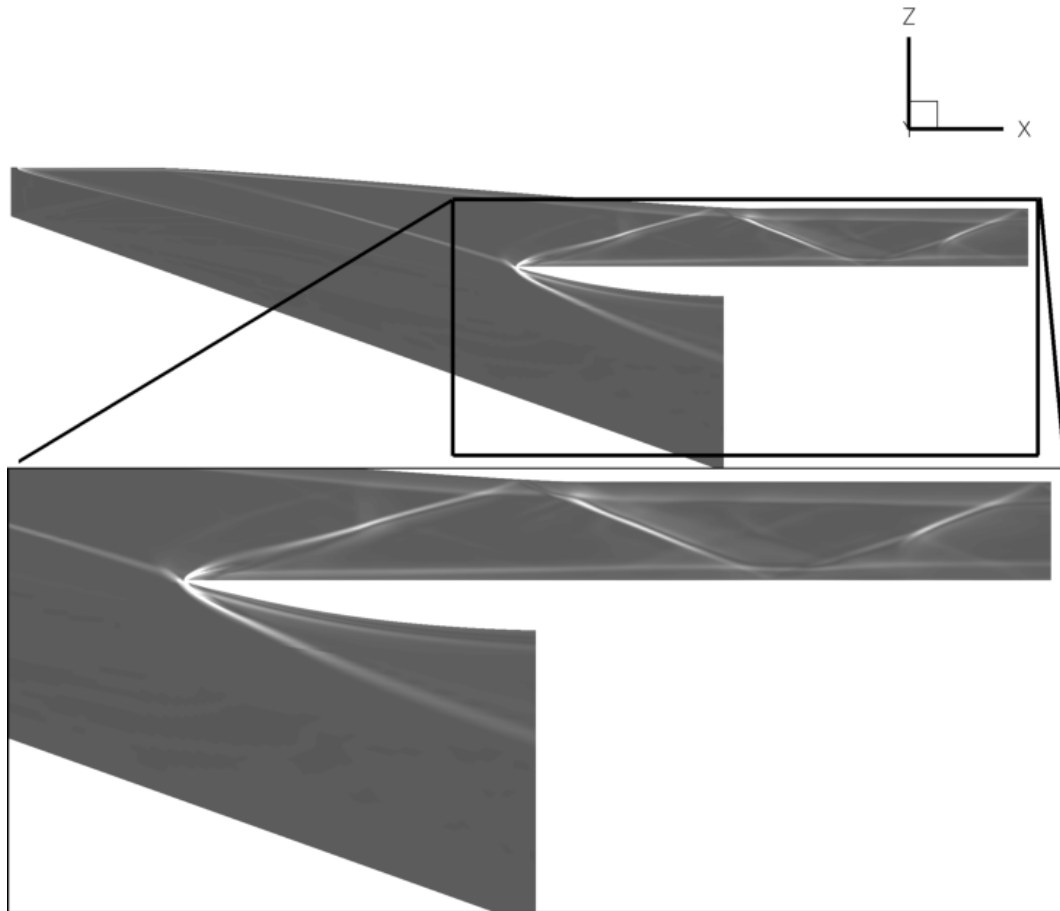
Figure 31. Numerical Schlieren of the symmetry plane of case 5D-D.

In each case the numerical Schlieren images used the same level of contour levels to detect the density gradient. As can be seen in comparison to the cases 5A-D in figure 14 and 5C-D in figure 25, the shock waves become increasingly weaker as the contraction ratio decreases. As the contraction ratio decreases, the compression decreases and the Mach number increases inside the inlet. Additionally, the inlets measured from the leading edge lip to the cowl are shorter. Counter to expected trends, as the shock angles approach a normal shock, the pressure drops and fewer shock reflections occur.

5.8   Case 5D-OD

Similar to the off-design case 5C-OD, this off-design computation for the 5D case did remain started and had a total pressure recovery of 0.8269. Figure 32 shows the convergence data for this computation. By comparison to the off-design flow solution for case 5C, the 5D solution converged

more like previous computations for the on-design conditions. The log of the L2 norm residuals shows convergence at a much lower number of iterations, but the DAF converged to a level that was only three orders of magnitude. The ILU converged the residuals to four orders of magnitude, indicating that the residuals reached a converged state. The mass flow rate error shows similar trends, as do the integrated quantities for each of the solution schemes.
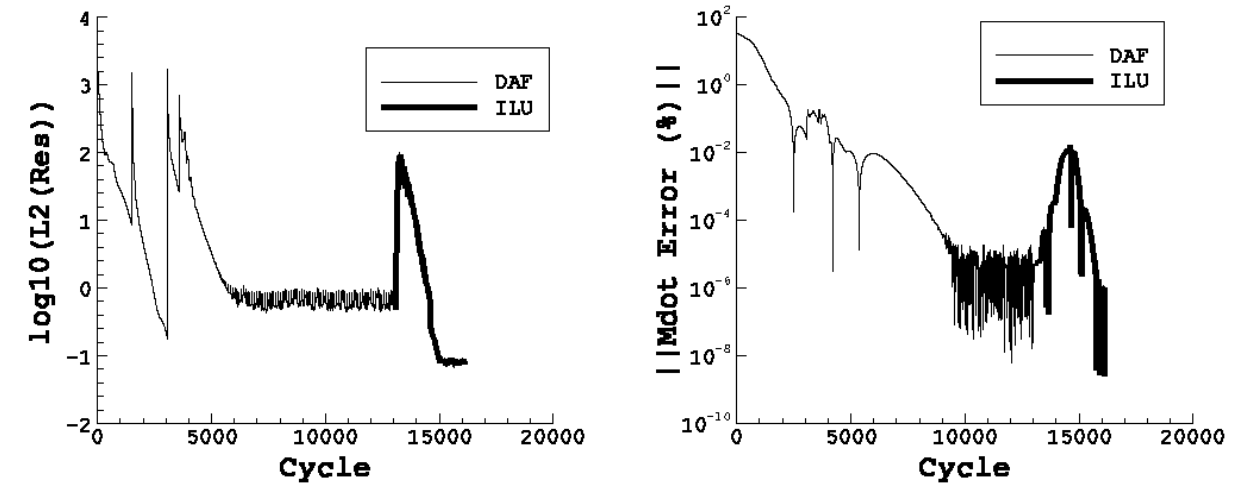
(a) Residuals.

(b) Mass flow rate error.
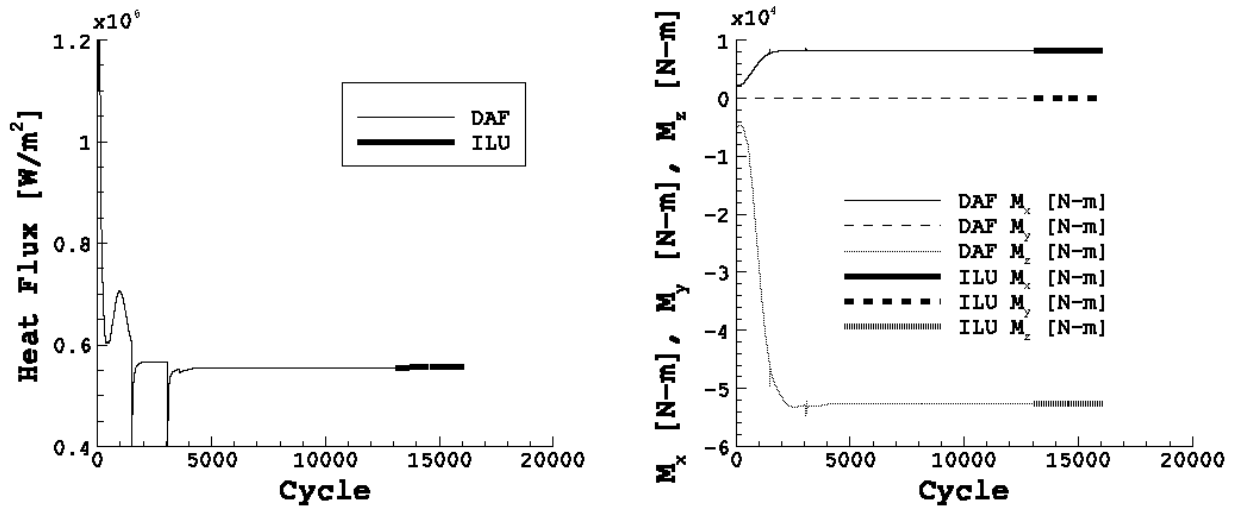
(c) Surface heating.

(d) Moments about CG.

Figure 32. Solution convergence of case 5D-OD.

The surface properties shown in figure 33 illustrate that the number of internal shock reflections was lower than the off-design case of 5C. Also the pressure was lower, the y+ value was lower, and the flow was completely attached as indicated by all positive surface shear. Being the shortest inlet though, the shocks were also weaker than the 5C off-design, a continuing trend in the computations.
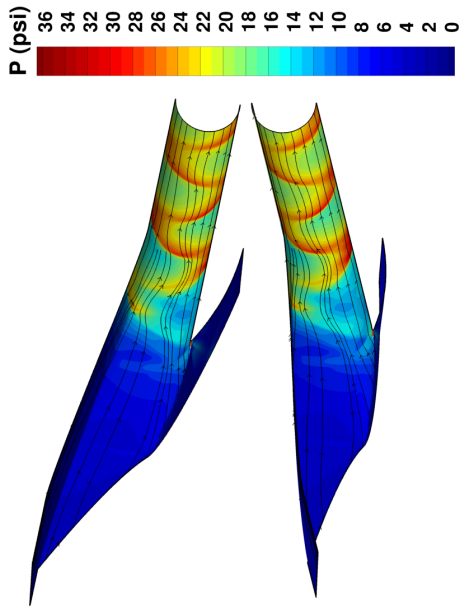
(a) Surface pressure.
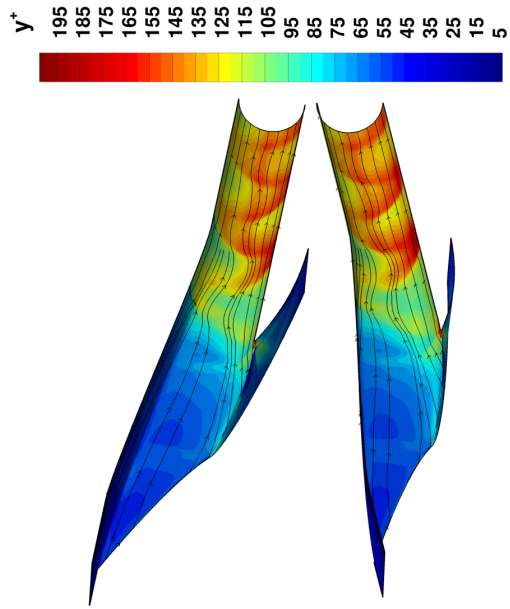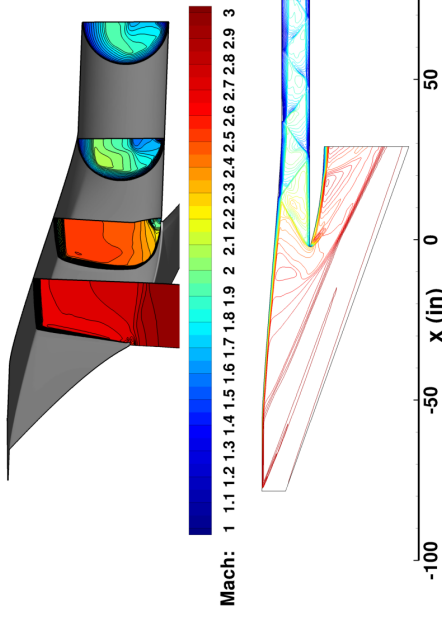
(b) Mach number.
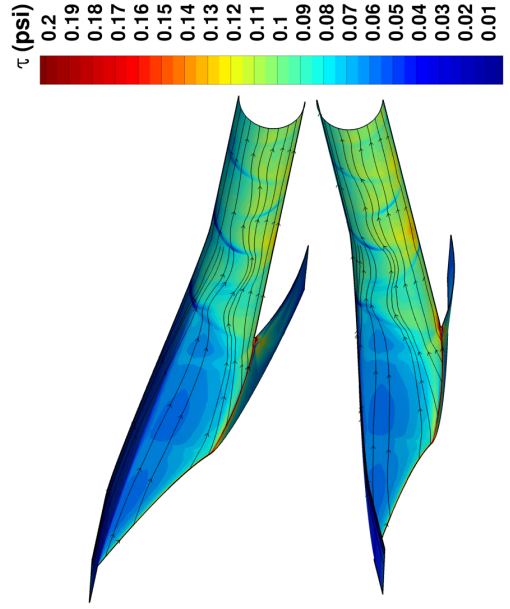
(c) Surface y^+.

(d) Total surface shear.

Figure 33. Surface properties of case 5D-OD.

According to the centerline numerical Schlieren image in figure 34, the number of shock reflections has indeed dropped by one, and the strength of the shock system was weaker. The boundary layer was not processed by as many shockwaves so its thickness was consistent through the inlet. Generally, the flow was well established and remained in a started condition.
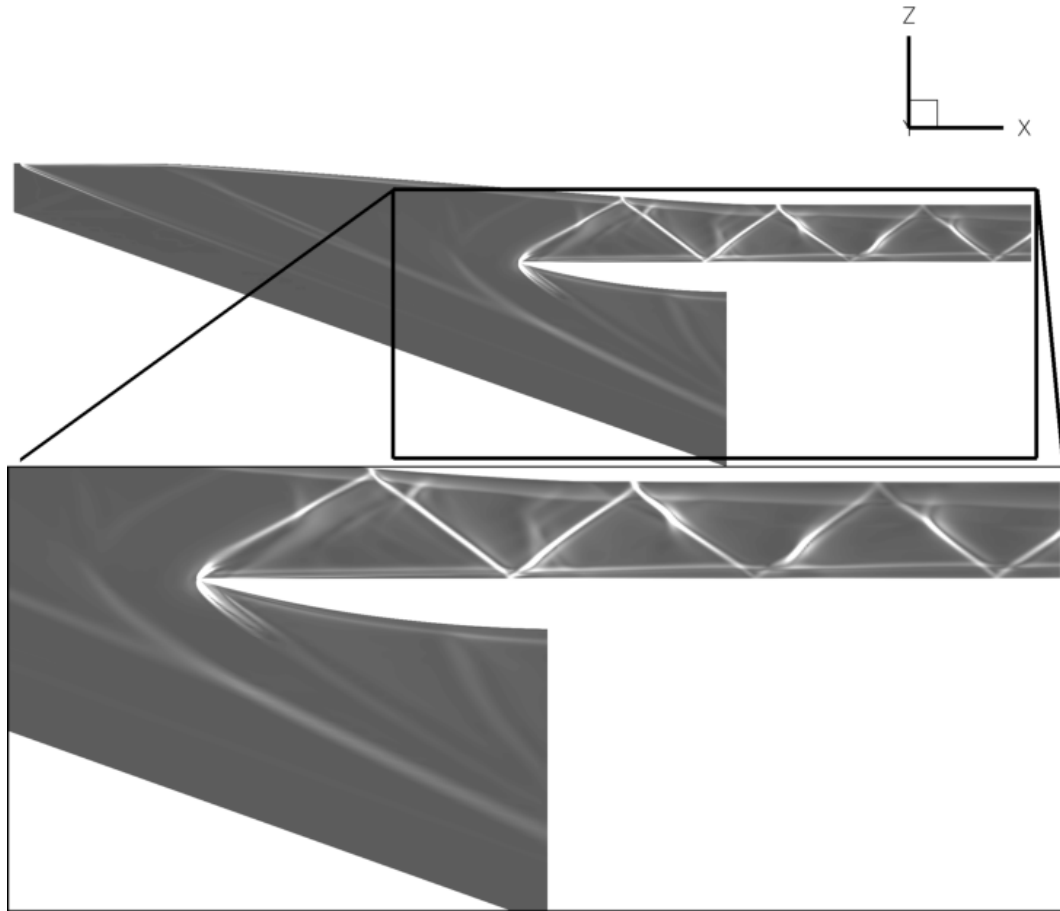
Figure 34. Numerical Schlieren of symmetry plane of case 5D-OD.

5.9   Summary of Mach 5 Solutions

The complete set of the Mach 5 cases was shown to identify trends in the data. The Mach 4 cases, were not covered in the results section because the same trends were seen as in the Mach 5 cases. However, unlike the 5C-OD case that remained "started," the 4C-OD case experienced an unstart condition. Thus only five "started" solutions were obtained from the Mach 4 cases. The additional data that may be useful for Mach 5 cases is the tabulated total pressure recovery for the computed inlets, as shown in table 4.

There are a variety of trends that can be gleaned from the Mach 5 cases. First, and foremost, as the geometric contraction ratio decreased, the shock strength decreased. This is verified by the shallow nature of the shock reflections and the intensity of the density gradients identified by the numerical Schlieren images. Equally interesting is the increase in the number of iterations to a

Table 4. Total pressure recovery for all computed inlets.

Case ID	M_1	Total Pressure Recovery	Case ID	M_1	Total Pressure Recovery
5A-D	5	0.6694	4A-D	4	0.7117
5B-D	5	0.6786	4B-D	4	0.7478
5C-D	5	0.6679	4C-D	4	0.7389
5D-D	5	0.6686	4D-D	4	0.7354
5C-OD	3	0.8276	4C-OD	3	—-
5D-OD	3	0.8269	4D-OD	3	0.8401

converged solution for the DAF scheme with weakening shock waves. Since the factorization error is more significant in the DAF scheme, weaker shocks are not easily resolved, which may require significantly more time to converge a solution. Finally, as the shock waves decrease in strength, the surface pressures decrease as well as the y+ values. This is consistent with shortening the inlet for the reduced contraction ratios because the amount of compression is being decreased.

6 Inlet Performance

Using the "vtls" post processor provided by the 3DHItS process, a variety of plotted data was generated. The massflow3d [28] software was used to generate one-dimensional representations of streamwise data from three-dimensionally [29] sliced data for comparisons among inlet cases. The consistent geometric location for all these computations was the throat or inlet exit. For this reason, all data has been shifted in axial location so that the inlet exit is at an X-ordinate value of zero, and all data is plotted with respect to the length of the inlet from notch to isolator exit. Since the inlets are not the same length, the beginning of the data is at different locations.

With 11 solutions taken to convergence, many of the plots were too busy to show all the data for one performance metric. Thus, two plots were used, where one has all of the Mach 5 cases and another has all the Mach 4 cases. Within each plot, solid lines identify the on-design Mach number cases and dashed lines represent the off-design Mach numbers. Because of the change in line patterns, color is used to differentiate the different contraction ratios.

6.1 Mass Flow Performance Data

The first plot in figure 35 is the cross-sectional area as a function of length, showing that to get the same total contraction ratio for two different on-design Mach numbers, as the Mach number decreases, the internal contraction ratio increases.

One-dimensional static pressure in the axial direction is shown in figure 36. Included on these plots with the gradient symbol is the design throat pressure of the inlet. The inlets for this study were designed without viscous effects factored into the shape. As a result, the design pressures are slightly lower than the computed values because the area of the inlet compressing the fluid is slightly less, thereby increasing the pressure. So the trend within the data is consistent with the design of the inlets.

The axial Mach number variation is shown in figure 37. With the inviscid design of the inlets, the Mach number will conversely be lower than the design. Hence, the trend from the different

(a) Mach 5 cases.

(b) Mach 4 cases.
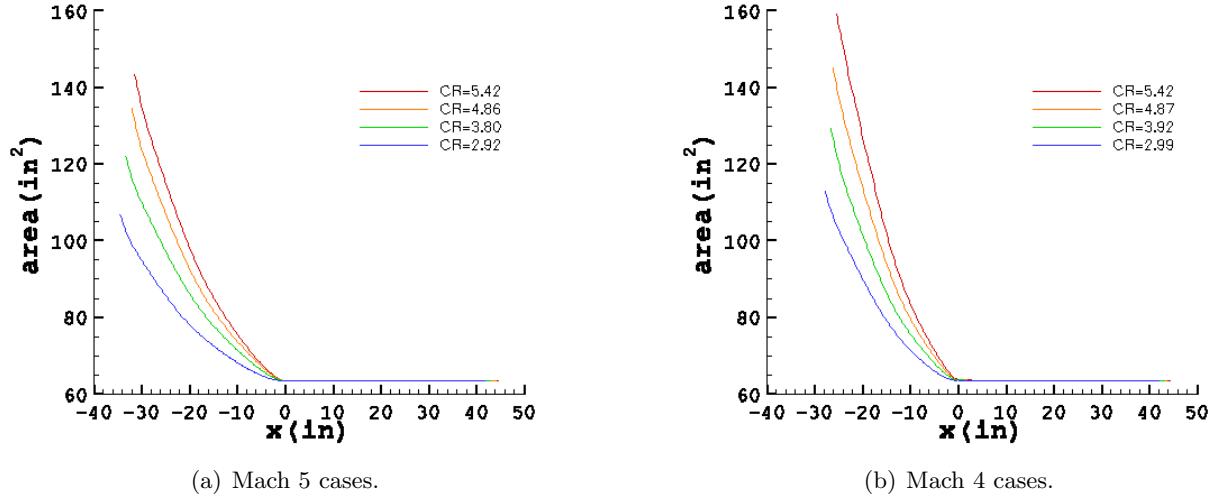
Figure 35. Area as a function of inlet length for all contraction ratios.

(a) Mach 5 cases.

(b) Mach 4 cases.
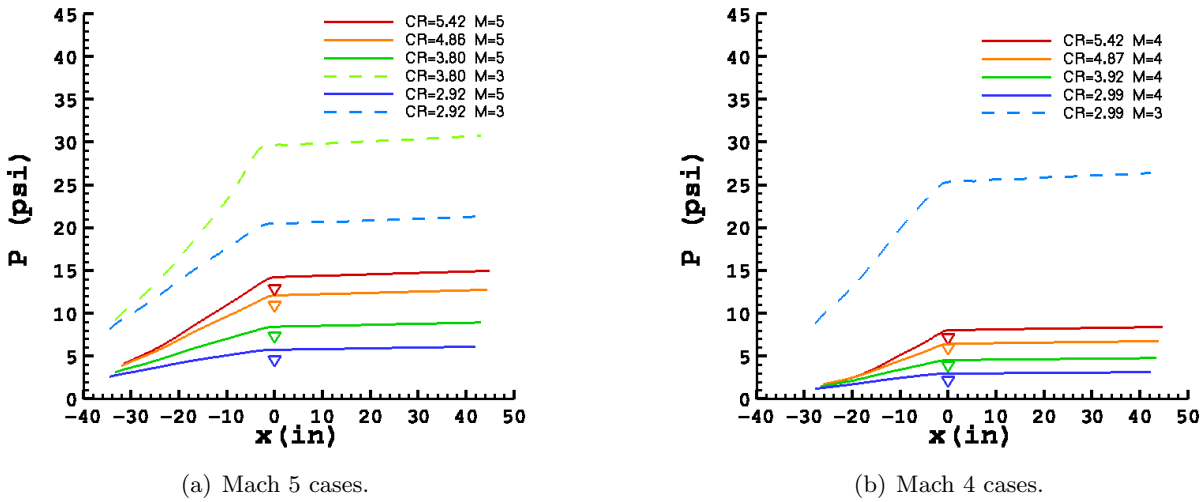
Figure 36. Static pressure as a function of inlet length for all contraction ratios.

design parameters to the CFD would suggest a lower Mach number, and this is reflected in the plots. At the inlet exit are gradient (∇) symbols representing the design Mach numbers for the inlets. These are higher because of the inviscid design methodology used and are, therefore, consistent with the computed results.

The integrated one-dimensional mass flow properties extracted for each case and tabulated, are shown in tables 5 and 6 at the notch for $M_\infty=5$ and $M_\infty=4$, respectively. The upper segment of values represents the on-design Mach numbers, and the lower set are for the off-design Mach 3 case, for the free-stream Mach 5 and 4 inlet designs, respectively. The values that are italicized were for inlets that experienced unstart, and were obtained by running VULCAN with a different

51

(a) Mach 5 cases.　　　　　　　　　　　　(b) Mach 4 cases.
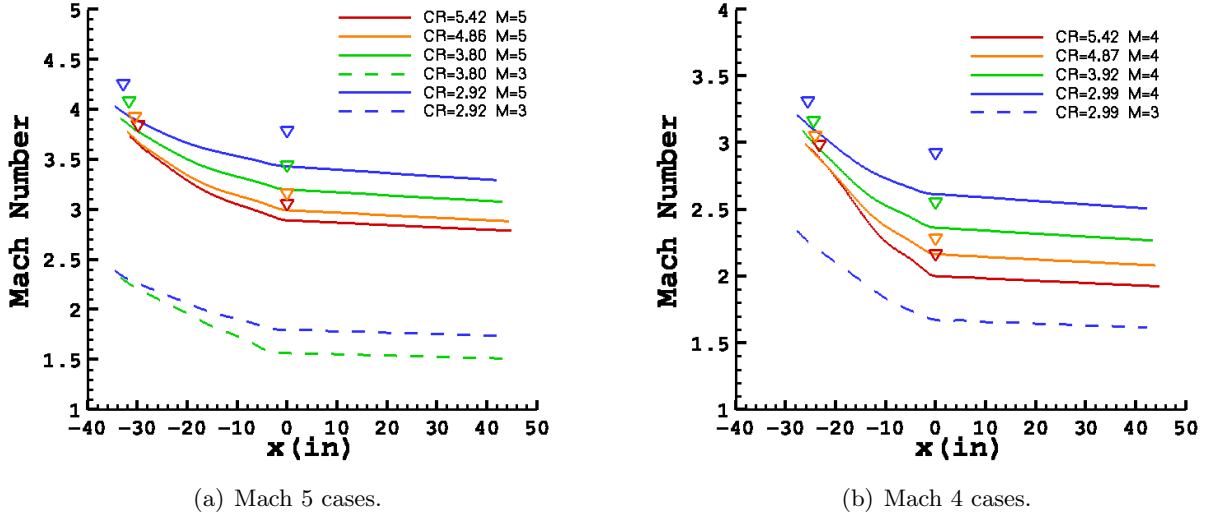
Figure 37. Axial Mach number as a function of inlet length for all contraction ratios.

boundary condition beyond the notch inside the inlet in order to get flow established at the notch for extraction of this data. Since unstart occurs when a normal shock forms because of choked flow at the throat, the region of the grid from the inlet entrance lip to the end of the notch was used for these particular computations. An extrapolated boundary condition was applied at the end of the notch, but well ahead of the throat, to allow the flow to exit this region towards the throat but not to encounter the throat. In this scenario, the conditions at the notch could be determined.

Similarly, tables 7 and 8 list the integrated one-dimensional mass flow properties extracted for each case for $M_\infty=5$ and $M_\infty=4$ at the inlet and isolator exit, respectively. Also listed in tables 7 and 8 are three distortion metrics, which were designed for planar flow fields [28]. They represent the area, momentum, and divergent velocity distortions given by equations 1 through 3, respectively.

$$\eta_{area} = \frac{\int \rho u \, dA}{\rho_{ref} u_{ref} A} \tag{1}$$

$$\eta_{momentum} = \frac{\int \rho u^2 \, dA}{\rho_{ref} u_{ref}^2 A} \tag{2}$$

$$\eta_{div \; vel} = \frac{\int \rho u \left(v^2 + w^2\right) dA}{\left(\rho_{ref} u_{ref}\right) u_{ref}^2 A} \tag{3}$$

52

Table 5. Integrated one-dimensional Mach number at the notch for $M_\infty = 5$.

Case ID	Contraction Ratio	CFD Computed Contraction	Mach Number
5A-D	5.42	5.44	3.7259
5B-D	4.86	4.90	3.7737
5C-D	3.80	3.82	3.9608
5D-D	2.92	2.97	4.0303
5A-OD	5.42	*4.52*	*2.13*
5B-OD	4.86	*4.09*	*2.15*
5C-OD	3.80	3.30	2.3172
5D-OD	2.92	2.60	2.3858

Table 6. Integrated one-dimensional Mach number at the notch for $M_\infty = 4$.

Case ID	Contraction Ratio	CFD Computed Contraction	Mach Number
4A-D	5.42	5.43	2.9670
4B-D	4.87	4.88	2.9926
4C-D	3.92	3.93	3.0868
4D-D	2.99	3.01	3.2069
4A-OD	5.42	*5.18*	*2.03*
4B-OD	4.87	*4.67*	*2.09*
4C-OD	3.92	*3.76*	*2.20*
4D-OD	2.99	2.92	2.3401

Table 7. One-dimensional properties for the inlet exit.

Case ID	M∞	Contraction Ratio	Mach Number	Total Velocity (ft/sec)	Density (lbm/ft³)	Pressure (psi)	Temperature (°R)	Stream Thrust (lbf.)	Area Distort.	Mom. Distort.	div. Vel. Distort.
5A-D	5.0	5.42	2.7902	4704.1016	1.8845e-05	14.9815	1229.7171	10773.5777	0.9785	0.9745	1.0011
5B-D	5.0	4.86	2.8855	4775.0362	1.6709e-05	12.7679	1182.0126	9779.0256	0.9772	0.9731	1.0013
5C-D	5.0	3.80	3.1526	4952.7022	1.1692e-05	8.0020	1058.6865	7244.9274	0.9715	0.9671	1.0004
5D-D	5.0	2.92	3.2960	5035.8630	9.4936e-06	6.1267	998.2584	6034.1271	0.9700	0.9657	1.0004
5C-OD	3.0	3.80	1.5148	2377.7006	4.4975e-05	30.7252	1056.7516	7748.6232	0.9755	0.9693	1.0006
5D-OD	3.0	2.92	1.7395	2618.7825	3.4075e-05	21.3173	967.7135	6663.2162	0.9834	0.9792	1.0004
4A-D	4.0	5.42	1.9254	3291.9390	1.0291e-05	8.4299	1267.0519	3149.2907	0.9678	0.9607	1.0009
4B-D	4.0	4.87	2.0828	3457.8947	8.8055e-06	6.7751	1190.1645	2895.5813	0.9802	0.9755	1.0015
4C-D	4.0	3.92	2.2694	3629.2069	6.7517e-06	4.7984	1099.3315	2382.5651	0.9735	0.9677	1.0003
4D-D	4.0	2.99	2.5099	3827.0036	4.9033e-06	3.1507	993.9578	1871.9386	0.9800	0.9757	1.0005
4D-OD	3.0	2.99	1.6171	2495.1008	4.0073e-05	26.4036	1019.2041	7359.7841	0.9858	0.9819	1.0012

Table 8. One-dimensional properties for the isolator exit.

Case ID	M∞	Contraction Ratio	Mach Number	Total Velocity (ft/sec)	Density (lbm/ft³)	Pressure (psi)	Temperature (°R)	Stream Thrust (lbf.)	Area Distort.	Mom. Distort.	div. Vel. Distort.
5A-D	5.0	5.42	2.7888	4702.5786	1.8852e-05	14.9929	1230.1816	10771.3384	0.9792	0.9752	1.0010
5B-D	5.0	4.86	2.8841	4773.5796	1.6715e-05	12.7773	1182.4619	9777.1208	0.9779	0.9739	1.0012
5C-D	5.0	3.80	3.1508	4951.0301	1.1697e-05	8.0092	1059.2042	7243.2048	0.9717	0.9673	1.0004
5D-D	5.0	2.92	3.2939	5034.0287	9.4980e-06	6.1331	998.8384	6032.5274	0.9689	0.9644	1.0003
5C-OD	3.0	3.80	1.5141	2376.6181	4.4998e-05	30.7433	1056.8255	7746.9968	0.9748	0.9683	1.0006
5D-OD	3.0	2.92	1.7386	2617.6653	3.4089e-05	21.3299	967.8790	6661.5472	0.9836	0.9794	1.0004
4A-D	4.0	5.42	1.9244	3290.4331	1.0296e-05	8.4348	1267.1913	3148.2652	0.9668	0.9594	1.0007
4B-D	4.0	4.87	2.0818	3456.5683	8.8095e-06	6.7794	1190.3971	2894.8608	0.9807	0.9761	1.0013
4C-D	4.0	3.92	2.2683	3627.8412	6.7545e-06	4.8013	1099.5435	2381.8894	0.9739	0.9681	1.0003
4D-D	4.0	2.99	2.5087	3825.7152	4.9053e-06	3.1529	994.2500	1871.5088	0.9795	0.9751	1.0006
4D-OD	3.0	2.99	1.6168	2494.6008	4.0090e-05	26.4132	1019.1422	7358.5722	0.9858	0.9818	1.0015

The data tables have been plotted so that trends could be examined. Figure 38 shows the Mach number as a function of contraction ratio at the throat and exit of the inlet. As the contraction ratio increases, the Mach number decreases, which is indicative of the work being performed on the fluid as it is processed by the inlet. The higher the contraction ratio, the higher the compression of fluid, and the flow decreases in velocity (figure 39).

(a) Throat conditions.

(b) Exit conditions.
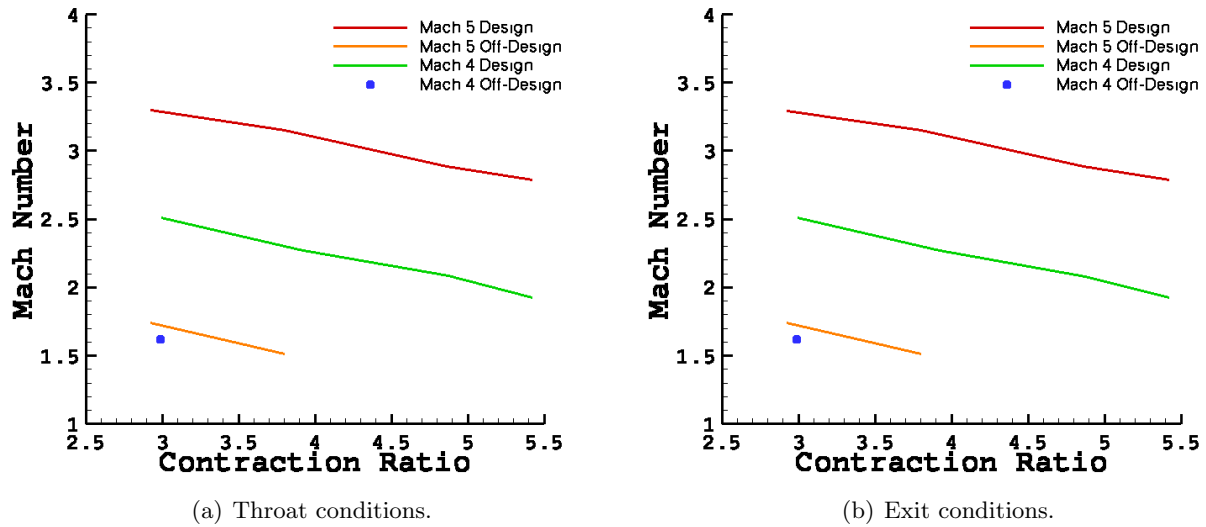
Figure 38. Integrated one-dimensional Mach number as a function of the contraction ratio for all inlets.

(a) Throat conditions.

(b) Exit conditions.
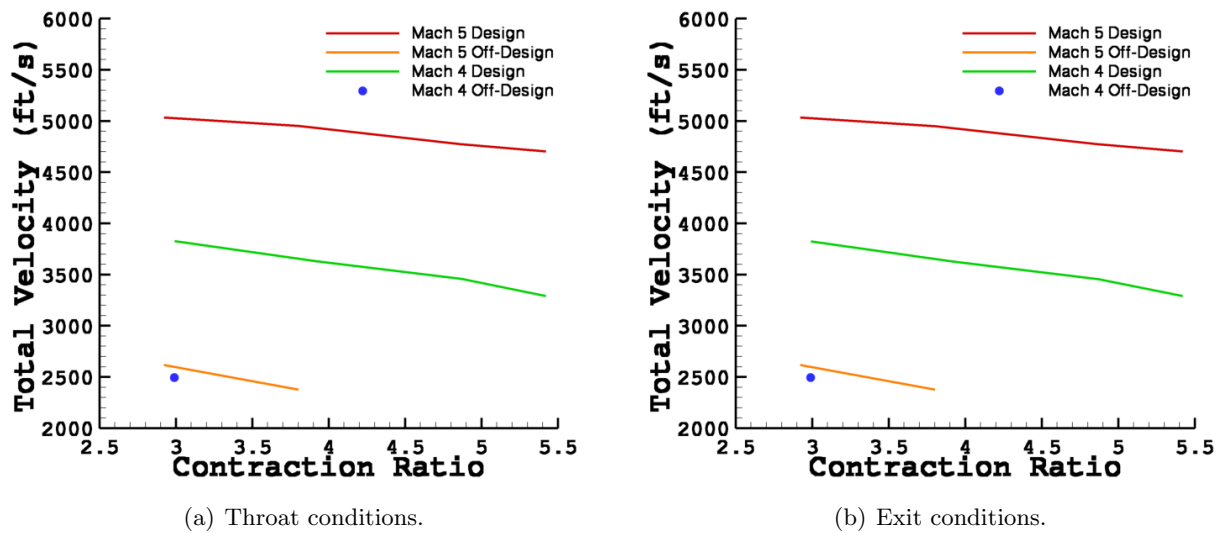
Figure 39. Integrated one-dimensional velocity as a function of the contraction ratio for all inlets.

Equally evident of the work performed on the fluid is the pressure plotted in figure 40. As the contraction ratio increases, the pressure increases because more work is being done on the fluid to compress it.

(a) Throat conditions.

(b) Exit conditions.
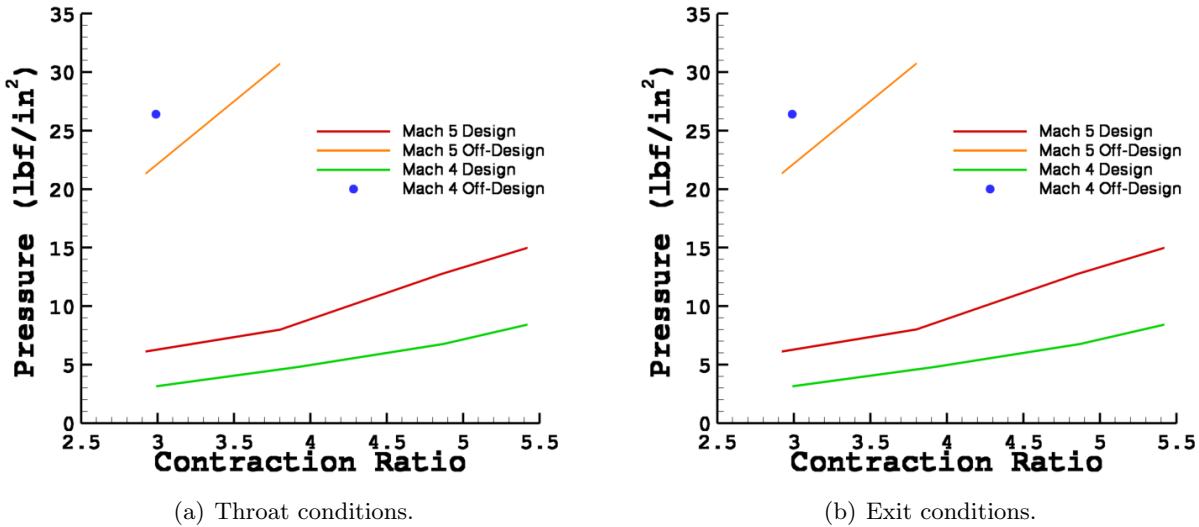
Figure 40. Integrated one-dimensional static pressure as a function of the contraction ratio for all inlets.

While the velocity is not very sensitive to the contraction ratio, the static pressure is. Following the equation of state, the density and temperature reflect the sensitivities, as shown in figures 41 and 42, respectively.

(a) Throat conditions.

(b) Exit conditions.
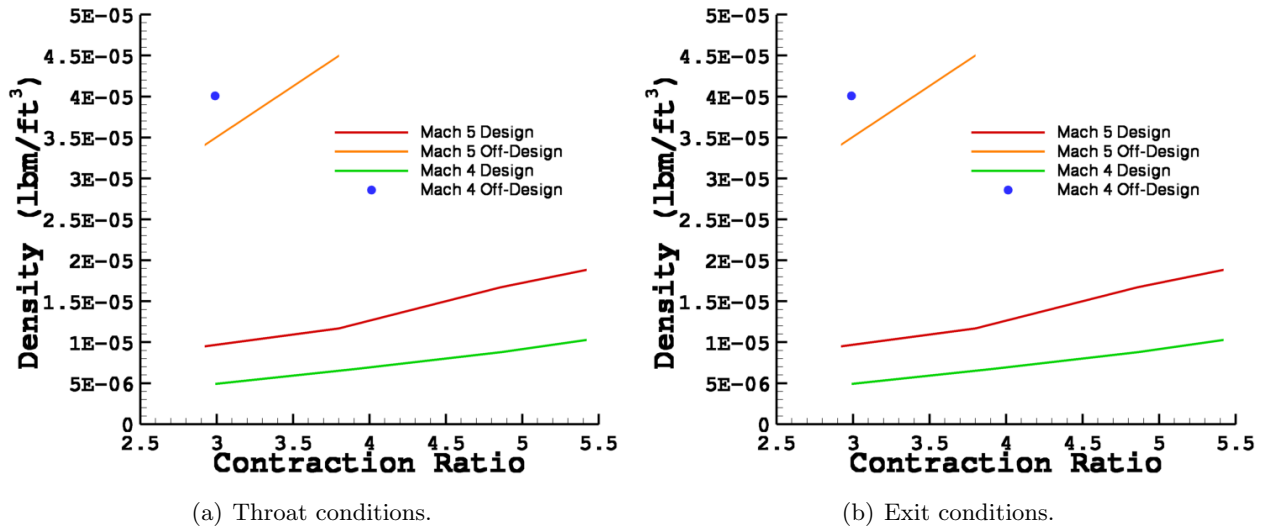
Figure 41. Integrated one-dimensional density as a function of the contraction ratio for all inlets.

(a) Throat conditions.

(b) Exit conditions.
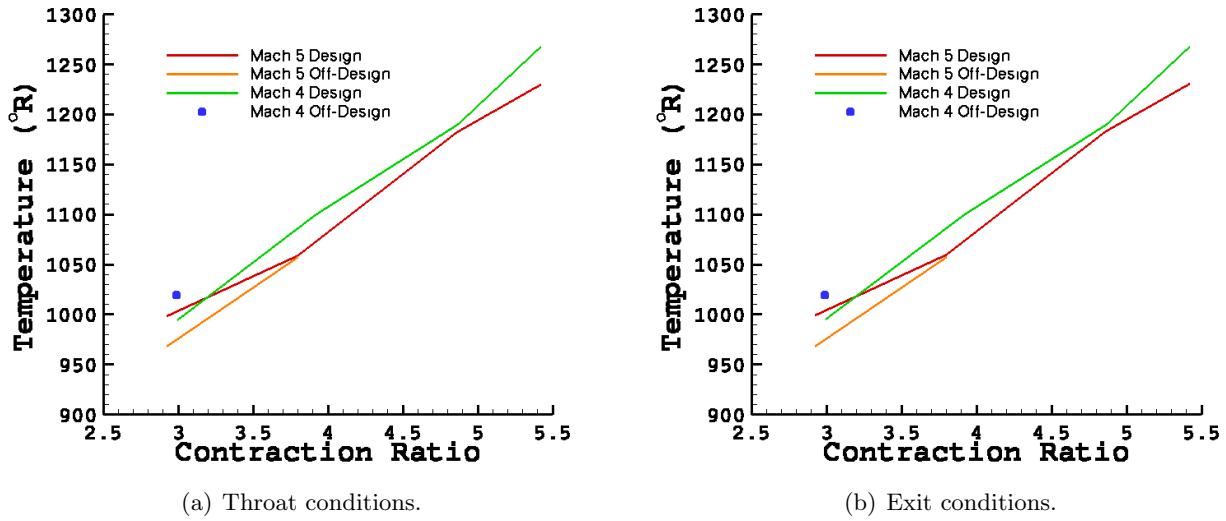
Figure 42. Integrated one-dimensional temperature as a function of the contraction ratio for all inlets.

Another important parameter in tables 7 and 8 is the stream thrust produced by the inlet as shown in figure 43. Prior to entering the combustion chamber, the stream thrust of the inlet is steadily decreasing as the fluid continues to be processed by the inlet, an indication of the drag produced by the inlet.

(a) Throat conditions.

(b) Exit conditions.
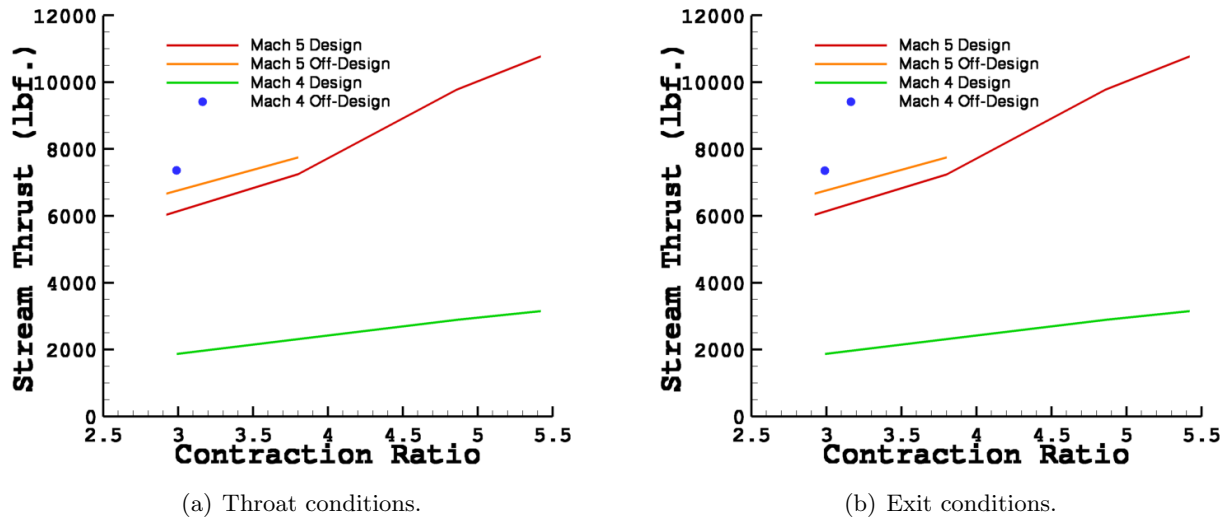
Figure 43. Integrated one-dimensional stream thrust as a function of the contraction ratio for all inlets.

Finally, figures 44, 45, and 46 show the distortion measures of area, momentum, and divergent velocity, respectively. The goal of the inlet is to produce as minimum losses as possible to the combustor from the isolator but when the inlet compresses the air, it is possible to distort the boundary layer through nonuniformities as well as through strong oblique shock waves within the inlet. These three measures are an evaluation of how distorted the fluid is as it is processed by the inlet towards the exit of the isolator, representing the conserved one-dimensional quantity divided by the same quantity computed with reference inflow values.

(a) Throat conditions.

(b) Exit conditions.
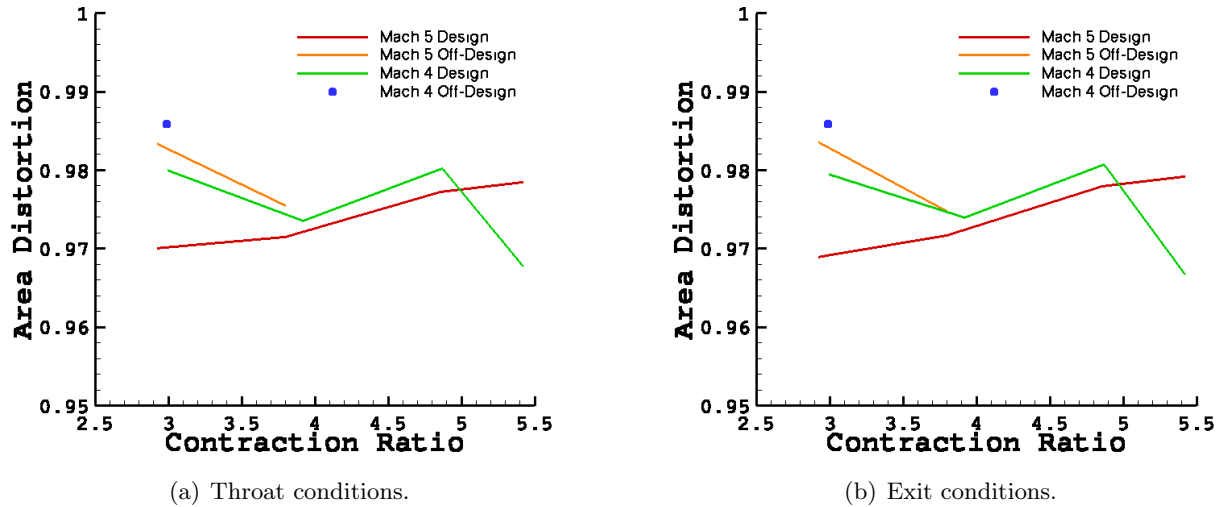
Figure 44. Integrated one-dimensional area distortion as a function of the contraction ratio for all inlets.

(a) Throat conditions.

(b) Exit conditions.
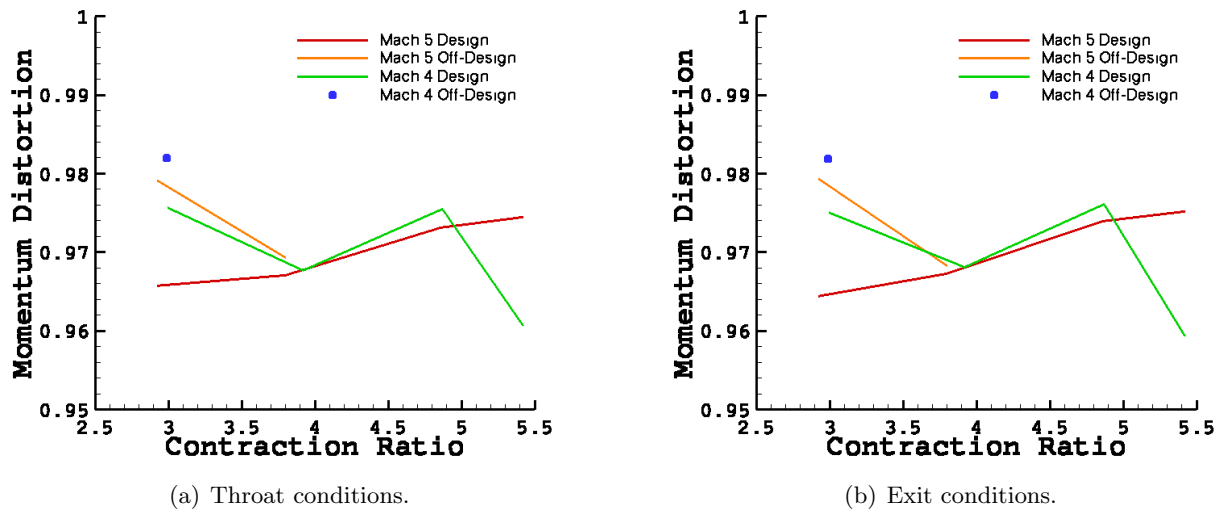
Figure 45. Integrated one-dimensional momentum distortion as a function of the contraction ratio for all inlets.

(a) Throat conditions. (b) Exit conditions.
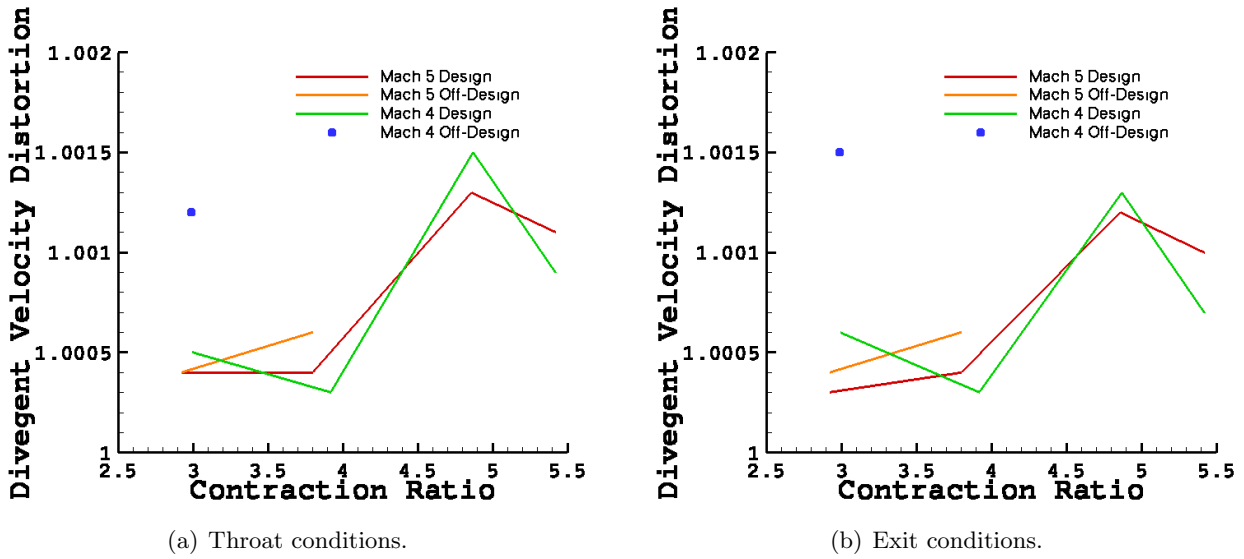
Figure 46. Integrated one-dimensional divergent velocity distortion as a function of the contraction ratio for all inlets.

Although the trends are similar, the free-stream conditions for these cases are not consistent. The Mach 3 and 5 solutions were for a high dynamic pressure condition while the Mach 4 cases were for a low dynamic pressure condition. The differences in free-stream conditions originated from the availability of nozzles for the 8-ft HTT facility. This study is not based on a specific trajectory or flight condition but is to determine what is possible with available wind tunnel set up. Thus, any relevance between the Mach 3 and 5 data to the Mach 4 data is simply coincidental and does not serve as an envelope for designing inlets or conditions. Deviation from the curves should be avoided.

6.2 Surface Performance Data

Analysis of the surface performance properties of these inlets began with the perimeter of the inlets as a function of axial location as shown in figure 47. Similar to the area function along the axial locations of the inlet, the higher Mach number design inlets had smaller perimeter lengths.

(a) Mach 5 cases.

(b) Mach 4 cases.
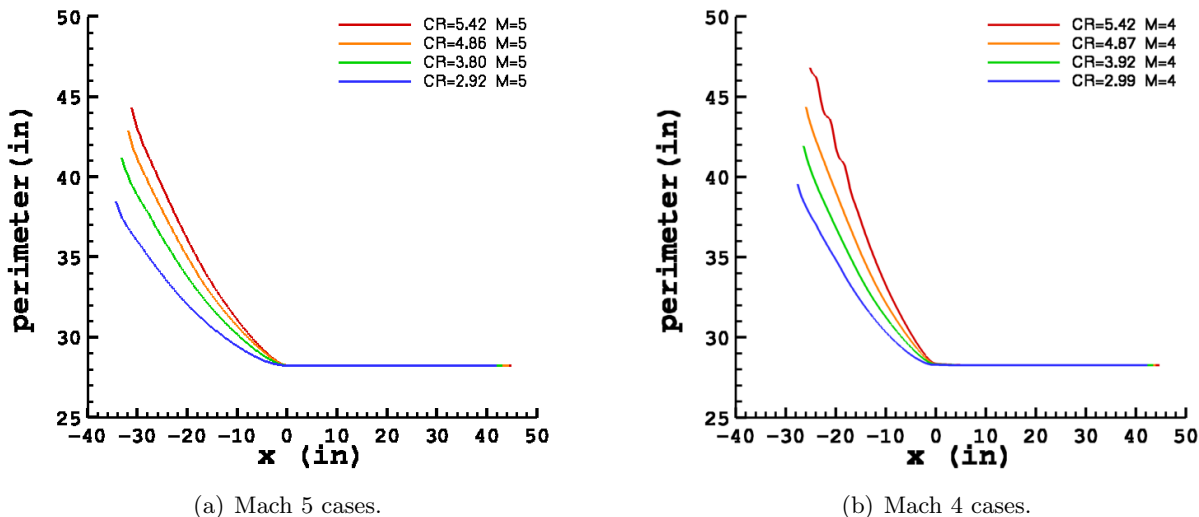
Figure 47. Perimeter as a function of inlet length for all contraction ratios.

The total surface shear stress combined with the sign of the streamwise component was a measure of how well the flow field was attached to the wall of the inlet, such that for negative shear, a region of separation would have been indicated. Thus, the minimum surface shear stress is shown in figure 48, while the average surface shear stress is shown in figure 49. The minimum surface shear stress is the minimum value of any of the three surface shear stress components in a cross-section whereas the average is the average of all surface shear stress values for the cross-section, assuming that the grid is nearly orthogonal to the axial axis of the inlet. For the grids generated, this is an accurate assessment. The minimum surface shear stress is considered because it provides an indicator of where separation may begin to occur. The average surface shear stress is shown because it aids in determining to what degree the minimum is affecting the total surface shear stress. These surface shear stress quantities are used in the HAPB to determine performance of the inlet and whether or not flow conditions are favorable for further considering of a particular inlet design.

Though the minimum surface shear stress for the Mach 5 cases did get low in three different locations for the off-design Mach number computations, they did not separate and were always positive. However, for the Mach 4 cases, this was not true. The highest compression of the flow for a geometric contraction ratio of 5.42 at Mach 4 did experience separation ahead of the throat of the inlet and also did occur for the off-design case that ran without an unstart condition. In fact the surface shear stress for the off-design case indicated this inlet performed at less than desirable conditions from the various changes in minimum surface shear stress. This was also seen in the average surface shear stress plots, though the Mach 5 cases did not show similar effects and, in fact, suggested reasonable performance characteristics.
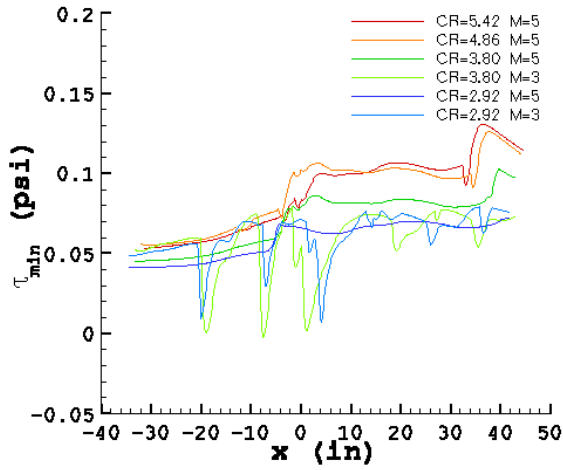
(a) Mach 5 design inlets.
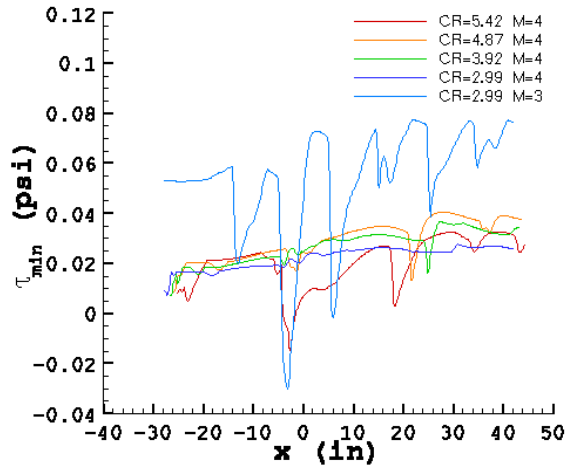
(b) Mach 4 design inlets.

Figure 48. Minimum surface shear stress as a function of inlet length for all contraction ratios.

(a) Mach 5 design inlets.

(b) Mach 4 design inlets.

Figure 49. Average surface shear stress as a function of inlet length for all contraction ratios.

The tabulated data for the one-dimensional surface properties of the inlet at the inlet and isolator exits are shown in tables 9 and 10, respectively.

Table 9. Surface perimeter properties for the inlet exit.

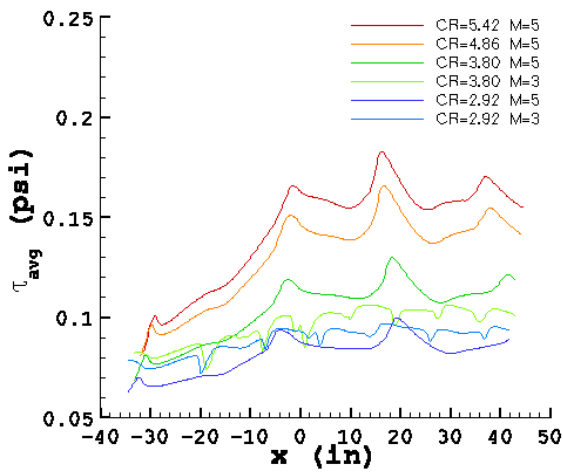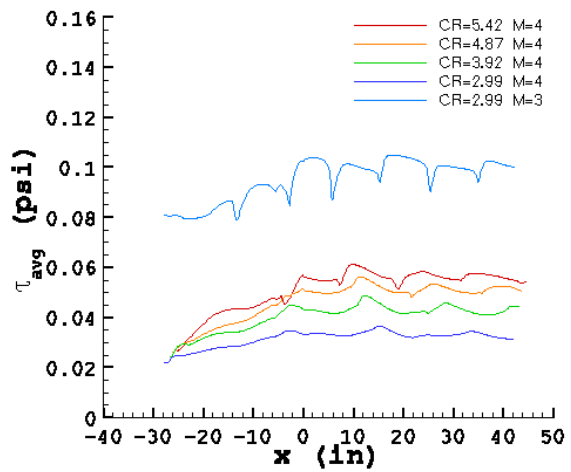| Case ID	M_∞	Contraction Ratio	Minimum p (lb/in^2)	Average p (lb/in^2)	Maximum p (lb/in^2)	Minimum τ (lb/in^2)	Average τ (lb/in^2)	Maximum τ (lb/in^2)
5A-D	5.0	5.42	11.6787	14.3467	17.6922	0.0821	0.1637	0.2098
5B-D	5.0	4.86	10.4111	12.1472	15.5747	0.1010	0.1471	0.1833
5C-D	5.0	3.80	6.5133	7.4795	8.9296	0.0717	0.1064	0.1307
5D-D	5.0	2.92	5.0571	5.7334	7.7633	0.0663	0.0879	0.1066
5C-OD	3.0	3.80	18.1339	30.9918	36.3813	0.0527	0.0961	0.1489
5D-OD	3.0	2.92	14.0247	19.3907	26.6152	0.0715	0.0934	0.1294
4A-D	4.0	5.42	6.4064	8.1313	9.2970	0.0067	0.0568	0.0777
4B-D	4.0	4.87	5.2226	6.3664	7.3555	0.0246	0.0513	0.0671
4C-D	4.0	3.92	3.7109	4.4683	5.2923	0.0247	0.0434	0.0542
4D-D	4.0	2.99	2.4993	2.9069	3.5489	0.0212	0.0333	0.0423
4D-OD	3.0	2.99	16.8829	25.9557	40.2701	0.0431	0.1024	0.1531

Table 10. Surface perimeter properties for the isolator exit.

Case ID	M_∞	Contraction Ratio	Minimum p (lb/in^2)	Average p (lb/in^2)	Maximum p (lb/in^2)	Minimum τ (lb/in^2)	Average τ (lb/in^2)	Maximum τ (lb/in^2)
5A-D	5.0	5.42	12.8685	14.3350	16.1210	0.1139	0.1547	0.1814
5B-D	5.0	4.86	11.2694	12.5044	14.0269	0.1120	0.1415	0.1628
5C-D	5.0	3.80	7.3784	8.7008	9.8331	0.0764	0.1097	0.1303
5D-D	5.0	2.92	5.6596	6.8077	10.0766	0.0721	0.0893	0.1022
5C-OD	3.0	3.80	31.2168	32.4039	35.2965	0.0733	0.1009	0.1177
5D-OD	3.0	2.92	18.5627	21.2292	25.8255	0.0758	0.0937	0.1096
4A-D	4.0	5.42	7.6116	9.2944	11.3015	0.0279	0.0546	0.0637
4B-D	4.0	4.87	6.2976	6.6014	6.9155	0.0376	0.0506	0.0637
4C-D	4.0	3.92	4.4771	5.1872	6.6984	0.0345	0.0443	0.0585
4D-D	4.0	2.99	2.8328	3.0429	3.1824	0.0259	0.0315	0.0362
4D-OD	3.0	2.99	23.8947	26.2777	29.3705	0.0762	0.0999	0.1272

The data collected within tables 9 and 10 are plotted in the following figures to graphically identify trends in the data. Although the tables show minimum, average, and maximum values for the pressure and surface shear stress, the values are used to show limits of these variables. For this reason, the limits are not specifically plotted but rather used for range bars on the plots to illustrate ranges of these two variables. The pressure is then shown in figure 50, and the surface shear stress is shown in figure 51.
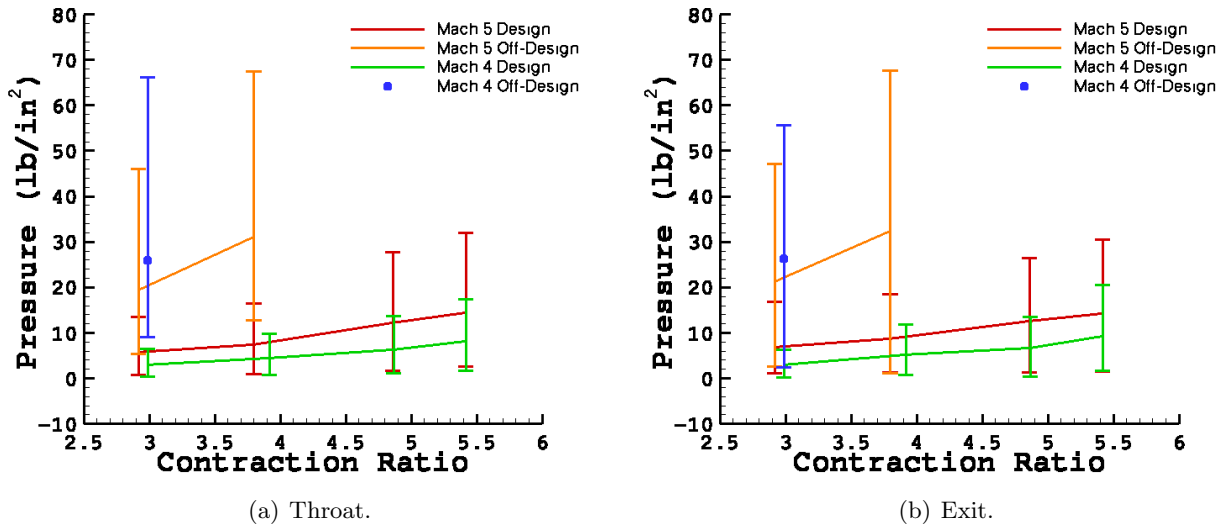

(a) Throat.

(b) Exit.

Figure 50. Perimeter pressure as a function of contraction ratio for all inlets.
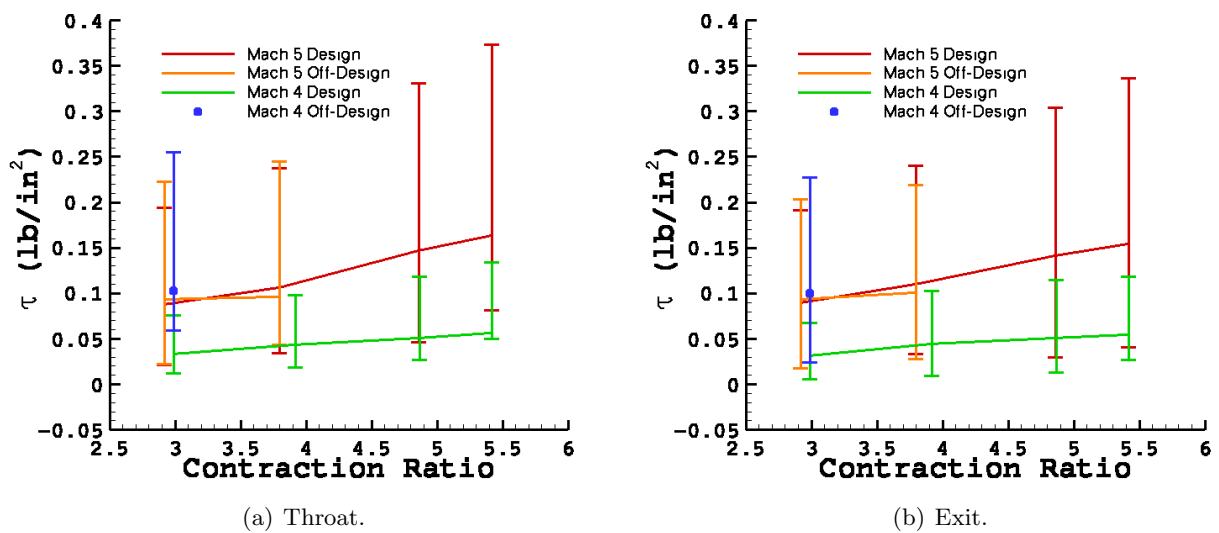

(a) Throat.

(b) Exit.

Figure 51. Perimeter surface shear stress as a function of contraction ratio for all inlets.

63

Similar to the trends noted in the one-dimensional property tables and plots, the trends in this data are only valid for the Mach 5 and Mach 3 cases because these represent high dynamic pressure condition nozzles for the 8-ft HTT facility. The Mach 4 cases were for a low dynamic pressure condition, so attempting to draw conclusions from possible operational envelopes from the data is not recommended. The reason for the Mach 4 computational results is that these computations are for existing 8-ft HTT nozzles. Thus, the Mach 4 computations represent a feasible facility reference condition.

6.3 Boundary Layer Properties

The boundary layer properties of the various inlets that ran at a started condition were collected in a variety of plots and tabulated data. Due to the significant extent of this data, and the importance of it, the presentation of the data will deviate slightly from previous collected information. First, the plots of aerodynamic and aerothermodynamic properties that are affected by the boundary layer will be shown, followed by tabulated data and plots of that data. The last set of data will be plots of what the boundary layer edge looks like within the inlet followed by boundary layer area ratio information and overall inviscid core data so that the inlet performance can be easily compared among the variety of geometric changes made to the inlets for accommodating the ranging contraction ratios.

Unlike previous variables plotted for axial location, the boundary layer properties are plotted from either the lip of the inlet to the isolator exit (1) for the body centerline on top of the inlet, or from the notch to the isolator exit for the cowl centerline on the bottom of the inlet, both of which are on the symmetry plane of the inlet. The top of the inlet is considered the body centerline because the top is typically where the engine is attached to the flight vehicle. The bottom of the inlet is typically called the cowl side because this is the side opposing the body where the cowl of the inlet closes off the inlet so that the flow is encompassed by walls of the inlet beyond the notch in the streamwise axial direction. The centerline pressure is shown in figure 52 for both top and bottom of the inlet.

Based on figure 52, the pressure at the lip for the top of the inlet is high due to a zero angle of attack ($\alpha = 0$) producing stagnated flow at the lip. This was not the case for the notch because the incoming flow to the lower side of the inlet was already turned by the Busemann compression field of the forward portion of the inlet. Characteristically, the pressure begins to vary at about 15 inches ahead of the inlet exit on both the bottom and top, which is an indication of the shock waves produced by the closing of the inlet entrance to solid walls on all sides.

The surface heat transfer (fig. 53) shows some different trends worth noting. The lower design Mach number cases have lower heat transfer in general, but for both the Mach 5 and Mach 4 design cases, the cowl side of the inlet had generally higher surface heat transfer than the top of the inlet. This may be attributed to a few characteristics. First, the cowl side of the inlet also had the thinnest boundary layer, so the thermal gradient was stronger leading to higher heating. Second, the elevated heating may be due to the extra processing by internal shock waves of the flow field of the closed section of the inlet that was past the axial location of the notch where the cowl side incoming shock wave was first reflected. This additional processing of the fluid would raise the energy in the boundary layer, causing the thermal gradient near the wall to be steeper. Hence, higher overall heating occurred along the cowl side of the centerline by comparison to the body centerline.
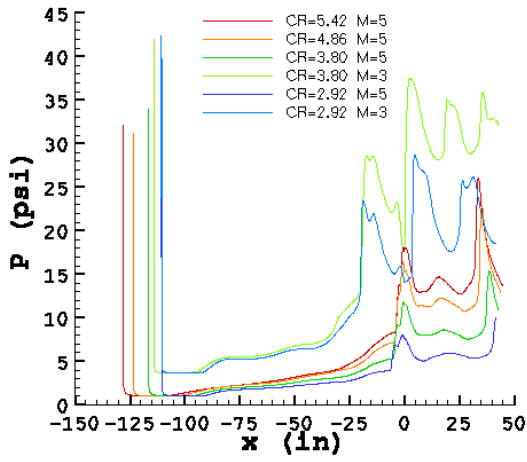
(a) Mach 5 inlet design body centerline cases.
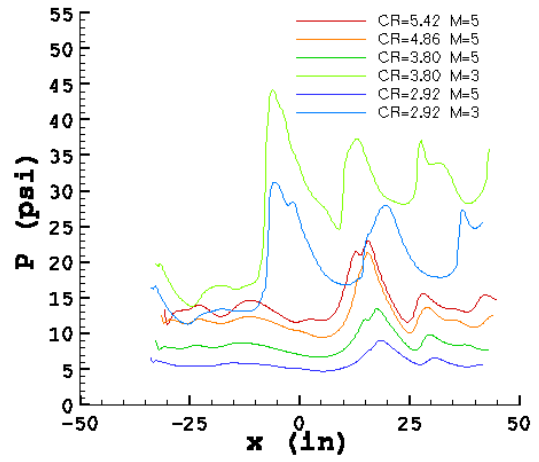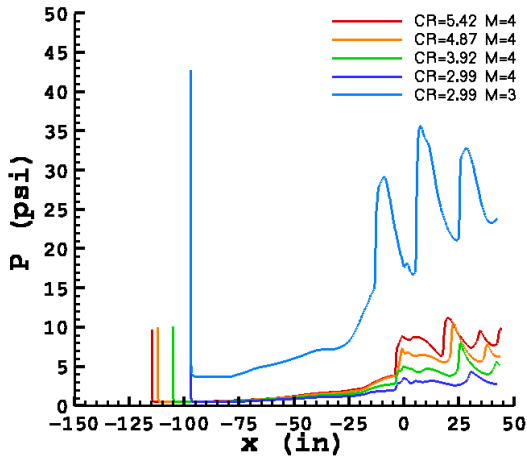
(b) Mach 5 inlet design cowl centerline cases.

(c) Mach 4 inlet design body centerline cases.

(d) Mach 4 inlet design cowl centerline cases.

Figure 52. Centerline pressure as a function of inlet length for all contraction ratios.

(a) Mach 5 inlet design body centerline cases.

(b) Mach 5 inlet design cowl centerline cases.

(c) Mach 4 inlet design body centerline cases.

(d) Mach 4 inlet design cowl centerline cases.

Figure 53. Centerline surface heat transfer as a function of inlet length for all contraction ratios.

Figure 54 shows the surface shear stress at the centerline. When figures 54 and 48 are compared, the Mach 4 off-design case is showing the separation to be along the cowl side of the inlet, just ahead of the inlet exit. Otherwise, the Mach 5 cases suggest no separation along the centerline of the inlet, and the body centerline of the Mach 4 cases show the same. What is interesting to note, however, is that the Mach 4 cases show measurably lower surface shear stress values than the Mach 5 cases along the body centerline. A root cause for the lower surface shear stress in the Mach 4 cases could have been the lower dynamic pressure condition of the computation and the resulting boundary layer thickness increase is shown in figure 55.
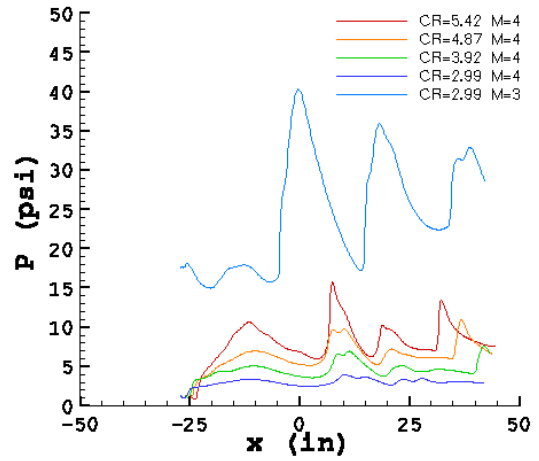

(a) Mach 5 inlet design body centerline cases.
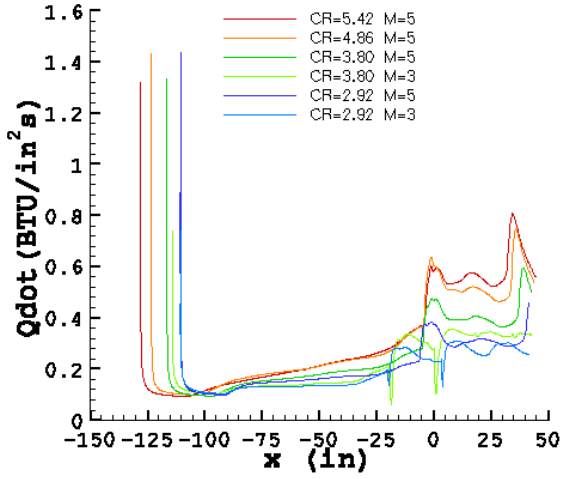
(b) Mach 5 inlet design cowl centerline cases.
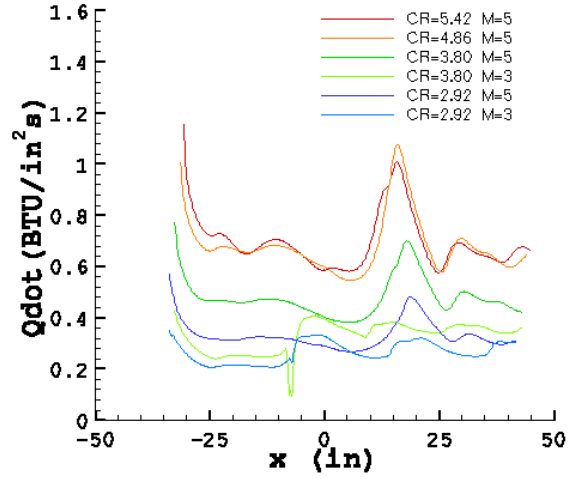
(c) Mach 4 inlet design body centerline cases.
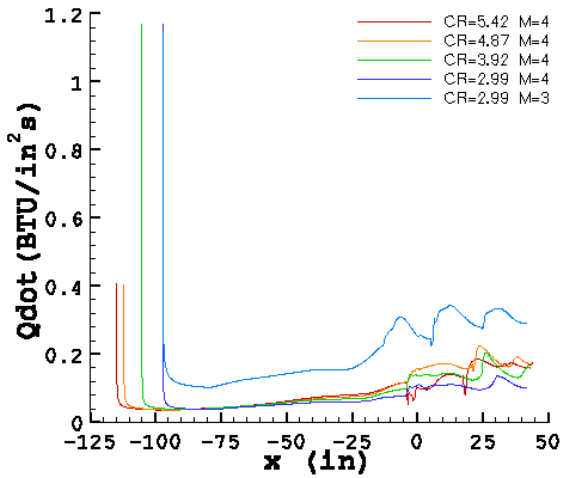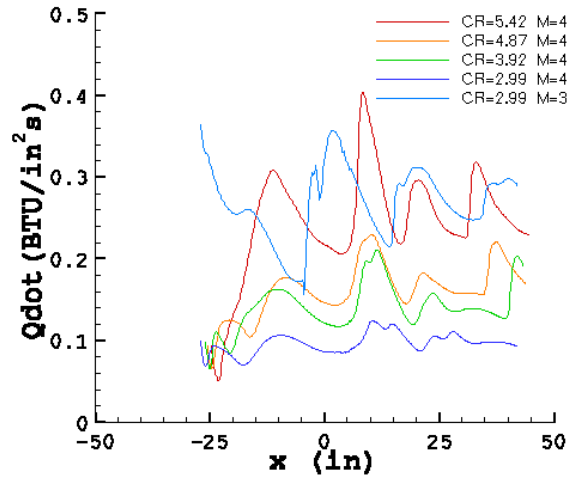
(d) Mach 4 inlet design cowl centerline cases.

Figure 54. Centerline surface shear stress as a function of inlet length for all contraction ratios.

The boundary layer thickness was determined where total enthalpy was 99.5 percent of the free-stream value. In these plots, the boundary layer thickness does not illustrate the sensitivity to the separation of the cowl side Mach 4 off-design case as significantly as the adverse pressure gradient does in figure 52(d). The fluid was showing signs of choking, indicated by sudden rise in pressure at the throat, yet a choked condition did not occur. A choking condition would have been evident by the increased boundary layer thickness (figure 55) on the cowl side by comparison to the trend in the Mach 5 cases. Thus, it indicated that the Mach 4 design for a low dynamic pressure condition could be adversely affected by flow conditions for a high dynamic pressure. This can be surmised because the Mach 5 high dynamic pressure condition computed showed a reverse trend in boundary layer thickness, as would be expected in a Mach 4 high dynamic pressure flow. This may also explain why the off-design case for the other Mach 4 inlets had difficulty remaining started.

Additionally, shown in figure 55d, the case 4A-D shows an odd buildup of boundary layer thickness. This is due to a lifting vortex in the core of the inlet flow field, originating from the cowl leading edge. The algorithm used to determine the boundary layer thickness does not account for this and is thus detecting an incorrect trend in the data. Only after the vortex is completely detached from the boundary layer within the analyzed cross-section is the correct boundary layer thickness detected near the end of the isolator section.

Further investigation into the boundary layer properties are shown in figure 56 and 57 for displacement thickness and momentum thickness, respectively. Both of these measures illustrate the same effects from the adverse pressure gradient and lifting core vortex, instead of a separation region on the cowl side of the inlet. Although the cowl information was not requested for all the boundary layer properties, the inclusion of this information provides valuable insight into the data collected for the computed inlets.

(a) Mach 5 inlet design body centerline cases.
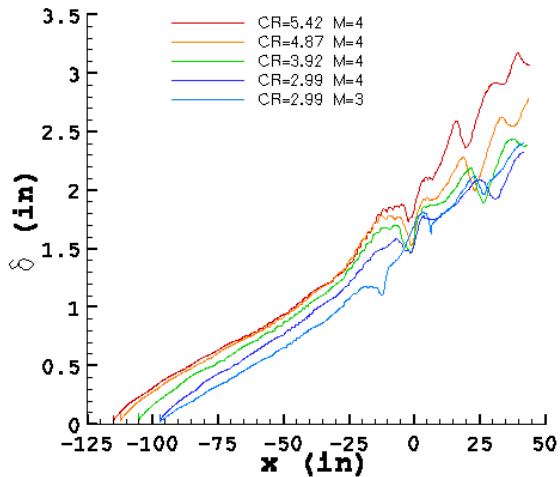
(b) Mach 5 inlet design cowl centerline cases.

(c) Mach 4 inlet design body centerline cases.
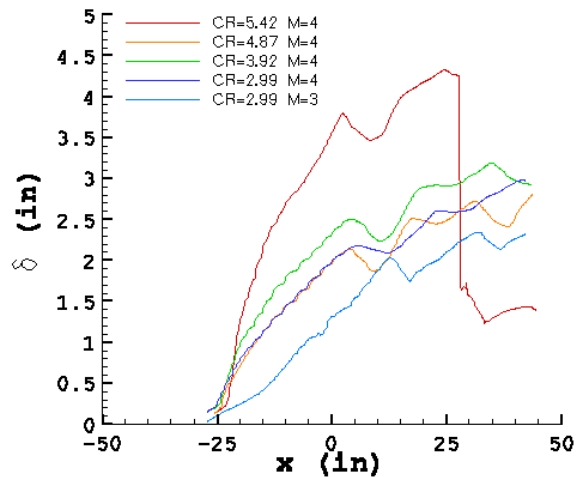
(d) Mach 4 inlet design cowl centerline cases.

Figure 55. Centerline boundary layer thickness as a function of inlet length for all contraction ratios.
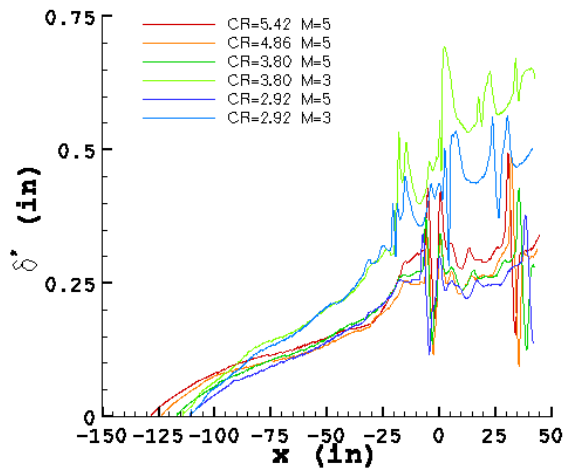
(a) Mach 5 inlet design body centerline cases.
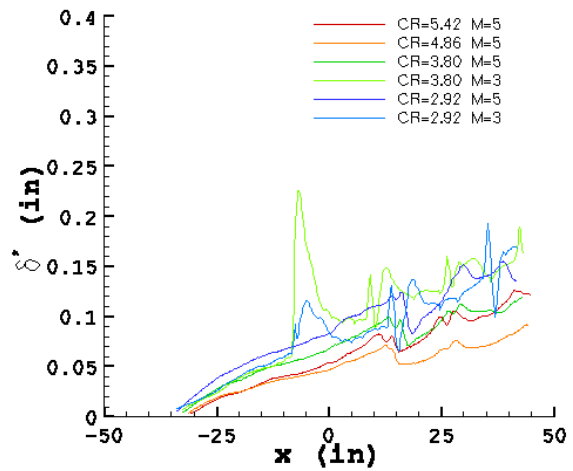
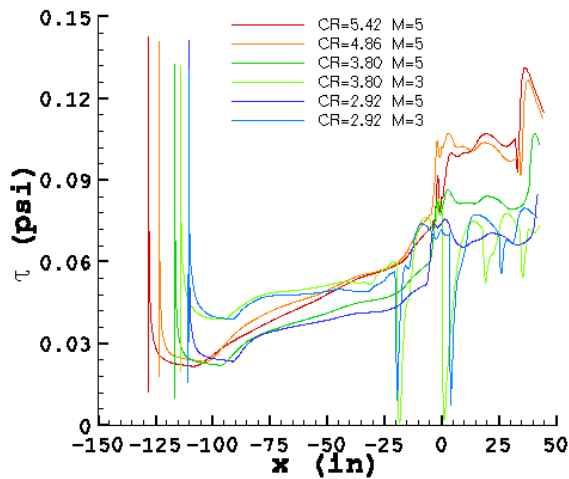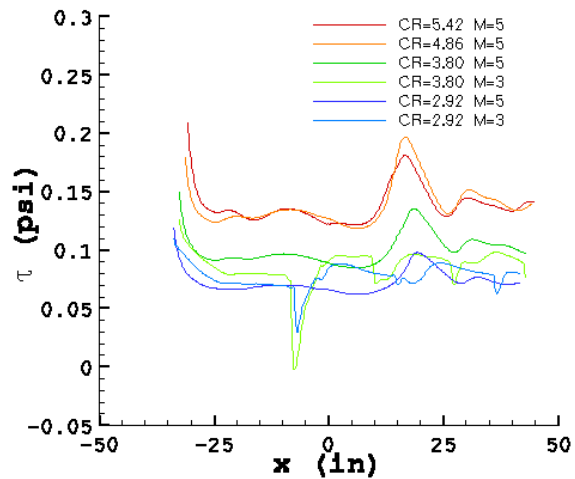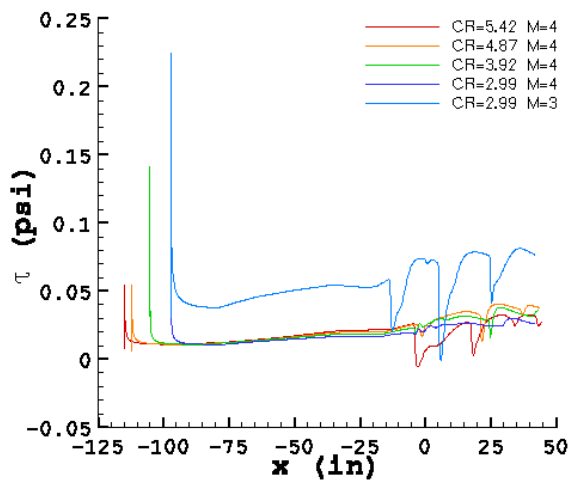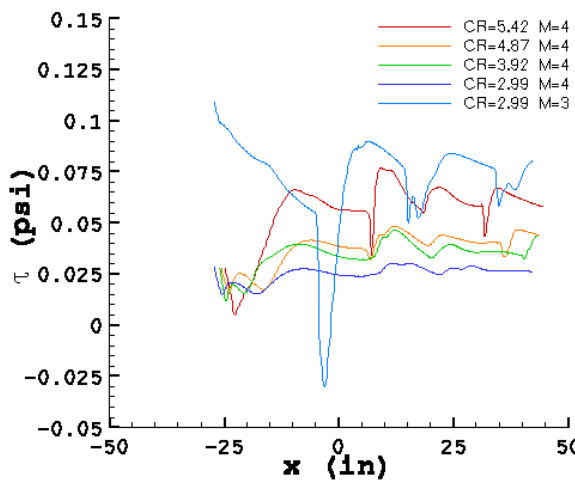(b) Mach 5 inlet design cowl centerline cases.
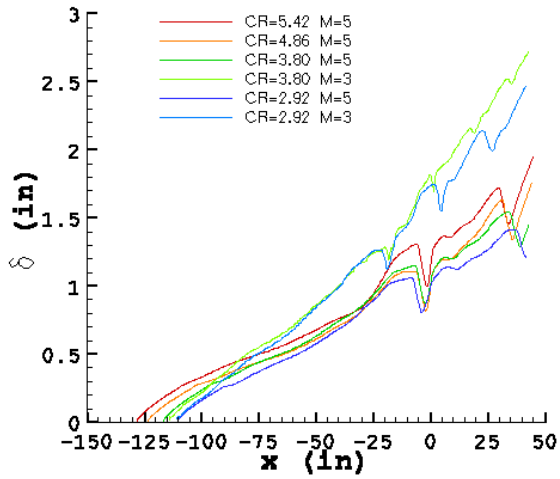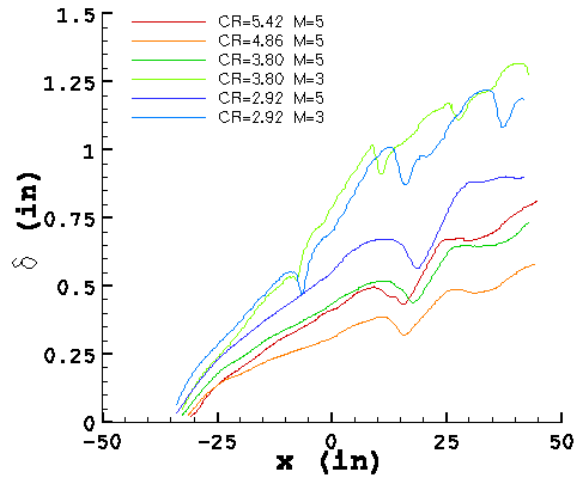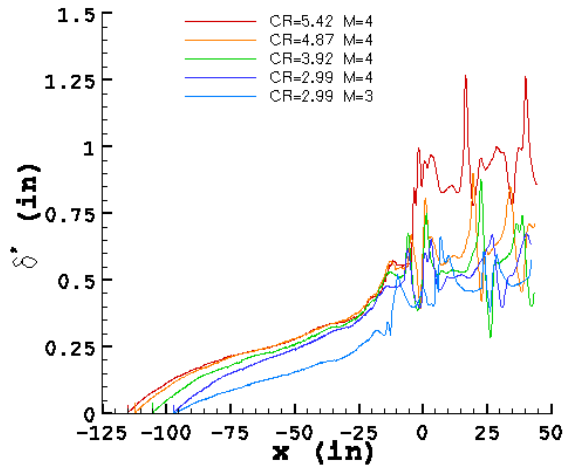
(c) Mach 4 inlet design body centerline cases.
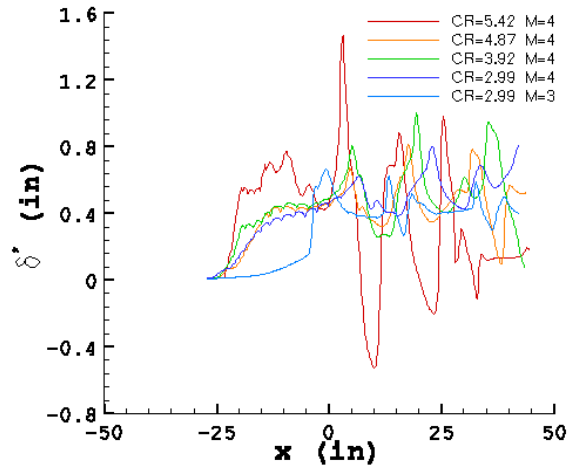
(d) Mach 4 inlet design cowl centerline cases.

Figure 56. Centerline boundary layer displacement thickness as a function of inlet length for all contraction ratios.
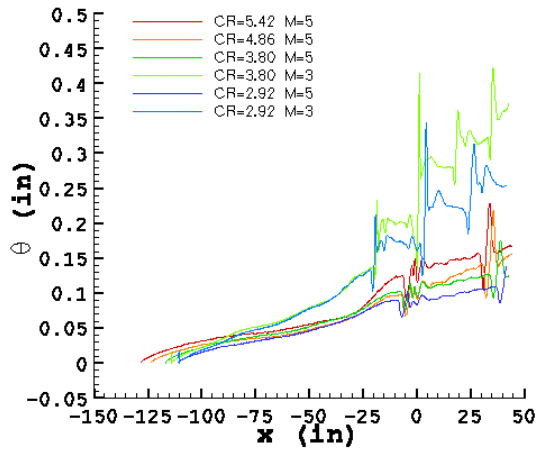
(a) Mach 5 inlet design body centerline cases.
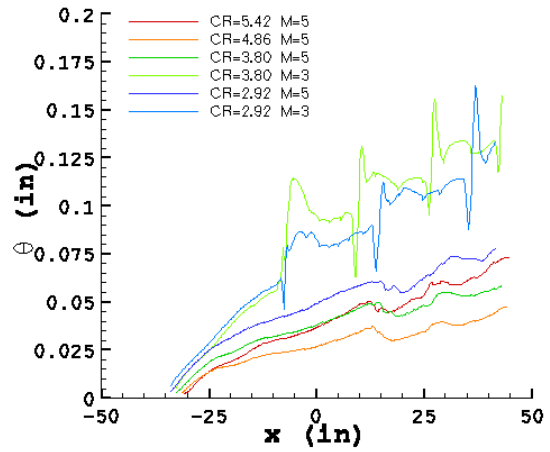
(b) Mach 5 inlet design cowl centerline cases.
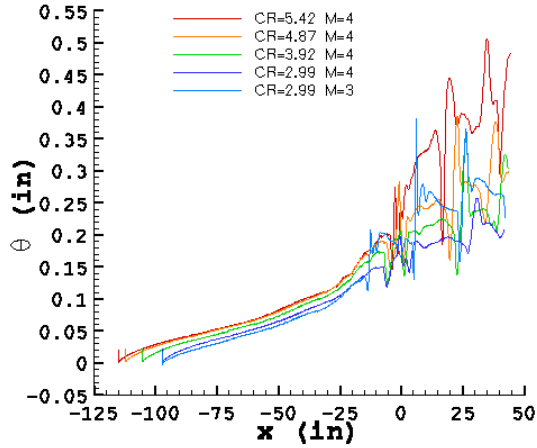
(c) Mach 4 inlet design body centerline cases.
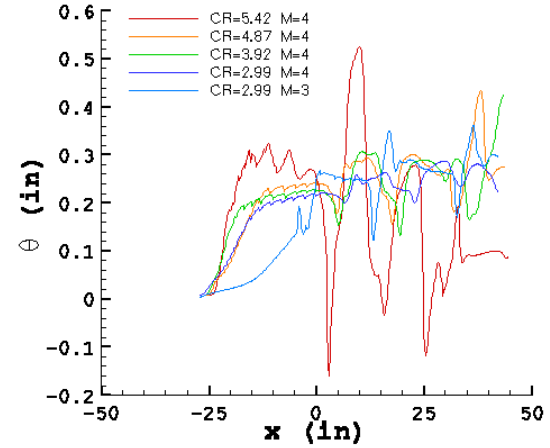
(d) Mach 4 inlet design cowl centerline cases.

Figure 57. Centerline boundary layer momentum thickness as a function of inlet length for all contraction ratios.

To get a clearer picture of the boundary layer edge, plots of the boundary layer edge for the Mach 5 and Mach 4 cases as shown in figures 58 and 59, respectively were examined. The edge of the boundary layer was determined at 99.5 percent of free-stream total enthalpy. With this criteria, an iso-surface at 99.5 percent illustrates the boundary layer edge. In the plots, this surface is shaded by temperature to provide additional information about the flow field. In all the cases that ran as started inlets, the Mach 4 cases clearly showed the affects of the adverse pressure gradients in the flow field based on the thickness of the boundary layers along the cowl side of the inlets. The body centerline side remained consistent with the Mach 5 cases.

Tables 11 and 12 list the tabulated data for the body centerline for the surface and edge properties, respectively.
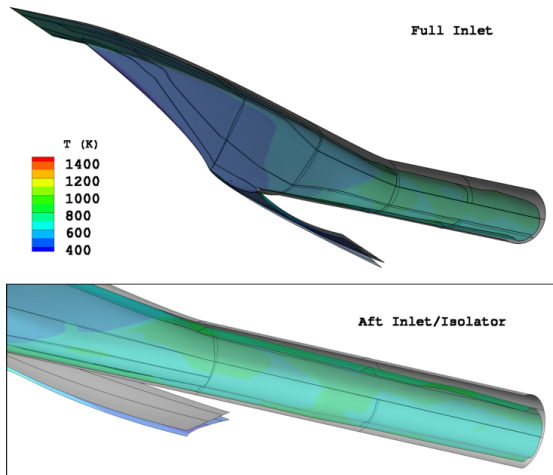
(a) Case 5A-D.
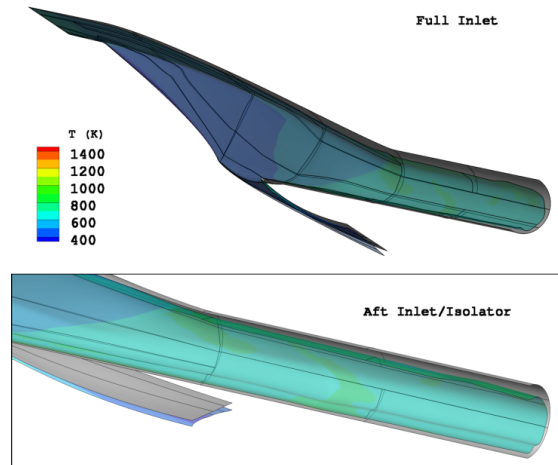
(b) Case 5B-D.
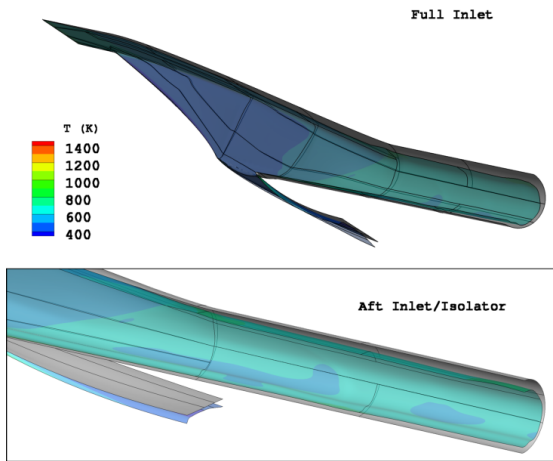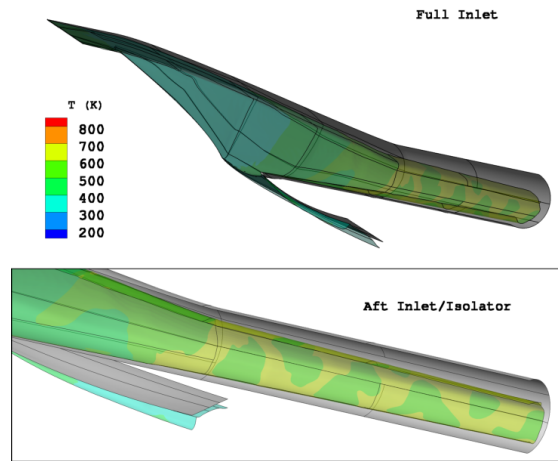
(c) Case 5C-D.

(d) Case 5C-OD.
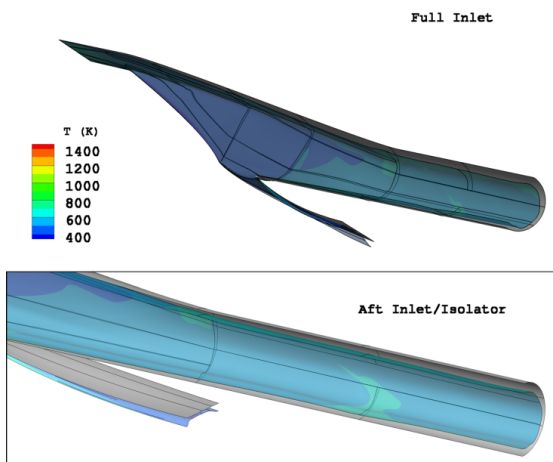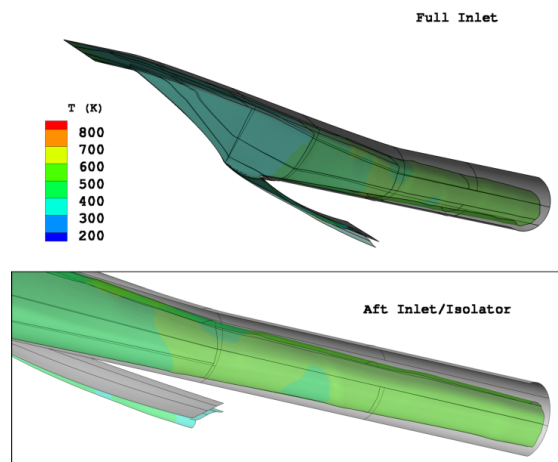
(e) Case 5D-D.

(f) Case 5D-OD.

Figure 58. Boundary layer edge inside the Mach 5 design case inlets.

(a) Case 4A-D.

(b) Case 4B-D.

(c) Case 4C-D.

(d) Case 4D-D.

(e) Case 4D-OD.
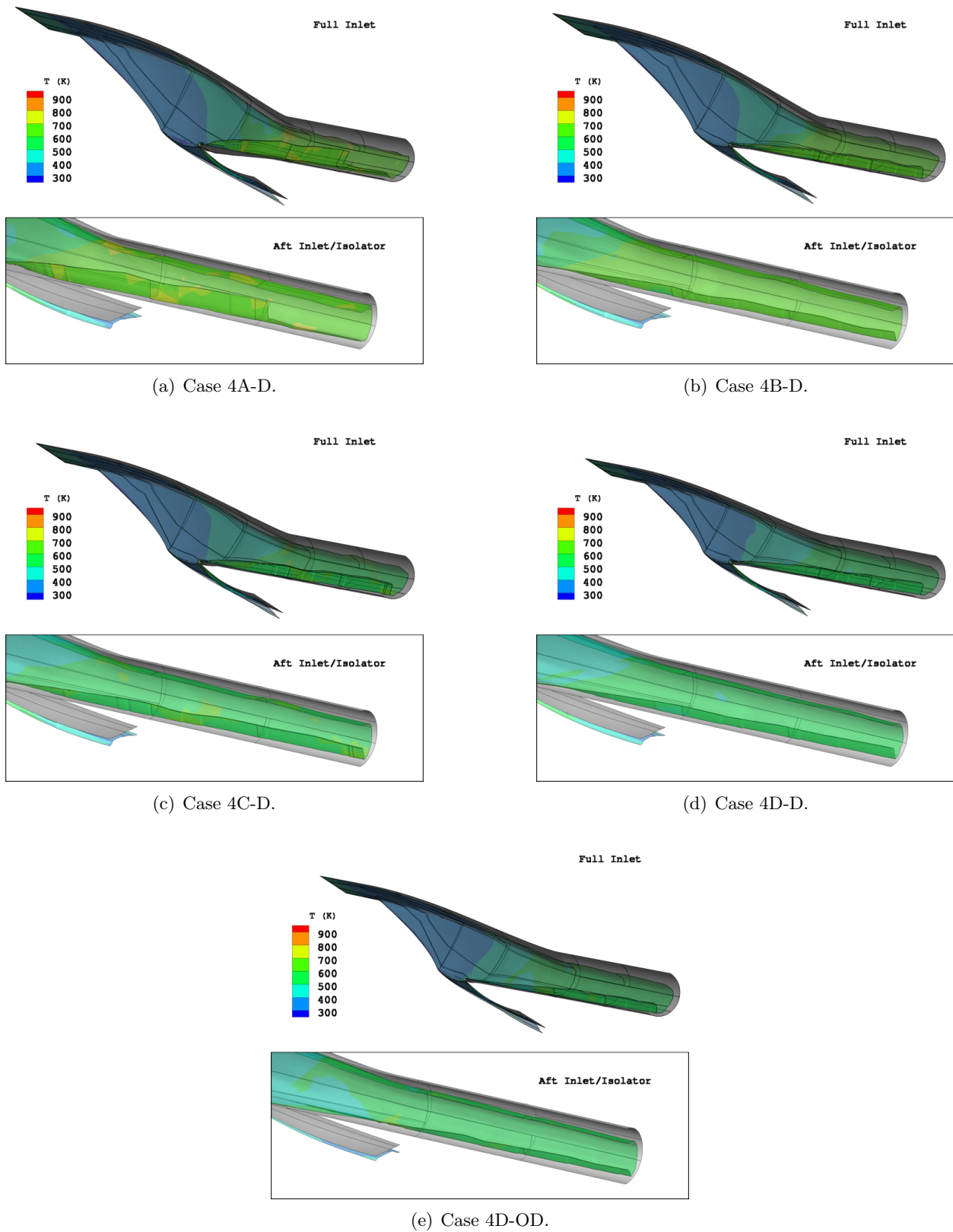
Figure 59. Boundary layer edge inside the Mach 4 design case inlets.

74

Table 11. Body centerline boundary layer based surface properties for the inlet exit.

Case ID	M_∞	Contraction Ratio	p (lb./in^2)	Heating (BTU/in^{2}s)	τ (lb./in^2)	δ Thickness (in)	δ^* Thickness (in)	θ Thickness (in)	Re_θ
5A-D	5.0	5.42	17.6922	0.5850	0.0840	1.1243	0.3488	0.1273	410.2428
5B-D	5.0	4.86	15.4909	0.6063	0.1017	0.9722	0.2871	0.0937	378.5071
5C-D	5.0	3.80	11.5413	0.4683	0.0791	1.0140	0.3089	0.0985	328.5602
5D-D	5.0	2.92	7.7568	0.3766	0.0740	0.9855	0.2913	0.0850	238.3000
5C-OD	3.0	3.80	38.4556	0.2737	0.0226	1.9199	0.7730	0.3002	2161.7998
5D-OD	3.0	2.92	14.1911	0.2287	0.0719	1.7361	0.4350	0.1635	739.4284
4A-D	4.0	5.42	8.7073	0.1034	0.0062	1.8479	0.8929	0.2349	408.5338
4B-D	4.0	4.87	6.6793	0.1577	0.0245	1.6177	0.6186	0.1989	369.2011
4C-D	4.0	3.92	4.9463	0.1373	0.0247	1.5777	0.5170	0.1969	277.0344
4D-D	4.0	2.99	3.5475	0.1088	0.0212	1.5412	0.4990	0.1786	251.0066
4D-OD	3.0	2.99	17.6404	0.2533	0.0726	1.7036	0.4700	0.1674	907.2484

Table 12. Body centerline boundary layer edge properties inlet exit.

Case ID	M_∞	Contraction Ratio	Edge Density (lbm/ft^3)	Edge Velocity (ft/s)	Edge Mach Number	Edge Viscosity (lbm/fts)
5A-D	5.0	5.42	2.1125e-05	4063.6074	2.1577	2.6630e-05
5B-D	5.0	4.86	1.9992e-05	4225.3871	2.3059	2.0917e-05
5C-D	5.0	3.80	1.5071e-05	4322.8914	2.4047	1.9532e-05
5D-D	5.0	2.92	1.1119e-05	4574.8733	2.6858	1.8137e-05
5C-OD	3.0	3.80	5.7398e-05	2254.7836	1.3822	1.7974e-05
5D-OD	3.0	2.92	2.8413e-05	2926.5706	2.0250	1.8385e-05
4A-D	4.0	5.42	1.1146e-05	3467.2697	2.0265	2.2220e-05
4B-D	4.0	4.87	1.0275e-05	3577.1894	2.1370	1.9798e-05
4C-D	4.0	3.92	7.6872e-06	3809.9402	2.3948	2.0820e-05
4D-D	4.0	2.99	5.9339e-06	3983.3763	2.6202	1.6819e-05
4D-OD	3.0	2.99	3.4291e-05	2793.6306	1.8761	1.7672e-05

The tabulated data for the body centerline boundary layer surface properties for pressure, surface heat transfer, and surface shear stress at the inlet exit are plotted in figure 60. Similar to the previous plots for pressure, as the contraction ratio increased, so too did the pressure. This is indicative of the direct proportionality of the contraction ratio to the compression ratio. With increasing compression, more work was performed on the fluid, so the surface heat transfer also rose as a function of the contraction ratio. The surface shear stress, however, was more driven by the adverse pressure gradient past the throat of the inlet, which showed some increase with the contraction ratio, but for the Mach 4 inlet design cases the surface shear stress was nearly insensitive to the contraction ratio.

(a) Pressure.

(b) Heat transfer.

(c) Surface shear stress.
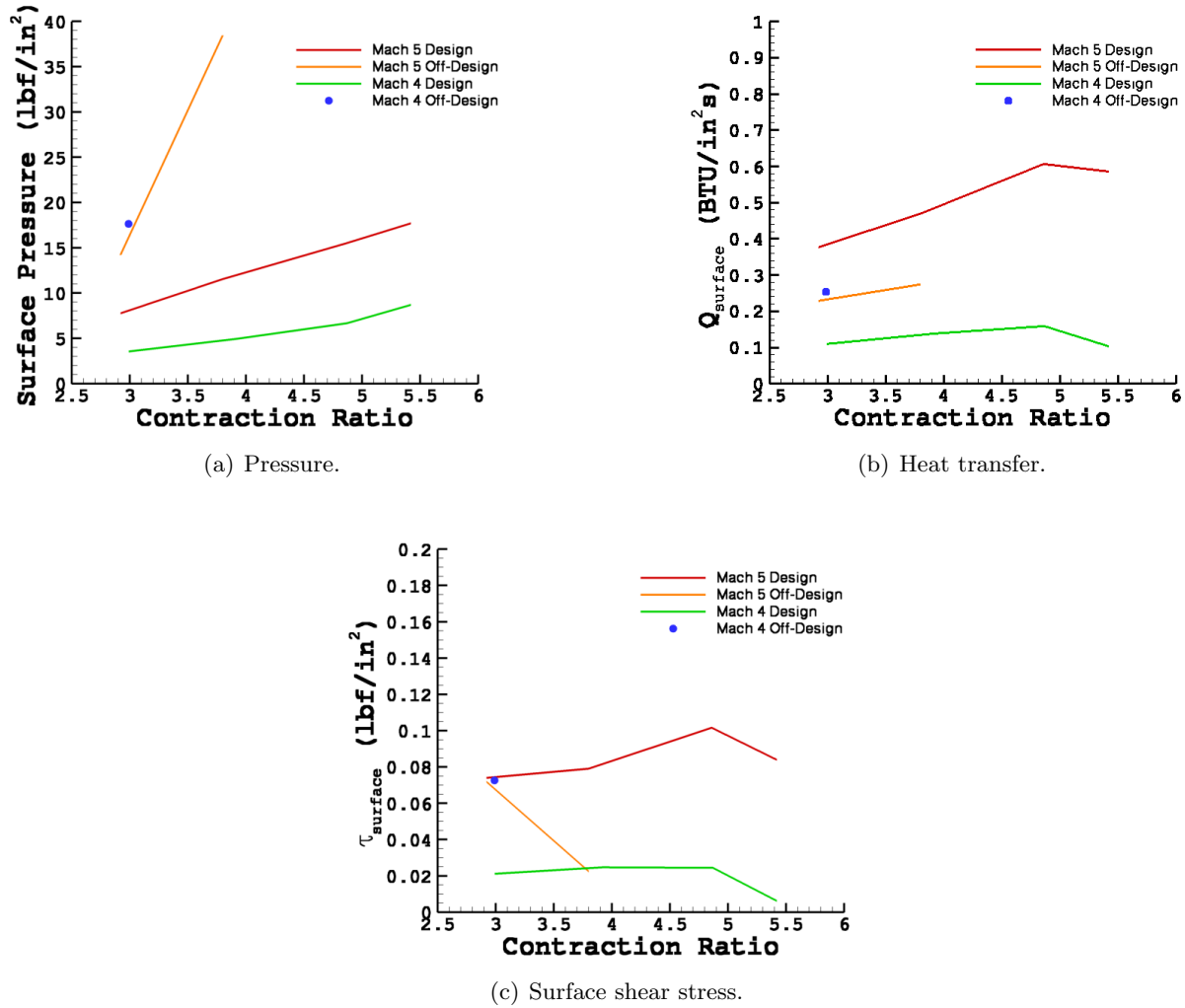
Figure 60. Body centerline surface properties as a function of the contraction ratio at the inlet exit.

The boundary layer edge properties of density, velocity, Mach number, and viscosity are shown in figure 61. The edge velocity and edge Mach number generally followed the same trend, indicating the compression of the flow field as the contraction ratio increased, where the density and viscosity was generally increasing with an increasing contraction ratio.

(a) Density.

(b) Velocity.

(c) Mach number.

(d) Viscosity.
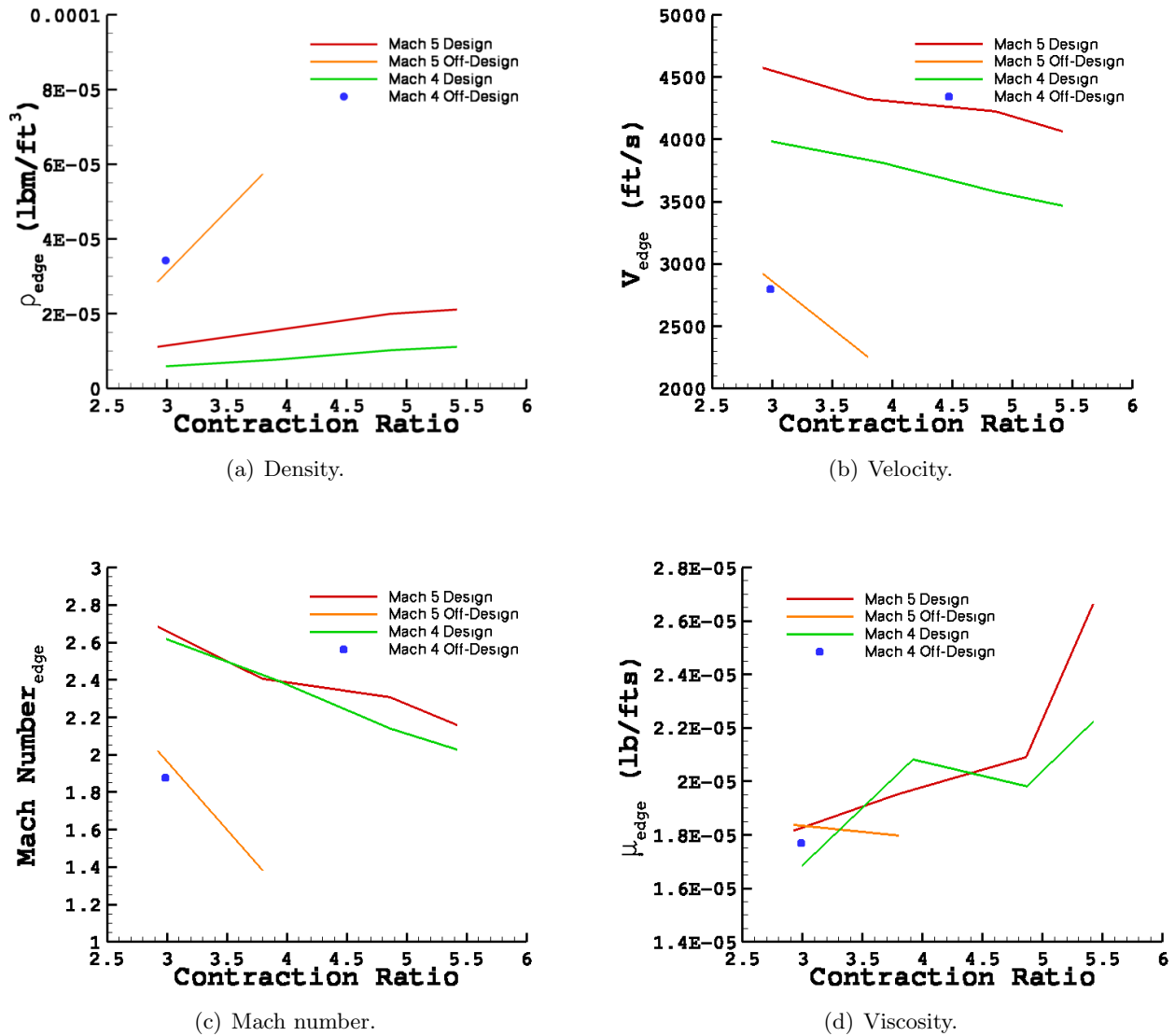
Figure 61. Body centerline boundary layer edge properties as a function of the contraction ratio at the inlet exit.

The boundary layer thickness, displacement thickness, momentum thickness, and Reynolds number based momentum thickness properties are shown in figure 62. Generally all these measures show a direct correlation with the contraction ratio. Of these data, what is most interesting is the insensitivity to Reynolds number based momentum thickness to the contraction ratio, and more importantly, the design Mach numbers. This particular measure is usually an indicator of when turbulent onset occurs with laminar boundary layers [30,31]. However, these inlets were computed with fully turbulent conditions so the measure was more of an indicator of energy in the boundary layer.

(a) Thickness.

(b) Displacement thickness.

(c) Momentum thickness.

(d) Reynolds number based momentum thickness.
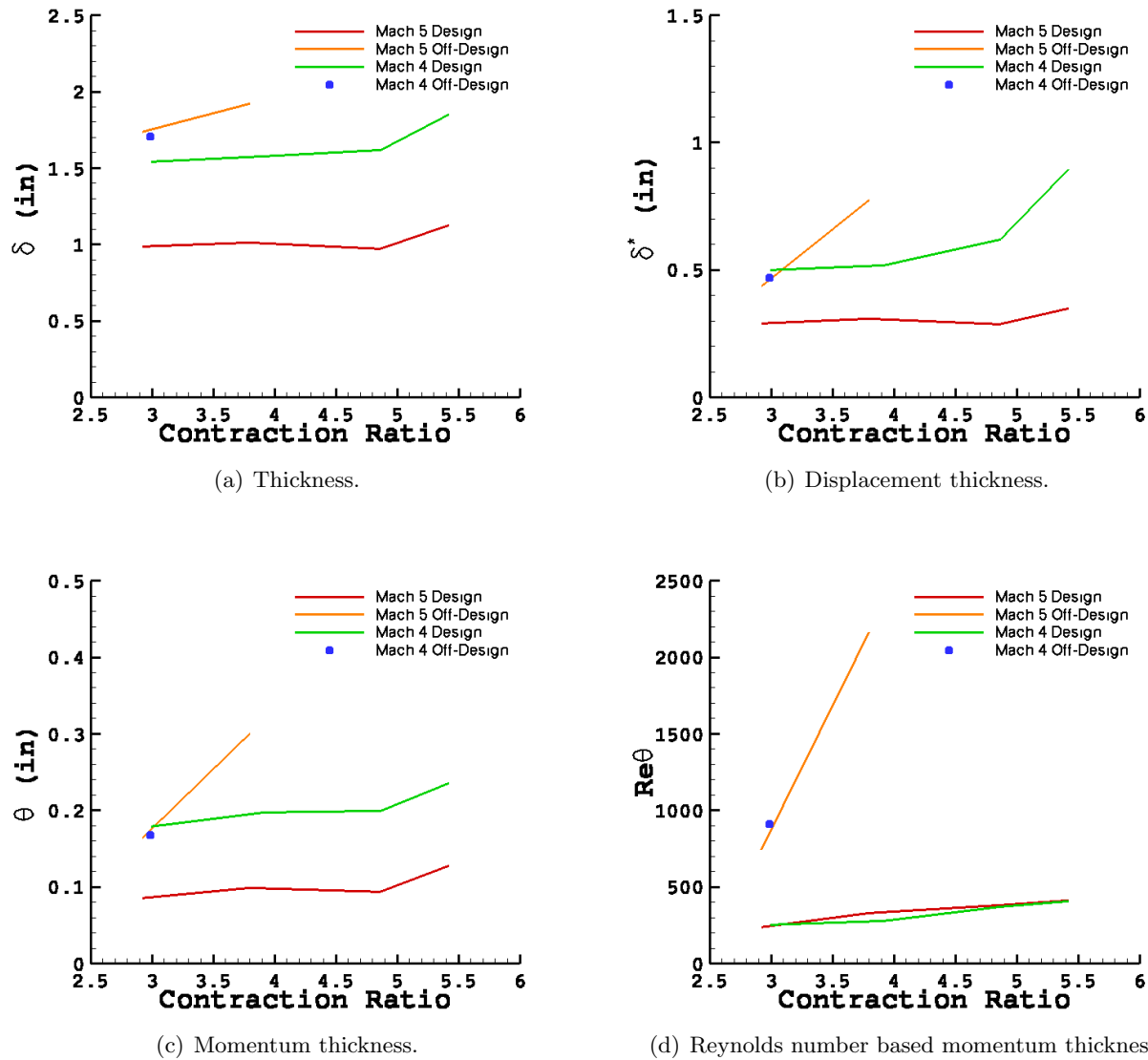
Figure 62. Body centerline boundary layer thickness properties as a function of the contraction ratio at the inlet exit.

While the tabulated and plotted data of these boundary layer dependent variables are useful, more information is easily gleaned from cross-sectional contour plots for the inlet and isolator exit. Due to the nature of the flow fields, these plots are provided for the Mach 5 and Mach 4 design in figures 63 and figure 64, respectively. Shown in figures 63 and 64 are the Mach contours on the left side and boundary layer area (based on total enthalpy) on the right side, with the boundary layer area ratios at the specific stations. As expected, as the fluid traveled from the inlet exit to the isolator exit, the boundary layer was increasing in area consumed by the flow. However, the rate was different from the Mach 5 to the Mach 4 design cases. This trend is more easily seen in the plots of the boundary layer area ratio shown in figure 65. Also interesting to note is the

more significant boundary layer roll-up for the Mach = 4 cases compared to the Mach = 5. At a contraction ratio of 5.42, a boundary layer bubble actually detached from the wall boundary layer. The roll-up was also larger for the 2.99 contraction ratio on design than the off-design cases.

(a) Case 5A-D.

(b) Case 5B-D.

(c) Case 5C-D.

(d) Case 5C-OD.

(e) Case 5D-D.

(f) Case 5D-OD.
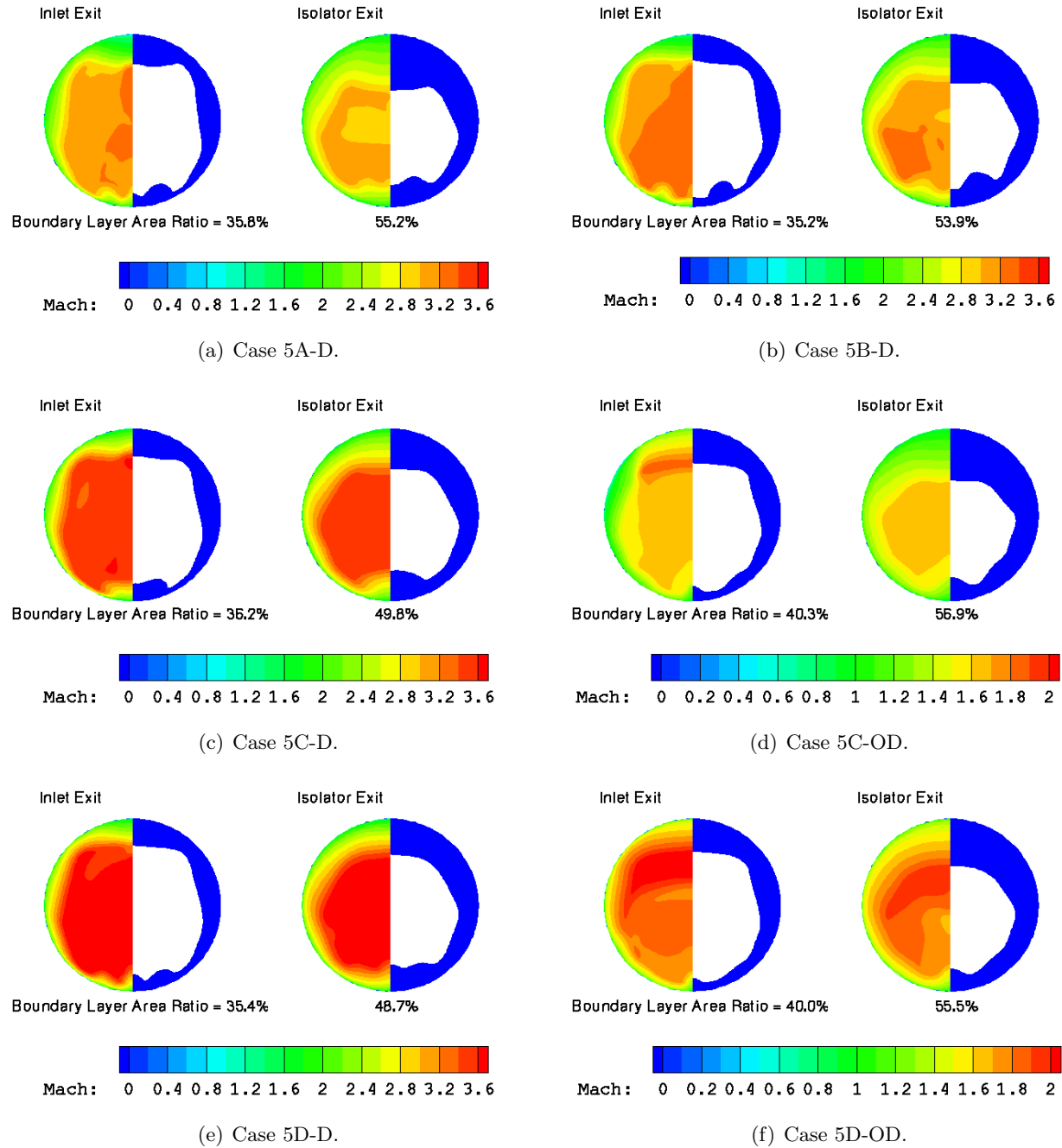
Figure 63. Boundary layer area ratio (A_δ/A_c) at the inlet and isolator exit for the Mach = 5 design cases.

(a) Case 4A-D.

(b) Case 4B-D.

(c) Case 4C-D.

(d) Case 4D-D.

(e) Case 4D-OD.
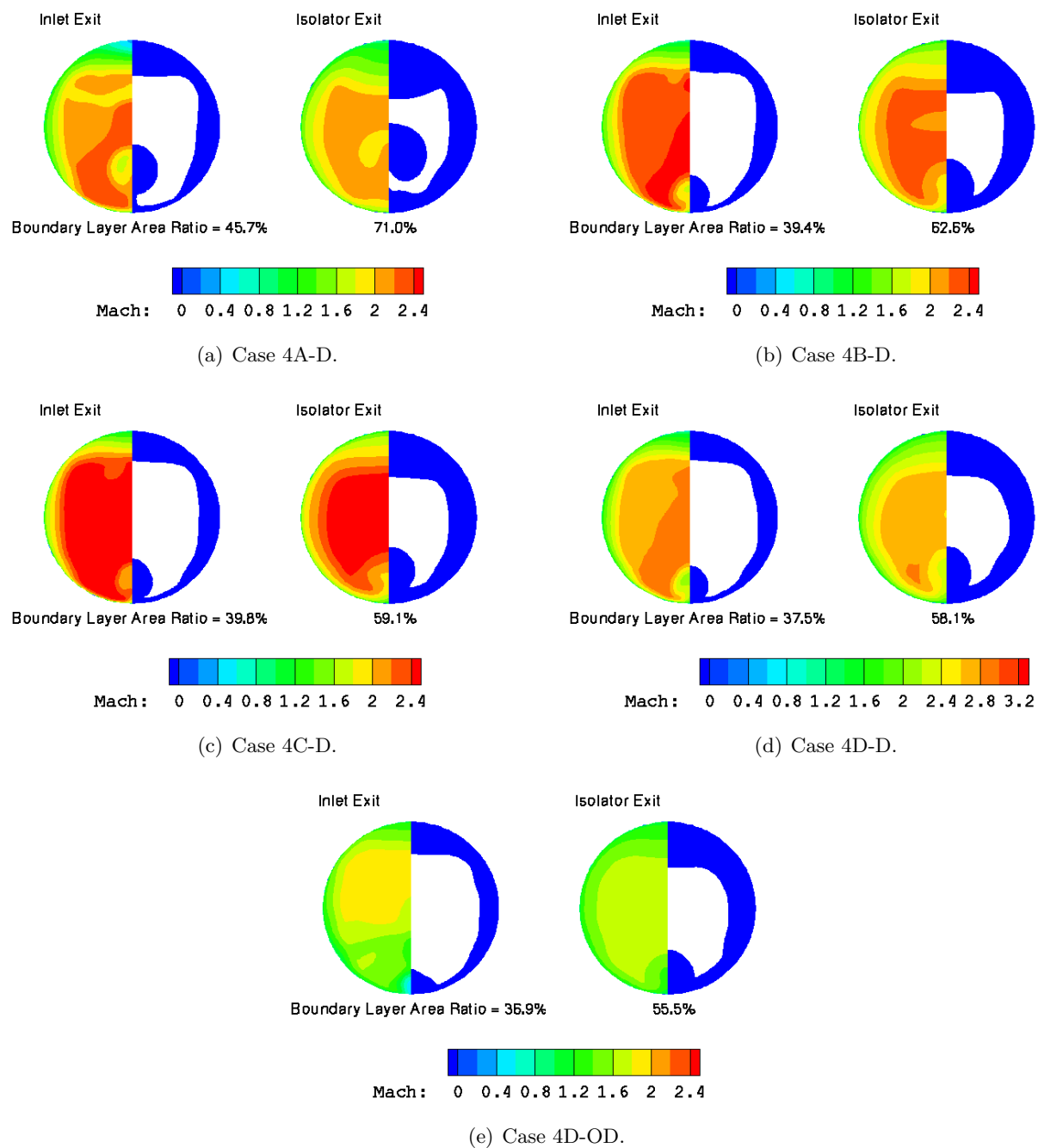
Figure 64. Boundary layer area ratio (A_δ/A_c) at the inlet and isolator exit for the Mach $= 4$ design cases.
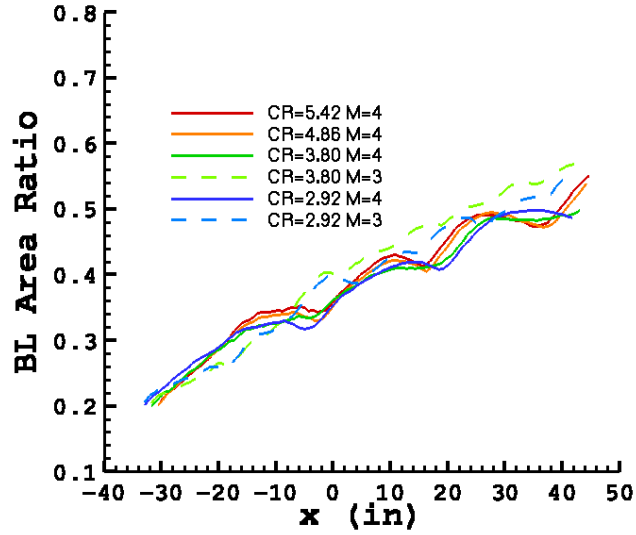
(a) Mach 5 designs.
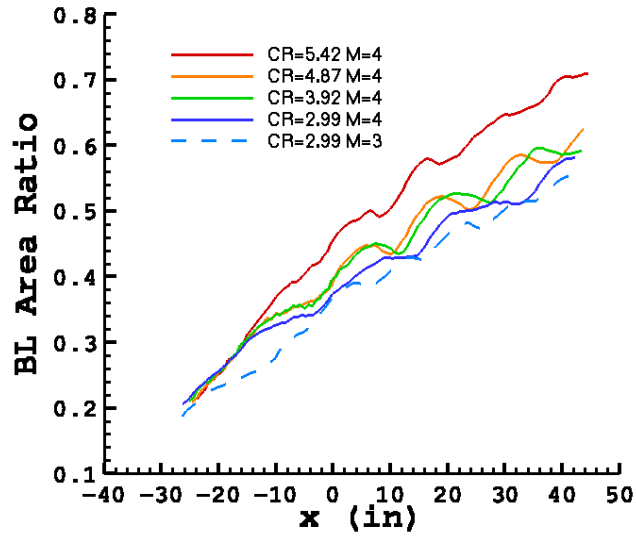
(b) Mach 4 designs.

Figure 65. Boundary layer area ratio (A_δ/A_c) as a function of inlet length for the various contraction ratios.

81

The boundary layer area ratios for the inlet and isolator exit, as well as statistical information about the mass capture and surface area of the inlets is tabulated in table 13. In plotted form, the inlet and isolator exit boundary layer area ratios are shown in figure 66.

Table 13. Boundary layer area ratios, mass capture, and surface area of the inlets.

Case ID	CR	Mach Number M_∞	$\dot{m}$ (lb/s)	Total Surface Area (in^2)	Inlet Exit BL Area Ratio	Isolator Exit BL Area Ratio
5A-D	5.42	5	67.66869	6155.992	35.8292	55.1545
5B-D	4.86	5	60.90490	5761.361	35.2423	53.9446
5C-D	3.80	5	47.53166	5171.740	36.1785	49.7728
5D-D	2.92	5	36.50679	4639.159	35.4492	48.6813
5C-OD	3.80	3	86.23160	5171.740	40.2519	56.9447
5D-OD	2.92	3	68.13606	4639.159	39.9763	55.4868
4A-D	5.42	4	25.87124	5891.562	45.6506	70.9674
4B-D	4.87	4	23.24510	5529.791	39.3538	62.6103
4C-D	3.92	4	18.70181	4913.820	39.8383	59.1221
4D-D	2.99	4	14.32167	4303.119	37.4639	58.1473
4D-OD	2.99	3	76.28876	4303.119	36.9043	55.4670

(a) Inlet exit.

(b) Isolator exit.
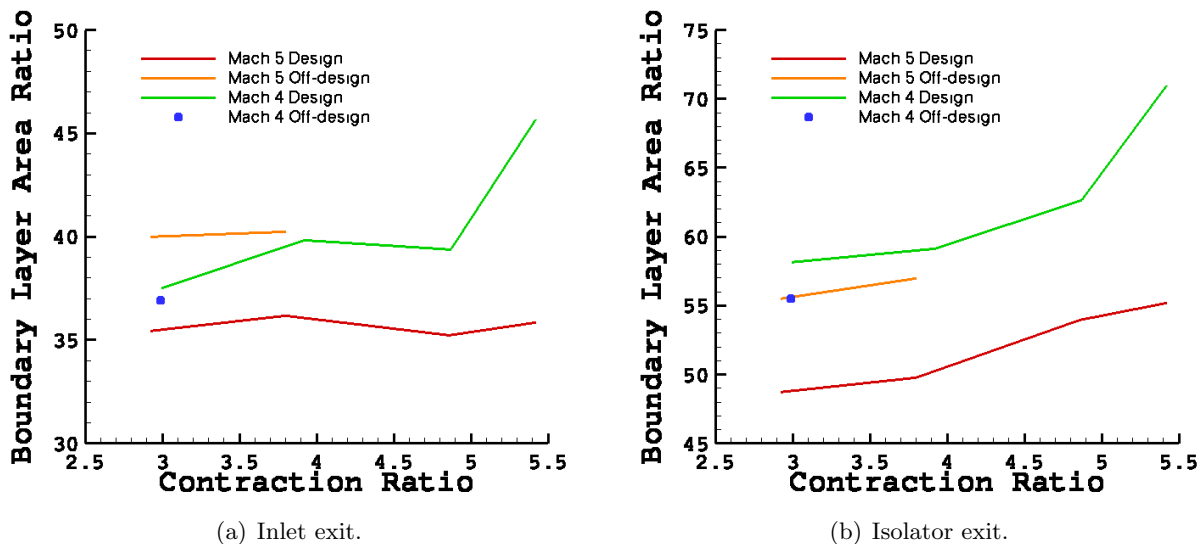
Figure 66. Boundary layer area ratio for two cross sections of each inlet.

The total surface area and mass capture for the inlets are shown in figure 67. The mass capture was directly proportional to the contraction ratio, which may seem counter intuitive because the compression of the fluid also rises. However, the throat size was fixed, free stream conditions were constant, so the larger contraction ratio implied a larger capture area. With a larger capture area, more mass capture occurred and, the more compression, the more mass could be swallowed by the inlet. The same was true for the surface area, which is useful to note because a higher surface area tended to increase total drag force.

(a) Mass capture.   (b) Total surface area.
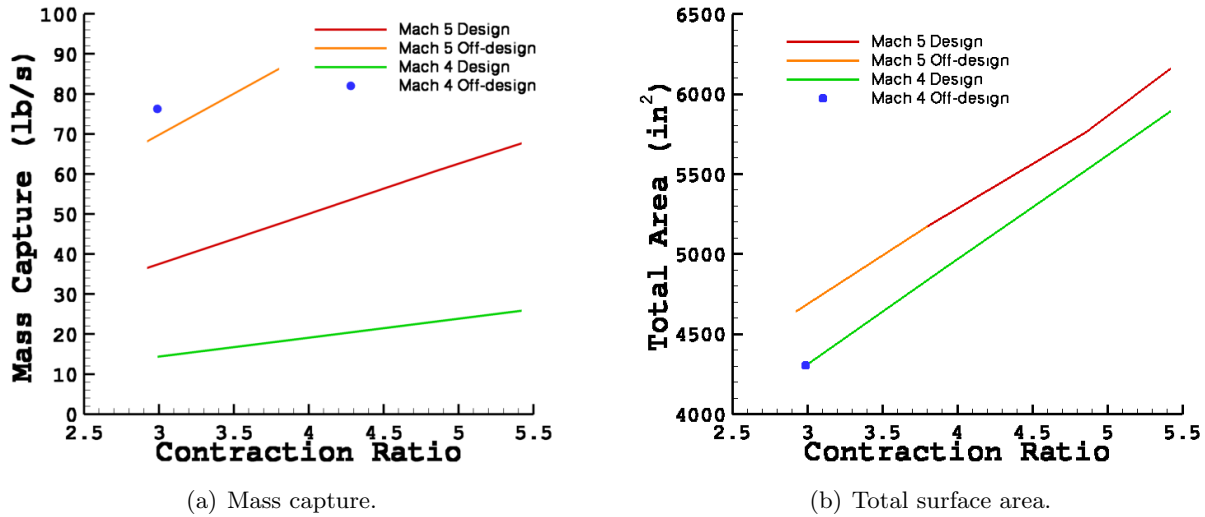
Figure 67. Total mass capture and surface area for the inlets.

A final set of data for consideration is the overall work of the inlets as characterized by the contraction ratio of the inlets. The inlets were designed with inviscid flow conditions, using target pressures at the inlet exit and, in the case of the lowest contraction ratio, the Kantrowitz self start limit as a target condition. The comparison of the overall contraction ratio of the design to the computed value based on flow conditions presented earlier is repeated here for completeness. The CFD computed contraction ratio was determined indirectly from the computations. The effective capture area was computed from the known quantities, including the isolator diameter exit of 9 inches, a doubling of the mass flow rate at the exit as computed by VULCAN, and the free-stream velocity and density. Beginning with continuity equation 4, the inlet flow capture stream must match the isolator exit.

$$\rho_0 U_0 A_0 = \rho_e U_e A_e = \dot{m}_e \tag{4}$$

The isolator exit mass flow rate is given by $\rho_e U_e$ times isolator exit area (nine inch diameter). Also known are the free-stream conditions for density $(\rho_0)$and velocity (U_0). Thus, the capture area for the inlet (A_0) is inferred and enables the determination of the the CFD computed, or over-all effective contraction ratio (A_0/A_e). In addition, tabulated with this comparison is the Kantrowitz contraction ratio based on internal Mach numbers at the notch for both design and CFD one-dimensional Mach numbers, listed in table 14.

These are subsequently plotted in figure 68. The differences between the internal design and computational internal contraction ratios as determined from the Kantrowitz limit equation are negligible. But by comparison to the internal design, it is quite different, except near the lowest contraction ratio, because that point was designed with the Kantrowitz limit as a target for the inlet. Since it was only a target, the differences are small, and the differences between the Mach 4 and Mach 5 cases are also small. The computed data is consistent with the design data, except for minor differences that can be attributed to viscous effects.

83

Table 14. Comparison of the computed and as designed contraction ratios for the inlets.

Case ID	M_∞	Design Contraction Ratio	Effective Contraction Ratio	Internal Design Contraction Ratio	Design Kantrowitz Contraction Ratio	CFD-1D Kantrowitz Contraction Ratio
5A-D	5.0	5.42	5.4433	2.03	1.4761	1.4660
5B-D	5.0	4.86	4.8993	1.94	1.4822	1.4700
5C-D	5.0	3.80	3.8235	1.74	1.4936	1.4845
5D-D	5.0	2.92	2.9366	1.54	1.5047	1.4895
4A-D	4.0	5.42	5.4334	2.15	1.3891	1.3861
4B-D	4.0	4.87	4.8819	2.06	1.3980	1.3894
4C-D	4.0	3.92	3.9277	1.82	1.4111	1.4012
4D-D	4.0	2.99	3.0078	1.59	1.4277	1.4153

(a) Mach 5.

(b) Mach 4.
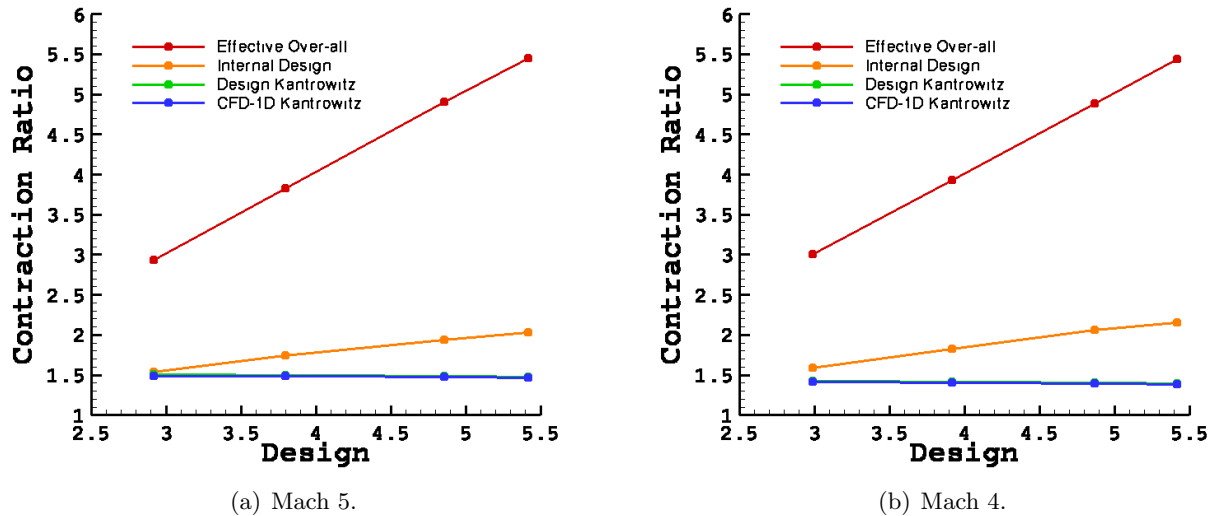
Figure 68. Effective and internal contraction ratios as a function of the design contraction ratios for the inlets.

7 Geometric Enhancements

The determination of geometric changes to the inlets evaluated in this study had several implications that make the effects of the changes uncertain. Changing one design feature could have both advantageous and disadvantageous effects on the overall design as well as the flow structure. Thus, a few geometric changes are offered as possibilities for the enhancement of flow and inlet performance characteristics.

7.1 A Modeling Change

When the inlets designed for this study were developed, several modifications of the original geometry were made to obtain the AML^{TM} input file. In one case, a change was made to soften a sharp corner at the cowl entrance. A suggested change is to not round this corner because it controls the angle of the turning shock. If the corner is rounded, the shock that results at this corner has a more shallow angle to the vertical, which will result in a stronger shock over all and a higher total pressure loss. By eliminating this curved surface, it is hoped that the total pressure loss may be reduced.

7.2 Boundary Layer Control

As reported in section 6.3, the boundary layer edge surface shown in figures 58 and 59 shows a relatively benign character. As the flow progresses axially down the interior of the inlet, the boundary layer thickens as would be expected. However, in the cross-sectional views of the boundary layer shown in figures 63 and 64, the thickness of the boundary layer changes significantly in the isolator section of the inlet, and, in all cases, there is a bubble on the cowl side and a rather thick section on the body centerline side.

During a detailed investigation of case 5A-D, a search for vortex cores in the flow field isolated three specific sections of the flow field that experienced vortical flow phenomenon. As can be seen in figure 69, there exists a vortex core along the inside of the cowl leading edge and two just after the notch on the inside and outside of the inlet. The inside vortex core past the notch is a continuation of the one along the inside cowl leading edge.
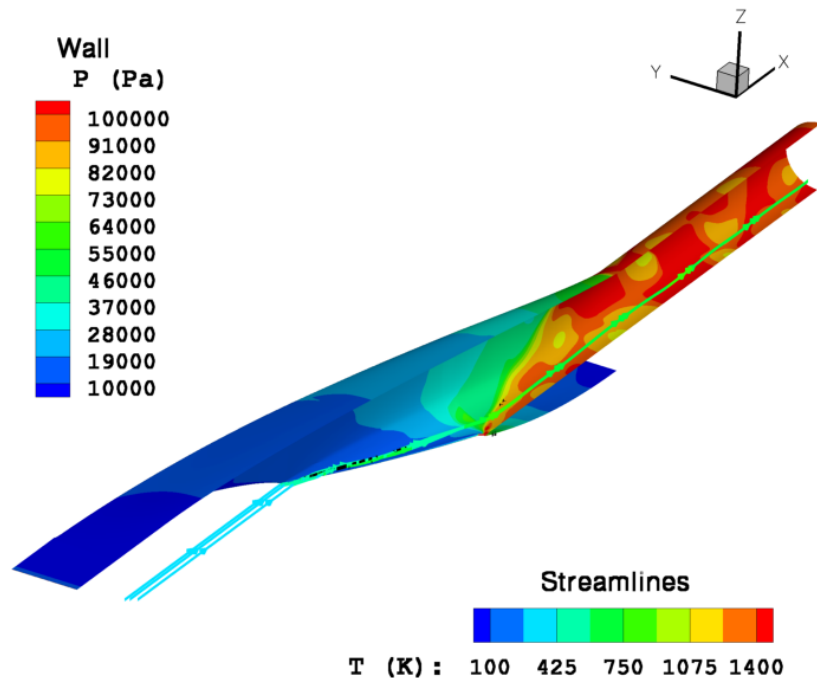

Figure 69. Volume streamlines about the vortex core; typical.

Although the inlet was at a relative angle of attack of zero, the external surface of the cowl was at a positive angle of attack. This produced a wing like structure with a pressure differential across the cowl leading edge, resulting in the formation of a vortex. The vortex then continues down the inlet axially until it exits the isolator. However, careful examination of this vortex core, illustrated in figure 70, shows that the vortex is inside the boundary layer and is responsible for the thickening of the boundary layer as it is traced axially down the inlet with the flow field.
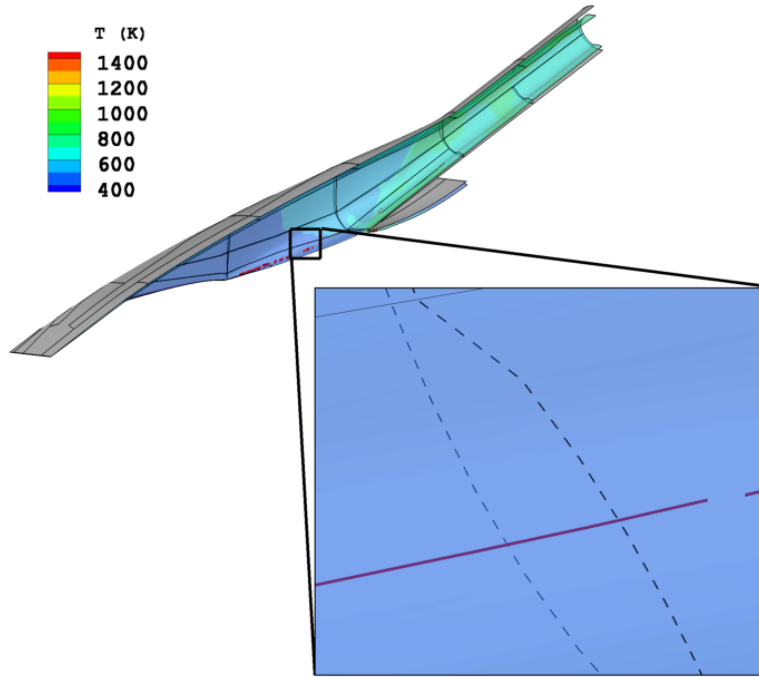

Figure 70. Vortex core immersion in the boundary layer along the inside of cowl leading edge.

This vortex core was found in all of the on-design Mach number inlets computed, as well as off-design cases, but was evaluated for the on-design Mach numbers only because trends were sought in the data. To determine the effect of the vortex core, at a specific grid point for the Mach 5 and Mach 4 cases, the orthogonal offset was determined. The grid point computational coordinates were held constant for the data extraction of this offset because the length of each of the inlet changed, and the grid point moved relative to the location of interest. Thus, by using the same computational grid point, the data was self similar in proportion to the length of the inlet. Figure 71 shows the height of the vortex core nearly 80 percent down the length of the cowl from the side wall.

As the compression of the inlets increased, the height of the vortex core also increased. This did not seem intuitive because the higher contraction ratio inlets were longer, which had the effect of reducing the effective angle of attack of the cowl leading edge. Thus, the compression and adverse pressure gradient were operating on the fluid in this region causing the vortex to lift. This was less than desirable because the effects for the Mach 4 high contraction ratio inlet caused the vortex to protrude into the operable inviscid section of the flow field as shown in figure 64a. Further evidence of the effects of this vortex can be seen in figures 72 and 73.
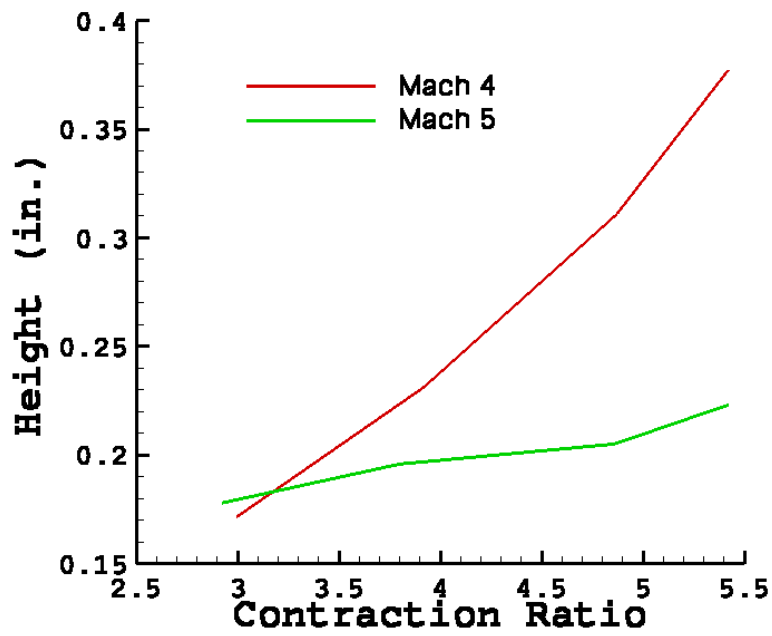
Figure 71. Vortex height at 80 percent downstream of the beginning of the cowl for all on-design inlet cases.

(a) CR = 5.42.

(b) CR = 4.86.

(c) CR = 3.80.
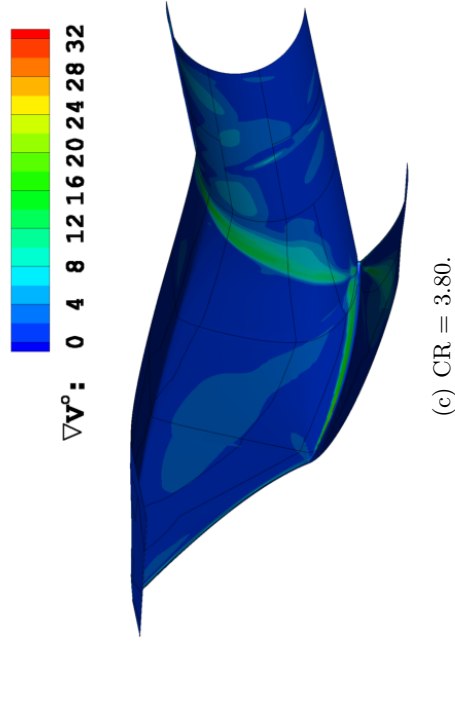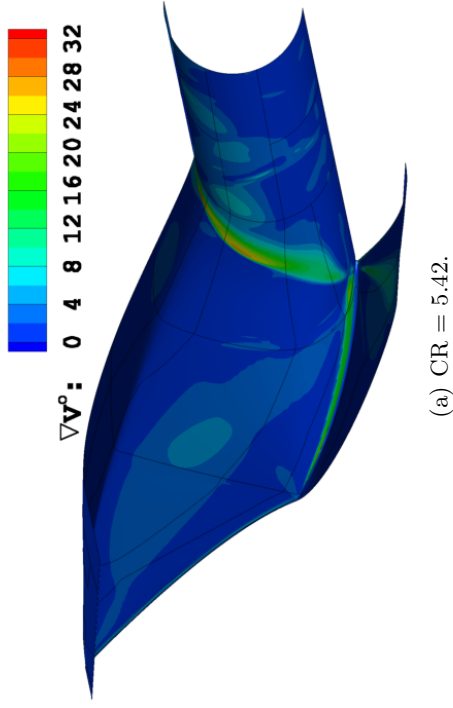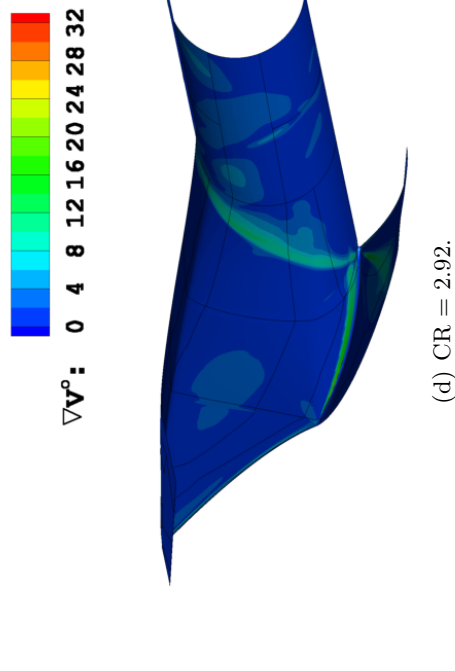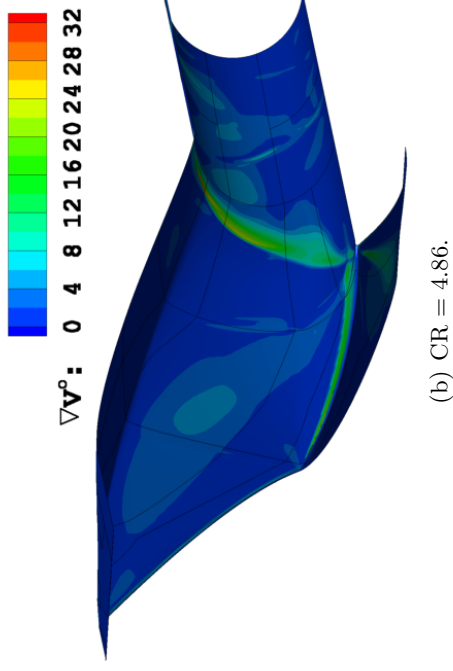
(d) CR = 2.92.

Figure 72. Angle difference between the surface shear stress and boundary layer edge velocities for the Mach = 5 on-design inlets.
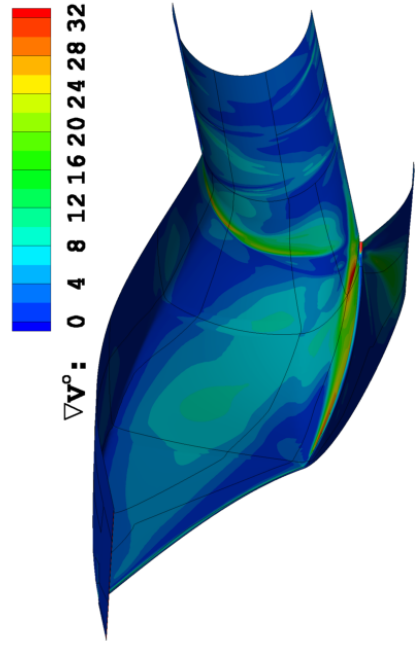
(a) CR = 5.42.
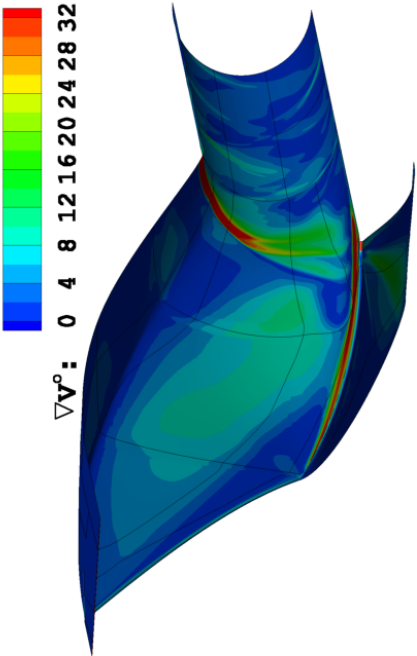
(b) CR = 4.87.
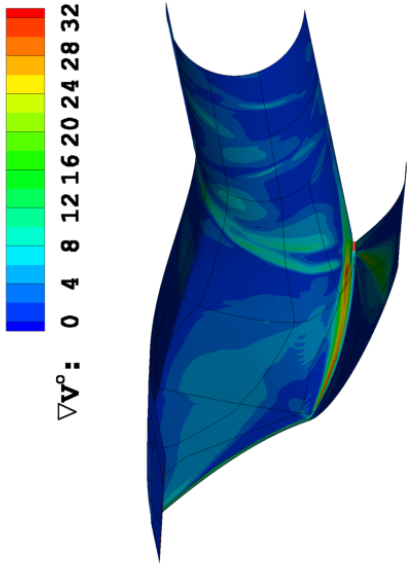
(c) CR = 3.92.
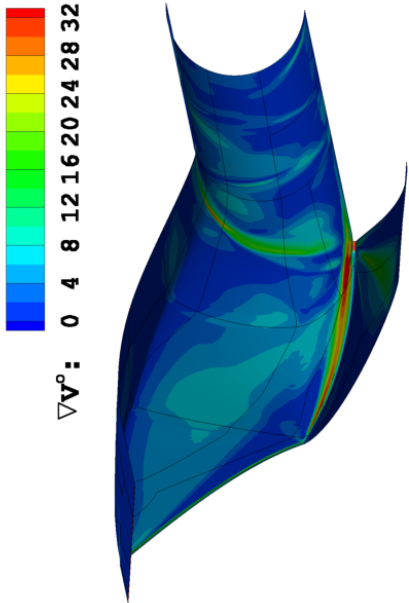
(d) CR = 2.99.

Figure 73. Angle difference between the surface shear stress and boundary layer edge velocities for the Mach = 4 on-design inlets.

In the region along the cowl leading edge, the differences in direction of the flow field were noticeably significant. The angles in this case are noted as the gradient of velocity, produced by evaluating the cosine of the angle between the two different vectors, but plotted on the wall of the inlets. This was due to the vortex inside the boundary layer changing the direction of the flow at the wall and opposing it at the boundary layer edge. While the angle was not significant, it clearly indicated significant cross-flow in this region.

There were a variety of methods available to deal with vorticies along a wing leading edge which in this case is synonymous with the cowl leading edge. The use of vortex generators is a common method to ensure a boundary layer is turbulent and that it will delay separation from the wall. However, in the case of these computations, the flow was considered fully turbulent. Thus another geometry change that could improve the quality of the flow and reduce the overall effectiveness of the cowl vortex was to blunt the cowl leading edge. Delta wings get the majority of their lift from the sharp leading edges which produce significantly strong vorticies. Thickening the cowl could offer an opportunity to reduce the strength of the vortex along the core and reduce the effect it had on the downstream boundary layer area. By making these changes, the tendency of the flow to separate based on the adverse pressure gradient and lifting of the vortex could improve total pressure recovery by increasing the size of the core flow region and reducing the boundary layer area ratio for the isolator.

Another less than desirable feature of the boundary layer for these flow fields was the thickness of the boundary layer on the body centerline at the isolator exit as shown in figures 63 and 64. The thicker the boundary layer, the more likely it is to separate. Considering this flow was going to be injected into the combustor of the scramjet engine, diminishing the thickness could prevent an adverse pressure gradient from causing flow separation in the isolator where the boundary layer was thickest. One of the more modern approaches to controlling the flow in this section of the inlet would be to use micro vortex generators (MVGs). According to recent work [32, 33], MVGs have been used effectively in high-speed flows to control the location and movement of boundary layers. Since the sides of the inlet have thinner boundary layer buildup, another geometric modification would be to either deflect the upper surface of the inlet inward towards the center of the core flow, or to use MVGs along the body centerline of the inlet to direct the boundary layer from there to the sides, thereby thinning the boundary layer at the body centerline while thickening it on the sides. Redistribution of the boundary layer could improve inlet performance by enabling compression without suffering from adverse pressure gradients separating the boundary layer before it enters the combustor, thereby improving total pressure recovery for the inlet.

8   Summary

Contained within this document is a study of inlets designed at a scale of six times the original size of the Hyper-X (X-43A) engine capture area of the vehicle. The inlets are evaluated as candidate configurations that can provide adequately compressed fluid to a combustor. The conditions used to evaluate these inlets are based on existing 8-ft high temperature tunnel nozzles, at two different design Mach numbers. Assessment of these inlets was performed for an off-design Mach number of three to determine if any of them are capable of producing adequate flow for multiple tunnel conditions. Four different geometric contraction ratios were evaluated, ranging from the highest of 5.42, designed to provide one atmosphere of pressure at the isolator exit, to the lowest of 2.92 based on the Kantrowitz self start limit for inlets. On-design Mach number computations show that all the inlets will support a started condition. However, very few inlets evaluated at the off-design Mach number were capable of providing the same. In fact, the higher the contraction ratio, the more likely the inlet experienced an unstart condition for the off-design cases.

These inlets are generally good for producing adequate flow to combustors of scramjet engines. They do suffer from adverse pressure gradients that can lead to boundary layer separation, but methods to mitigate this are offered as areas of consideration for future studies. The primary issue that these inlets have is a vortex along the cowl leading edge ahead of the full entrainment of the flow for the inlet. This vortex causes significant cross-flow inside the inlet, but there may be opportunities to mitigate the strength of this vortex.

References

1. McClinton, C. R.: X-43–Scramjet Power Breaks the Hypersonic Barrier, Dryden Lectureship in Research 2006. AIAA 2006–1, 44th AIAA Aerospace Sciences Meeting and Exhibit, January 2006.

2. Hodge, J. S.; and Harvin, S. F.: Test Capabilities and Recent Experiences in the NASA Langley 8-foot High Temperature Tunnel. AIAA 2006–2646, 21st AIAA Advanced Measurement Technology and Ground Testing Conference, June 2006.

3. Holdren, J. P.: National Aeronautics Research and Development Plan. Executive office of the president of the united states, National Science and Technology Council, February 2010.

4. Reed, D. K.; Mayle, M. N.; and Nance, D. K.: An Assessment of Ares I-X Aeroacoustic Measurements With Comparisons to Pre-Flight Wind Tunnel Test Results. AIAA 2011–174, 49th AIAA Aerospace Sciences Meeting and Exhibit, January 2011.

5. Weilmuenster, K. J.; Gnoffo, P. A.; and Greene, F. A.: Navier-Stokes Simulations of Orbiter Aerodynamic Characteristics Including Pitch Trim and Bodyflap. *Journal of Spacecraft and Rockets*, Vol. 31, no. 3, 1994, pp. 355–366.

6. Bertin, J. J.; and Cummings, R. M.: Critical Hypersonic Aerothermodynamic Phenomena. *Annual Review of Fluid Mechanics*, Vol. 38, 2006, pp. 129–157.

7. Trexler, C. A.: Inlet Performance of the Integrated Langley Scramjet Module (Mach 2.3 to 7.6). AIAA/SAE 1975-1212, 11th AIAA/SAE Propulsion Conference, October 1975.

8. Korte, J. J.; Singh, D. J.; Kumar, A.; and Auslender, A. H.: Numerical Study of the Performance of Swept, Curved Compression Surfacce Scramjet Inlets. AIAA 1993–1837, 29th AIAA/SAE/ASME/ASEE Joint Propulsion Conference and Exhibit, June 1993.

9. Kumar, A.; and Trexler, C. A.: Analysis and Performance Prediction of Scramjet Inlets Utilizing a Three-Dimensional Navier-Stokes Code. *Langley Symposium on Aerodynamics*, S. H. Stack, ed., NASA, Hampton, Virginia, Vol. 1, April 1985, pp. 187–208.

10. Holland, S. D.; and Perkins, J. N.: Contraciton Ratio Effects ina Generic Three-Dimensional Sidewall Compression Scramjet Inlet: A Computation and Experimental Investigation. AIAA 1991-1708, 22nd AIAA Fluid Dynamics, Plasma Dynamics, and Lasers Conference, June 1991.

11. Holland, S. D.: Mach 10 Computational Study of a Three-Dimensional Scramjet Inlet Flow Field. Technical Memorandum TM–4602, NASA, March 1995.

12. Smart, M. K.: Design of Three-Dimensional Hypersonic Inlets with Rectangular to Elliptic Shape Transition. *Journal of Propulsion and Power*, Vol. 15, no. 3, 1999, pp. 408–416.

13. Ferlemann, P. G.; and Gollan, R. J.: Parametric Geometry, Structured Grid Generation, and Initial Design Study for REST-class Hypersonic Inlets. *JANNAF Airbreathing Propulsion Subcommittee Meeting*, La Jolla, California, 2009.

14. VULCAN. `http://vulcan-cfd.larc.nasa.gov`.

15. White, J. A.; and Morrison, J. H.: A Pseudo-temporal Multi-grid Relaxation Scheme for Solving the Parabolized Navier-Stokes Equations. AIAA Paper 99–3360, AIAA, 1999.

16. van Wie, D. M.: Scramjet Inlets. *Scramjet Propulsion*, E. T. Curran and S. N. B. Murthy, eds., AIAA, Reston, Virginia, Vol. 189, 2000, pp. 447–511.

17. Holland, S. D.: Wind-Tunnel Blockage and Actuation Systems Test of a Two-Dimensional Scramjet Inlet Unstart Model at Mach 6. Technical Memorandum TM–109152, NASA, November 1994.

18. AML (Adaptive Modelling Language) from Technosoft Inc., Cincinnati, OH. http://www.technosoft.com.

19. Smart, M. K.; and White, J. A.: Computational Investigation of the Performance and Back-Pressure Limits of a Hypersonic Inlet. AIAA 2002–0508, 40th AIAA Aerospace Sciences Meeting & Exhibit, January 2002.

20. Smart, M. K.; and Trexler, C. A.: Mach 4 Performance of a Fixed-Geometry Hypersonic Inlet with Rectangular-to-Elliptical Shape Transition. AIAA 2003–0012, 41st AIAA Aerospace Sciences Meeting & Exhibit, January 2003.

21. Gollan, R. J.; and Ferlemann, P. G.: Investigation of REST-class Hypersonic Inlet Designs. AIAA 2011–2254, 17th AIAA International Space Planes & Hypersonic Systems Conference, April 2011.

22. Smart, M. K.; and Ruf, E. G.: Free-jet Testing of a REST Scramjet at Off-Design Conditions. AIAA 2006–2955, 25th AIAA Aerodynamic Measurement Technology and Ground Testing Conference, June 2006.

23. Gollan, R. J.; and Smart, M. K.: Design of Modular, Shape-Transitioning Inlets for a Conical Hypersonic Vehicle. AIAA 2010–0940, 48th AIAA Aerospace Sciences Meeting, January 2010.

24. GridPro, Program Development Corporation, White Plains, NY. http://www.gridpro.com.

25. Ferlemann, P. A.: COMPOSITE: A Computer Program to Efficiently Model Thermodynamic and Transport Coefficients of Mixtures. NASA LaRC Contract NAS1–96013 00–114, HNAG, 2000.

26. Wilcox, D. C.: Wall Matching, A Rational Alternative to Wall Functions. AIAA 1981–0611, 27th AIAA Aerospace Sciences Meeting, January 1989.

27. Ferlemann, P. A.; and Gollan, R. J.: Solution Process and Details for an Initial Design Study for REST-Class Hypersonic Inlets. Technical Note 10–545, Hypersonic Vehicle Analysis Group, 2010.

28. Meyer, B.: User Manual and Methodology for One-Dimensionalization Code: Massflow3D Version 8.4. Technical Note 06–474, NASA LaRC Contract NAS1–00135B, 2006.

29. Baurle, R. A.; and Gaffney, R. L.: The Art of Extracting One-Dimensional Flow Properties from Multi-Dimensional Data Sets. Paper 2007–0639, 45th AIAA Aerospace Sciences Meeting and Exhibit, 2007.

30. Liechty, D. S.; Berry, S. A.; Hollis, B. R.; and Horvath, T. J.: Comparison of Methods for Determining Boundary Layer Edge Conditions for Transition Correlations. Paper 2003–3590, AIAA, 2003.

31. Berry, S. A.; Hamilton, H. H.; and Wurster, K. E.: Effect of Computational Method on Discrete Roughness Correlations for Shuttle Orbiter. *Journal of Spacecraft and Rockets*, Vol. 42, no. 1, 2006, pp. 1–12.

32. Kumar, V. V.; and Bogadi, S.: Effect of Micro-Vortex Generator in Hypersonic Inlet. 1, International Journal of Applied Research in Mechanical Engineering, 2011.

33. Lu, F. K.; Li, Q.; Shih, Y.; Pierce, A. J.; and Liu, C.: Review of Micro Vortex Generators in High-Speed Flow. Paper 2011–0031, AIAA, 2011.

REPORT DOCUMENTATION PAGE

Form Approved
OMB No. 0704-0188

1. REPORT DATE *(DD-MM-YYYY)*	2. REPORT TYPE	3. DATES COVERED *(From - To)*
01-09-2012	Technical Memorandum	

4. TITLE AND SUBTITLE

Investigation of "6X" Scramjet Inlet Configurations

5a. CONTRACT NUMBER

5b. GRANT NUMBER

5c. PROGRAM ELEMENT NUMBER

6. AUTHOR(S)

Alter, Stephen J.

5d. PROJECT NUMBER

5e. TASK NUMBER

5f. WORK UNIT NUMBER

432938.11.01.07.43.05.01

7. PERFORMING ORGANIZATION NAME(S) AND ADDRESS(ES)

NASA Langley Research Center
Hampton, VA 23681-2199

8. PERFORMING ORGANIZATION REPORT NUMBER

L-20092

9. SPONSORING/MONITORING AGENCY NAME(S) AND ADDRESS(ES)

National Aeronautics and Space Administration
Washington, DC 20546-0001

10. SPONSOR/MONITOR'S ACRONYM(S)

NASA

11. SPONSOR/MONITOR'S REPORT NUMBER(S)

NASA/TM-2012-217761

12. DISTRIBUTION/AVAILABILITY STATEMENT

Unclassified - Unlimited
Subject Category 07
Availability: NASA CASI (443) 757-5802

13. SUPPLEMENTARY NOTES

14. ABSTRACT

This work represents an initial attempt to determine what, if any, issues arise from scaling demonstration supersonic combustion scramjets to a flight scale making the engine a viable candidate for both military weapon and civilian access to space applications. The original vehicle sizes tested and flown to date, were designed to prove a concept. With the proven designs, use of the technology for applications as weapon systems or space flight are only possible at six to ten times the original scale. To determine effects of scaling, computations were performed with hypersonic inlets designed to operate a nominal Mach 4 and Mach 5 conditions that are possible within the eight foot high temperature tunnel at NASA Langley Research Center. The total pressure recovery for these inlets is about 70%, while maintaining self start conditions, and providing operable inflow to combustors. Based on this study, the primary scaling effect detected is the strength of a vortex created along the cowl edge causing adverse boundary layer growth in the inlet.

15. SUBJECT TERMS

CFD; Combustion; Hypersonics; Scramjet

16. SECURITY CLASSIFICATION OF:			17. LIMITATION OF ABSTRACT	18. NUMBER OF PAGES	19a. NAME OF RESPONSIBLE PERSON
a. REPORT	b. ABSTRACT	c. THIS PAGE			STI Help Desk (email: help@sti.nasa.gov)
U	U	U	UU	99	19b. TELEPHONE NUMBER *(Include area code)* (443) 757-5802

Standard Form 298 (Rev. 8-98)
Prescribed by ANSI Std. Z39.18